Fall 11-14-2018

Carrier Lifetime vs. Proton Radiation in Prototype III-V and II-VI Space-based Infrared Detectors

Geoffrey D. Jenkins
University of New Mexico

Geoffrey D. Jenkins

Candidate

Electrical and Computer Engineering (ECE)

Department

This dissertation is approved, and it is acceptable in quality and form for publication:

Approved by the Dissertation Committee:

Dr. Ganesh Balakrishnan, Chairperson

Dr. Mansoor Sheik-Bahae

Dr. Francesca Cavallo

Dr. Christian Morath

Carrier Lifetime vs. Proton Radiation in Prototype III-V and II-VI Space-based Infrared Detectors

by

Geoffrey D. Jenkins

B.S., Elect. Engineering, Oregon Inst. of Technology, 2006
M.S., Electro-Optics, University of Dayton, 2008

DISSERTATION

Submitted in Partial Fulfillment of the
Requirements for the Degree of

Doctor of Philosophy
Engineering

The University of New Mexico

Albuquerque, New Mexico

December, 2018

DEDICATION

To my wife, Katie, my daughter, Hailey, and my son, Logan, thank you for all the support, motivation, and love you have given me.

ACKNOWLEDGMENTS

First and foremost I would like to acknowledge and thank my parents, Richard and Teresa, for providing support and encouragement in my endeavors throughout my entire life, for which I am very grateful.

Secondly, I would like to thank Dr. Christian Morath. Your mentorship has been invaluable with this research and has shaped me into a better scientist. I thank you for all the helpful whiteboard discussions, enthusiastic guidance, and the habit of searching for physics-based answers to puzzling questions, even if some are “just electrical engineering.”

To my colleagues at the Air Force Research Laboratory and UNM, thank you all for the eagerness to help and teach me over the years.

To Dr. John Hubbs, in addition to the countless helpful discussions on radiation effects, thank you for allowing me to use your beam time to squeeze in some extra science.

Carrier Lifetime vs. Proton Radiation in Prototype III-V and II-VI Space-based Infrared Detectors

by

Geoffrey D. Jenkins

B.S., Elect. Engineering, Oregon Inst. of Technology, 2006
M.S., Electro-Optics, University of Dayton, 2008

Ph.D., Engineering, University of New Mexico, 2018

ABSTRACT

Researchers have spent over 50 years improving the performance of HgCdTe infrared (IR) detectors and it is currently the dominant technology in the field; however, further improvement may be limited due to devices reaching the intrinsic limits of their constituent materials. To further improve the state-of-the-art in space-based IR detection, alternative material systems are being considered. The focus of this work is testing the space-environment viability of innovative device structures, namely unipolar barriers with Type-II superlattice (T2SL) absorbers, made from the 6.1 Å family of III-V elements which are theoretically superior performers while being less costly.

Sensitive IR photo-detection using III-V material systems has been demonstrated; however, overall performance to-date has been hindered by short minority carrier lifetimes attributed to high concentrations of Shockley-Read-Hall (SRH) recombination centers. This problem is exacerbated when these materials are exposed to charged particle

irradiation, as is unavoidable for spacecraft electronics, due to displacement damage increasing the concentration of SRH defects.

In this work, a measurement system was designed and constructed to directly measure the minority carrier recombination lifetimes of prototype IR detector structures at the wafer die level as functions of proton fluence and temperature, to include both HgCdTe and the new 6.1 Å T2SL *nBn* technology being considered. It is unique for two reasons: 1) it was designed to be portable which allows *in-situ* lifetime characterization vs. stepwise proton irradiation by deploying it to radiation sources across the country, and 2) through cryogenic cooling, it maintains samples at mission operating temperatures throughout entire irradiation experiments which enables post-radiation annealing studies. The typical radiation test found in literature is a single, large dose performed at room temperature.

The conclusions in this dissertation are derived from analyses on data acquired from this measurement system at a monoenergetic proton source. Radiation tolerances of the minority carrier lifetime and post-radiation annealing effects are compared between HgCdTe photodiodes and 6.1 Å T2SL *nBn* detector structures, the effects of doping and other design parameters on the lifetime damage factors in III-V materials are investigated, and a damage factor vs. proton energy (NIEL) study was performed on III-V structures which allows spacecraft mission planners to extrapolate lifetime damage factors in these materials through any proton differential energy spectra of interest, *i.e.* satellite orbit.

TABLE OF CONTENTS

LIST OF FIGURES

LIST OF TABLES

Chapter 1

Introduction

1.1 The Infrared Spectrum and Applications

Electromagnetic radiation exists in a continuum of wavelength as shown in Figure 1.1, of which only a small fraction is visible to the human eye. Specific wavelength ranges within are divided and named, from shortest to longest wavelength: gamma ray, x-ray, ultraviolet (UV), visible, infrared (IR), microwave, and radio. This radiation may be described as streams of mass-less particles (photons), each traveling at the speed of light in a wave-like pattern. Each photon contains a certain amount of energy which is inversely proportional to its wavelength: $E_{photon} = hv = hc/\lambda$ (eV), where h is Planck's constant, v is the frequency, c is the speed of light, and λ is the wavelength.

Since its discovery in the early 1800's by Sir Frederick William Herschel, IR radiation has been increasingly utilized in an abundance of technological applications throughout a wide range of industries. To mention a few, spectroscopy is used to identify compounds in atmospheric, astronomical, and biomedical research, fiber optics are used for telecommunications and high power lasers, and IR detectors are employed in thermal imaging from military target acquisition to skin cancer screening [**1**]. The focus of work discussed herein is the characterization of emerging material technologies aimed at creating superior *space-based* IR optoelectronic devices, specifically photodetectors.

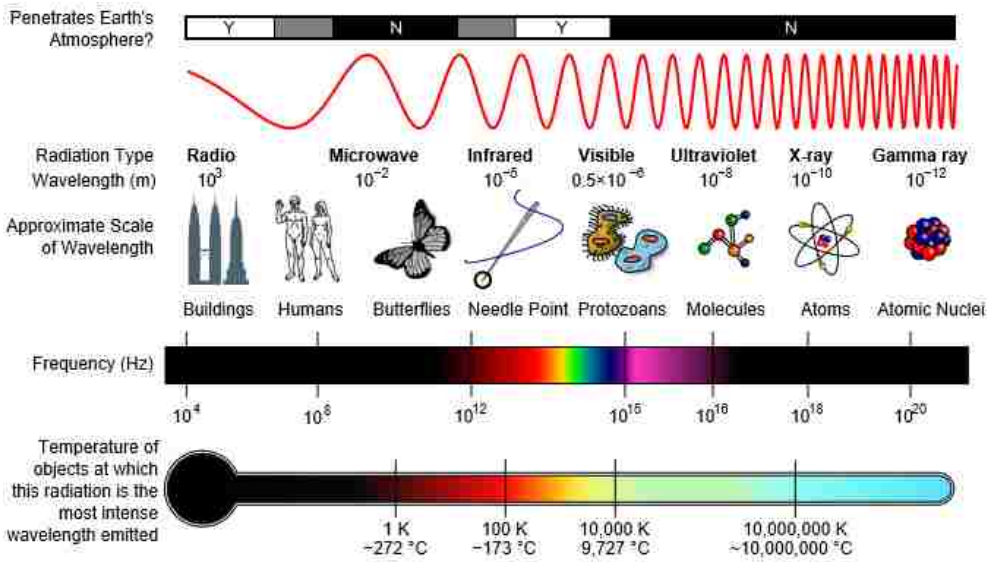

Figure 1.1: The electromagnetic spectrum. Credit: NASA.

Due to chemical and molecular absorption of IR radiation by the Earth's atmosphere, there is a limitation on how far photons of certain wavelengths can travel for practical use. Much international effort has been exerted in creating empirical databases for modeling atmospheric absorption as a function of wavelength, viewing angle, and location on Earth [**2**]. Figure 1.2 shows the atmospheric transmission of the IR spectrum.

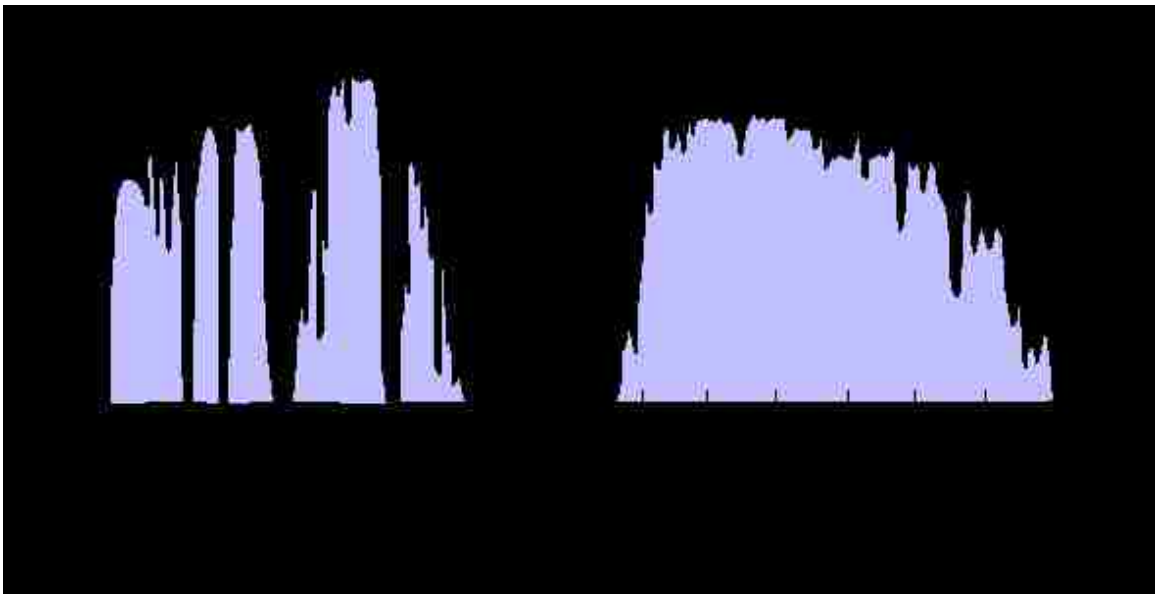

Figure 1.2: Atmospheric transmission of infrared radiation [**3**].

From this figure it should be noticed there exist sub-regions in the IR spectrum that exhibit very high transmission. These are known as atmospheric windows and their spectral ranges are roughly quantified in Table 1.1. The naming convention is as follows: near-infrared (NIR), short-wave-infrared (SWIR), mid-wave-infrared (MWIR), long-wave-infrared (LWIR), and far-infrared (FIR).

Table 1.1: Atmospheric windows in the IR

Atmospheric Window	λ (μm)	Application Examples
NIR	0.75-1	Pharmaceutical | Telecommunication | Agriculture | Spectroscopy
SWIR	1-2.5	Telecommuinication | Moisture Detection | Machine Vision| Spectroscopy | Mining
MWIR	3-5	Imaging through smoke and fog | Hot object thermal imaging
LWIR	8-12	Thermography | Body temperature thermal imaging | Night Vision
FIR	12-1000	Thermal Imaging | Biomedical

Photodetectors designed to sense in the MWIR and LWIR windows are the focus herein and are ideal for thermal imaging of hot (e.g. rockets and jet engines) and relatively cold (human body) objects, respectively, due to the wavelengths at which blackbody radiation for those temperatures peak. Heated objects, or bodies, each radiate photons in a continuum of wavelength but most are concentrated in the IR. Given the temperature of an object, its spectral radiance and exitance can be obtained using equations derived for blackbody emitters [**4**]:

$$L_{q,\lambda}(\lambda,T) = \frac{2c}{\lambda^4\left[e^{\mathrm{hc}/\lambda kT}-1\right]}\left[\frac{\text{photon}}{\text{s}-\text{cm}^2-\text{sr}-\mu\text{m}}\right] \tag{1.1}$$

$$M_{q,\lambda}(\lambda,T) = \frac{2\pi c}{\lambda^4\left[e^{\mathrm{hc}/\lambda kT}-1\right]}\left[\frac{\text{photon}}{\text{s}-\text{cm}^2-\mu\text{m}}\right] \tag{1.2}$$

When Eq. 1.2 is plotted vs wavelength, as is done in Figure 1.3, it can be seen that hotter objects radiate more photons at shorter wavelengths (higher energies). This is why light bulb manufacturers advertise a temperature in Kelvin on a scale from “warm” to “cool.” These equations are for ideal blackbodies and therefore should be treated as upper limits.

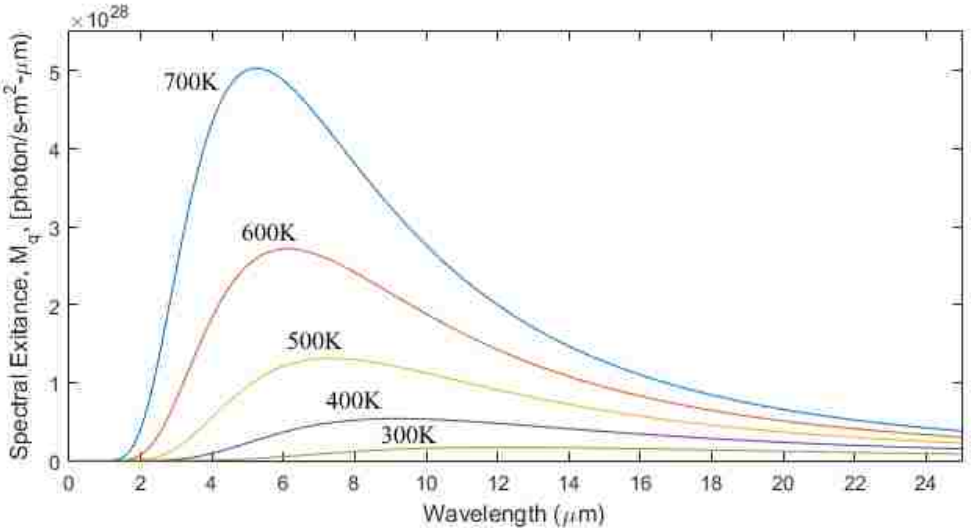

Figure 1.3: Spectral photon flux exitance for various blackbody temperatures.

In reality, most objects are not ideal blackbodies; therefore their radiance and exitance curves must be scaled down by a unitless emissivity factor $(0 \leq \varepsilon \leq 1)$ which is a function of reflectivity, surface texture, temperature, and wavelength.

The Wien Displacement Law quantifies the relationship between the wavelength of peak exitance and object temperature by setting the partial derivative of spectral photon flux exitance with respect to wavelength equal to zero and solving for wavelength at maximum exitance [**4**]:

$$\frac{\partial M_{q,\lambda}(\lambda,T)}{\partial \lambda} = 0 \tag{1.3}$$

$$\lambda_{max} = \frac{3662}{T}\left[\frac{\mu m}{K}\right] \tag{1.4}$$

Using this relationship one can easily find, for example, that the wavelengths of peak exitance of a jet engine (~1200 K) and human body (~310 K) are 3.05 μm (MWIR) and 11.8 μm (LWIR), respectively [**5**]. Separate photodetectors would have to be designed for each application, each optimized for detection around the maximum exitance of the intended targets while using a high transmission region of its IR atmospheric window.

1.2 Infrared Photo-detection

Semiconductors are naturally suited for photo-detection because their bandgap energies (energy required to free an electron from the valence band to the conduction band for free travel) coincide with photon energies inside and near the visible wavelength bands. This enables the creation of practical devices. According to the photoelectric effect, for an electron to be generated by a photon and have a chance at being detected, the photon's energy must be greater or equal to that of the semiconductor's energy bandgap. This is illustrated in Figure 1.4 for GaAs where $E_g = 1.424\ eV$ at room temperature, thus it is only able to detect photons with energies > 1.424 eV, corresponding to wavelengths < 870 nm (visible and NIR). If incident photon energies are too high, they are at risk of being absorbed by the surface of the detector and not making it to the active detection region, and if they are too low they will simply pass through the material with no effect. There are additional complications, such as reflectivity and absorption coefficients being functions of wavelength, and these must be considered in device design; however, the focus of this dissertation is on testing new material systems being created to produce specific energy bandgaps for reasons discussed later.

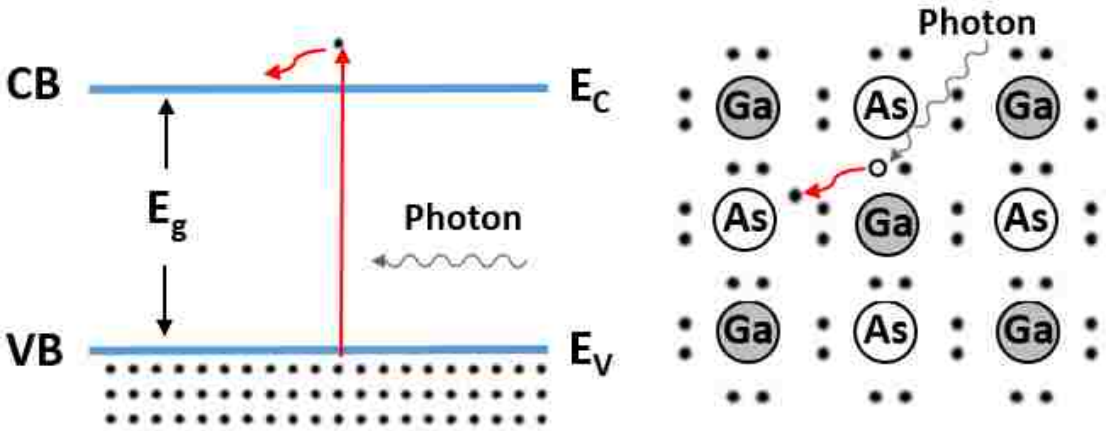

Figure 1.4: The photo-electric effect.

To design materials for photo-detection in the MWIR and LWIR, the energy bandgaps must be significantly smaller than those used for visible light. This is problematic due to the relative ease, as illustrated in Figure 1.5, of thermally generated charge carriers (noise) to outnumber those that are photo-generated (signal).

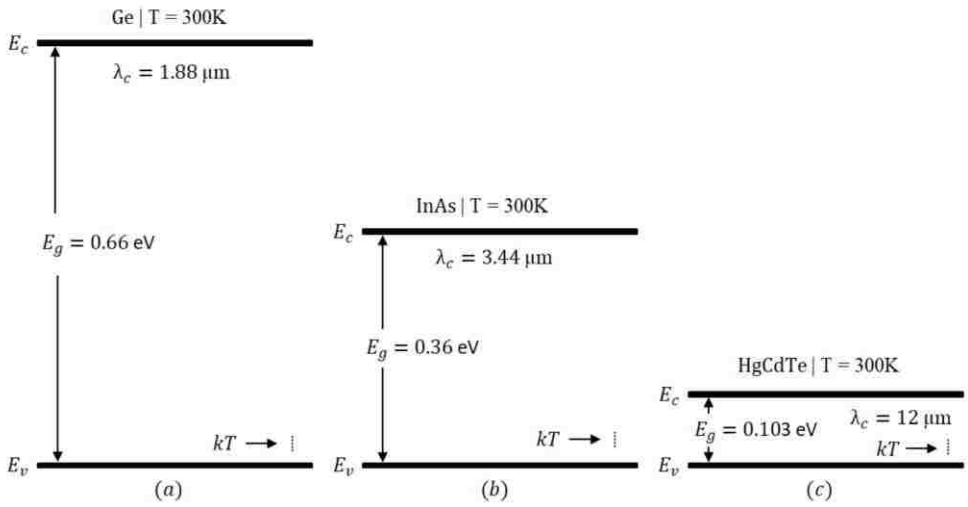

Figure 1.5: Energy bandgap diagrams for various semiconductors highlighting the increase in significance of thermal energy factor, *kT*, in smaller bandgaps.

For an intrinsic semiconductor at equilibrium, the density of charge carriers is dependent upon temperature and bandgap energy, proportional to [**6**]

$$n \propto T^{3/2} e^{-E_g/2kT}, \tag{1.5}$$

therefore cryogenic cooling is employed to decrease this *kT* factor in most MWIR and LWIR photodetectors. This reduces the normalized thermal generation rate which is desirable to minimize when creating a high performance photodetector [**7**].

The electronic and optical properties of semiconductors are derived from their atomic structure (crystalline) and periodicity. Atoms from group IV in the periodic table of elements are natural semiconductors (i.e. Si and Ge) , while atoms from groups II, III,

V, and VI may be used to create binary, ternary, and quaternary semiconducting compounds such GaAs, HgCdTe, and InGaAsP, respectively. These compounds are created by carefully combining two or more elements during crystal growth which results in a semiconductor with a bandgap energy that is an interpolation (not necessarily linear) between those of constituent elements. For example, the ternary compound $Hg_{1-x}Cd_xTe$ is created by controlling the proportions of HgTe and CdTe which enables the tuning of its energy bandgap according to [**8**]:

$$E_g = -0.302 + 1.93x + (5.35 \times 10^{-4})T(1-2x) - 0.310x^2 + 0.832x^3 \quad (1.6)$$

Fig. 1.6 shows E_g plotted vs *x*. Using this information one can design a $Hg_{1-x}Cd_xTe$ photo-detector tailored to specific IR applications with available detection wavelengths spanning from the SWIR to the FIR.

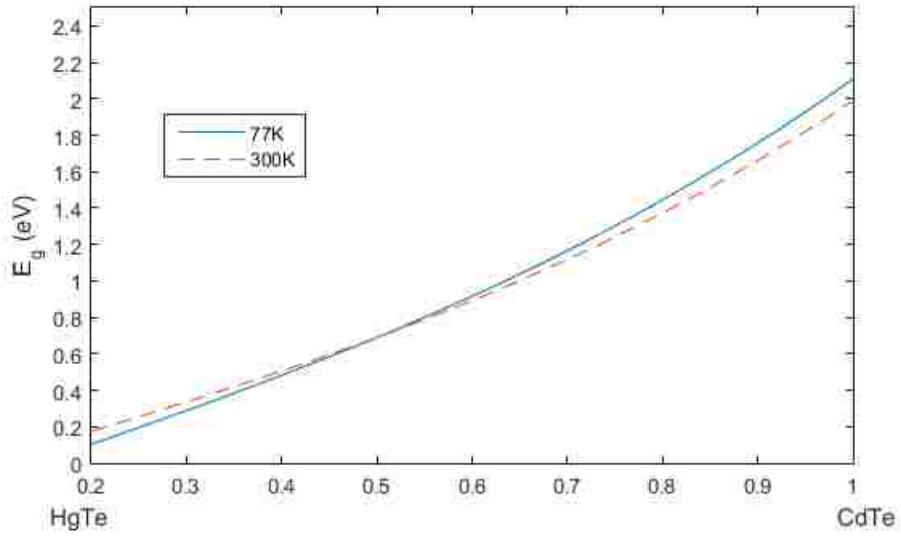

Figure 1.6: Energy bandgap tunability of HgCdTe.

This is highly convenient, however $Hg_{1-x}Cd_xTe$ is not he best solution for all IR applications and not all semiconducting elements can be mixed arbitrarily. This is partially due to differences in the natural atomic spacing and configuration in each

element's crystal lattice. When atoms having dissimilar lattice constants are forced together, compressive or tensile strain can alter electronic performance of the subsequent device. While this can lead to negative defects, strain can also be intentionally introduced to alter properties such as valence band structure and effective mass [**9**]. This is known as "strain engineering" and will be discussed in further detail later as it is relevant to many devices characterized in this work. Practical semiconductor compounds are shown in Figure 1.7 with solid lines indicating continuous bandgap energy tunability via mole ratios.

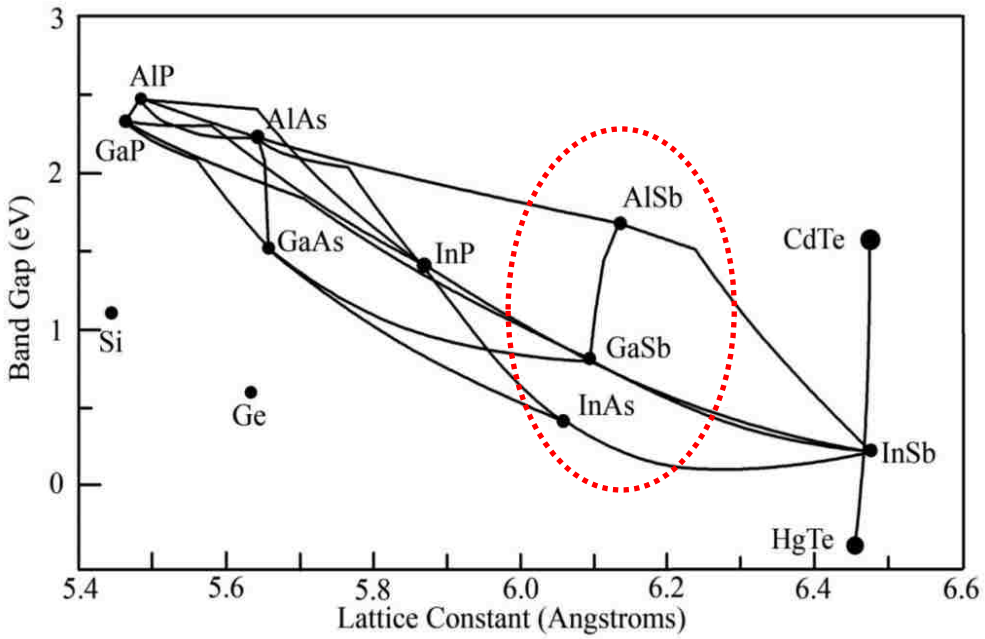

Figure 1.7: Energy bandgaps as a function of lattice constant highlighting the 6.1 Å group.

The focus of this work is to test the viability of newly developed semiconductor material systems combined with innovative device structures made from the 6.1 Å family (circled above) as superior alternatives for the long established, dominant HgCdTe technology in space-based photodetectors. Now that it has been established what is needed of

semiconductors to detect in the IR and why, recent efforts to improve the state of the art will be discussed.

1.3 Established vs. Emerging IR Detector Technologies

Lattice matching and energy bandgaps, as discussed above, are just a couple of many factors one must consider when designing a photodetector. Even if two different compounds can sense the same wavelengths, the differences in atomic structure may lead to only one being suitable for a particular application. Si and GaAs, for example, can both sense NIR wavelengths; however, since the electron mobility of GaAs is > 6x higher than that of Si, GaAs would make a better high speed detector for telecommunications. On the contrary, Si makes superior CMOS electronics due to its greater hole mobility. Substrate cost, atomic melting points, effective mass of charge carriers, domestic availability, fabrication yield, environment, and operating temperature all need to be considered when designing a high quality photodetector.

1.3.1 II-VI: HgCdTe

Researchers have spent over 50 years maturing and improving the performance of HgCdTe detectors and it is currently the dominant technology in the field. Its energy bandgap is highly tunable, as shown above, which makes it very versatile; however, it is challenging to grow and uncertainty in the mole fraction ratio during crystal growth, x in Eq. 1.6, can result in non-uniformities in cutoff wavelength, even among an array of adjacent pixels [**4**]. LWIR detectors are especially sensitive to this. Further improvement may be limited due to the minority carrier lifetimes reaching their intrinsic limit via

Auger recombination [**10**]. To further improve the state of the art of IR photo-detection, other material systems are currently being considered as viable alternatives.

1.3.2 III-V: 6.1 Å T2SL

IR detector development using Type-II superlattices (T2SL) has been a recent focus using the 6.1 Å family of materials (AlSb, GaSb, InAs) due to their longer intrinsic Auger lifetimes and abilities to sense longer wavelengths while operating at higher temperatures, relative to HgCdTe [**7**]. Multiple quantum wells (QW) with thin barrier layers between constitute a superlattice (SL). The thin barriers allow wave functions between neighboring quantum wells to overlap and charge carriers to tunnel through. The end result is a semiconductor with a synthesized, or engineered, energy bandgap smaller than those of the constituent semiconductor compounds [**11**]. This is illustrated in Figure 1.8. In Type-I SLs, the charge carriers are confined in the same layers, while in T2SLs the electrons and holes are confined in different layers.

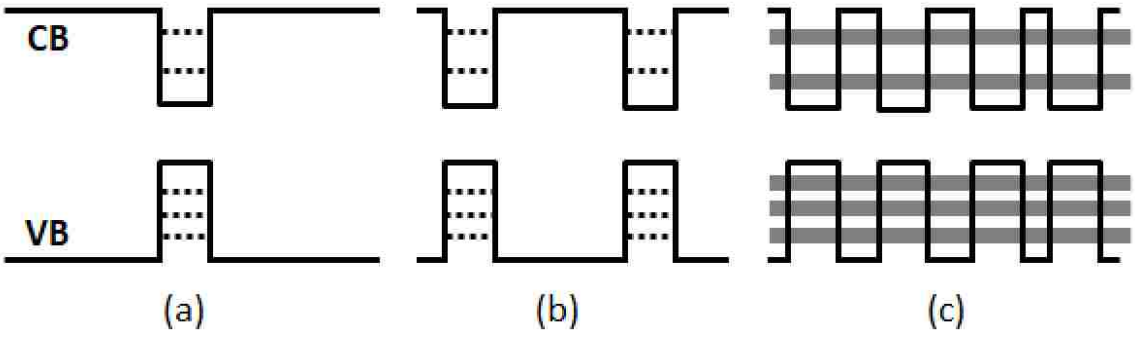

Figure 1.8: Quantum structures, where (a) is a single QW, (b) is two QWs, and (c) is an SL composed of multiple, closely spaced QWs.

This has been made possible with advances in crystal growth technology, specifically Molecular Beam Epitaxy (MBE), where it is possible to control periodicities and

symmetries of crystal lattices through application of very thin layers (on the order of a single atomic layer at a time) of each desired element or compound.

These systems were proposed for use in IR detectors in 1987 by D.L. Smith and C. Mailhiot [**12**] and shortly thereafter Youngdale *et al.* empirically demonstrated Auger lifetimes in an InAs/GaInSb T2SL material that were >100x superior (longer) than those in HgCdTe [**13**]. The significance of this is that these III-V T2SL systems, in theory, have better potential performance than that of HgCdTe due to more desirable (less restrictive) intrinsic limitations. Research and development efforts have been poured into these III-V T2SL material systems ever since in effort to push performance to their full theoretical potential. Sensitive photo-detection using these material systems have been demonstrated in both the MWIR [**14**,**15**,**16**,**17**] and LWIR [**18**]; however, overall performance to date has been hindered by short minority carrier lifetimes (much shorter than those of HgCdTe) attributed to high concentrations of Shockley-Read-Hall (SRH) recombination centers [**19**], which will be discussed in section 2.3.

Multiple efforts have been taken to improve the performance of these III-V T2SL material systems by incorporating potential barrier structures during crystal growth. These are intended to mitigate generation-recombination (G-R) currents caused by the SRH trap centers. Notable designs include the M-structure [**17**], W-structure [**20**], and *nBn* structure [**15**]. Many unipolar barrier detector structures were characterized in this work, and an example of an *nBn* detector structure is shown in Figure 1.9. The barriers have been proven to significantly reduce dark and surface currents by impeding the flow of majority carriers while still allowing free flow of the photo-generated minority carriers [**21**]; however, short minority carrier lifetimes remain problematic.

It was noticed in work by Svennson *et al.*, by varying the thicknesses of T2SL periods in InAs/GaSb, that carrier lifetime improved when GaSb content decreased [**22**].

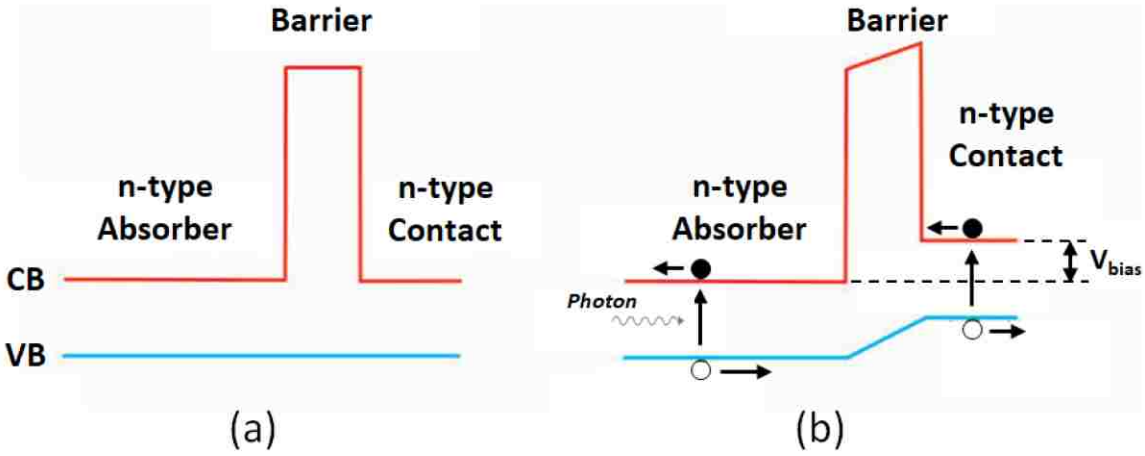

Figure 1.9: Energy band diagram of an ideal unipolar barrier detector structure: (a) unbiased, (b) biased.

This has led to an industry-wide change in research focus from the InAs/GaSb T2SL material system to that of the so-called "Ga-free" InAs/InAsSb T2SL in which Steenbergen *et al.* reported a significantly higher minority carrier lifetime in a LWIR energy bandgap of > 412 ns [**23**].

In summary, despite their current struggle with short minority carrier lifetime, III-V T2SL material systems have a number of attractive advantages over HgCdTe: crystal growth is easier to control resulting in higher uniformity across wafers [**24**], it has stronger atomic bonds and structural stability [**25**], its GaSb substrates are orders of magnitude less expensive than the CdZnTe used for HgCdTe [**4**], mature III-V growth and processing technologies stood up by the solid-state laser industry can be leveraged, effective masses combined with strain engineering reduce tunneling and Auger recombination [**26**], and domestic availability is not problematic.

1.4 Radiation Tolerance

Even if the full optoelectronic performance potential of these 6.1 Å T2SL IR detectors eventually becomes realized, they must also fare well in the harsh environment of space if they are to become viable alternatives to HgCdTe as space-based sensors. There has been much effort put into characterizing the degradation of electronics in these conditions, which are unavoidable for satellite-based detectors [**27**,**28**,**29**,**30**,**31**,**32**,**33**,**34**,**35**]. There, different species of charged particles (e.g. heavy ions, protons, and electrons) exist in spectra of kinetic energies which are highly location dependent (i.e. selected satellite orbit trajectory and altitude as shown in Figure 1.10).

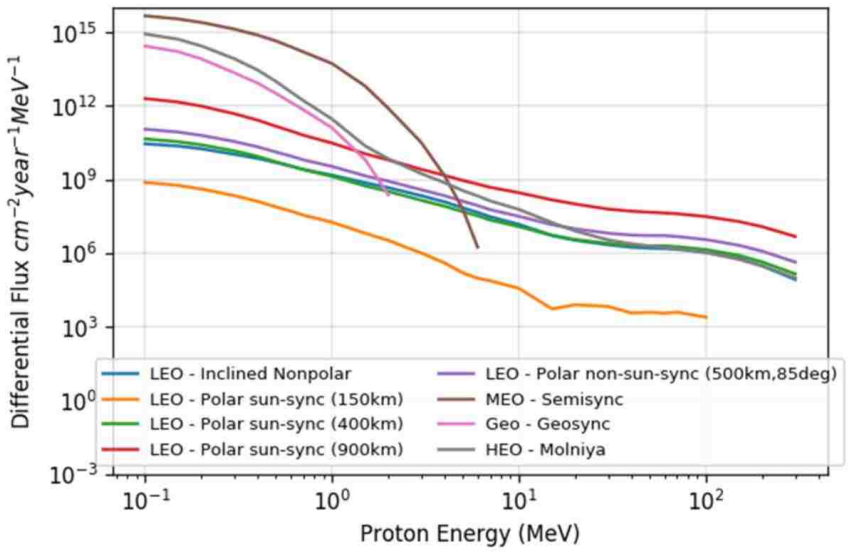

Figure 1.10: Kinetic energy spectra of protons vs. satellite orbit [**36**].

Earth's magnetic field captures the energetic charged particles from solar wind and cosmic rays, and they remain in belts circling the planet at altitudes from 500 to 58,000 km. James Van Allen is credited to their discovery, hence they are known as the Van

Allen radiation belts which are depicted in Figure 1.11. The inner and outer belts are dominated by protons and electrons, respectively.

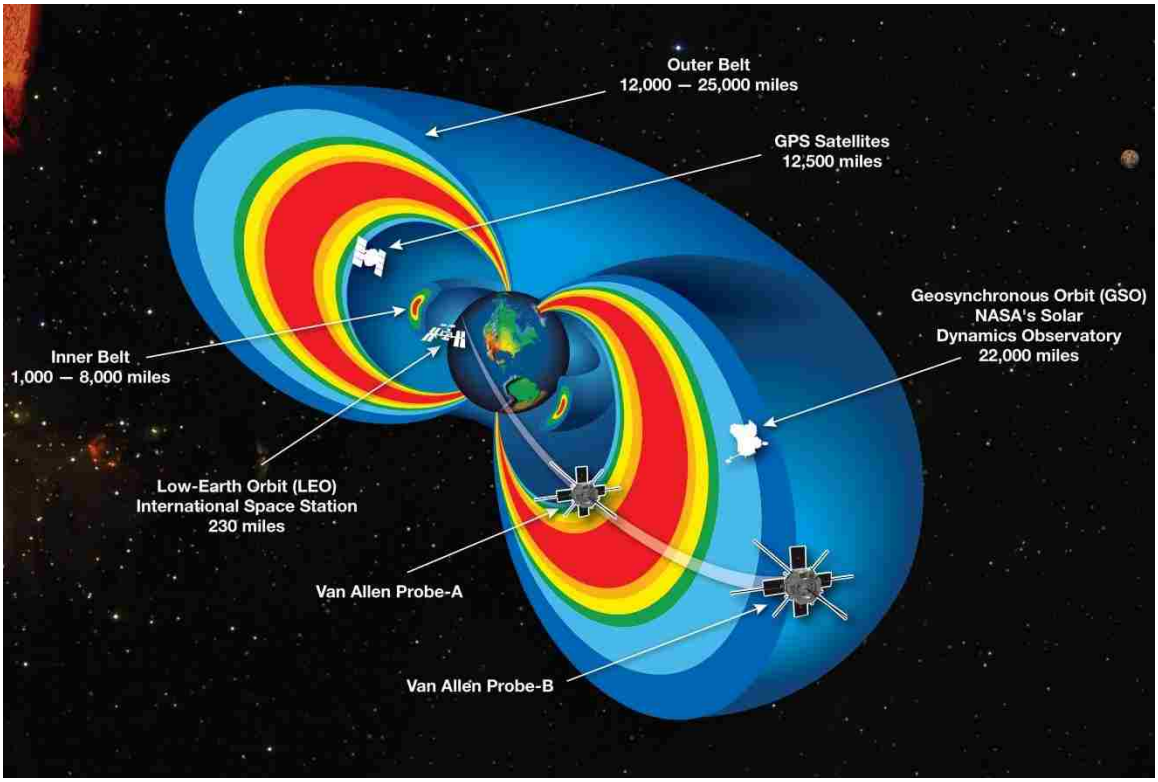

Figure 1.11: Van Allen Radiation Belts around Earth. Credit: NASA

Electronics in this environment can be affected by these charged particles through several different mechanisms which are listed in Table 1.2 for convenient comparison. Proton irradiation is the focus of this work as electrons are more easily shielded [**37**] and less dominant in orbits of interest intended for space-detectors discussed herein. In a study of radiation shielding by C. Dale *et al.* it was found that, not only does increasing shield thickness rapidly result in diminishing returns in proton mitigation, when charged particles travel through thicker metals (Ta and Al) they can actually increase radiation through the creation of secondary protons and neutrons with higher probability [**38**].

Table 1.2: Effects of the space environment on spacecraft electronics

Mechanism	Effect	Source
Total Ionizing Dose (TID)	Degradation of electronics	Trapped protons Trapped Electrons Solar Protons
Displacement Damage	Degradation of opto- and micro-electronics	Trapped protons Trapped Electrons Solar Protons Neutrons
Single-Event Effects	Data corruption Noise in data System shutdowns Electronic damage	Heavy ions Solar protons Trapped protons Neutrons
Surface Charging	Biasing of instrument readings Power drains Physical damage	Hot and cold plasma
Deep Dielectric Charging	Biasing of instrument readings Electrical discharges	High energy electrons

If the kinetic energy of a charged particle is high enough it will induce displacement damage in a semiconductor, which is the physical relocation of its atoms within its crystal lattice causing defects such as vacancy-interstitial pairs leading to important device-level electronic changes [**39**]. Most of its energy is spent ionizing atoms by creating electron-hole pairs, while the remaining ~0.1-1% is spent impacting atoms with elastic or inelastic nuclear collisions. This fractional energy that causes displacement damage is known as non-ionizing energy loss (NIEL). A more elegant definition of NIEL is *the energy a particle imparts to a solid through non-ionizing mechanisms*. This damage mechanism is explained in detail by Marshall and Marshall in regard to satellite sensor design [**40**].

By performing "ground-truth" irradiation experiments in controlled laboratory environments, the performance degradation of spacecraft electronics vs. charged particle

irradiation can be measured. Essentially, this accelerated aging of spacecraft electronics on the ground in effort to predict their long term survivability in space. "Damage factors," which are measured rates of change vs. charged particle irradiance, are assigned to optoelectronic parameters under test [**41**]. These damage factors are highly dependent on the kinetic energy; therefore they must be specified along with the energies used for each experiment. As counterintuitive as it may seem, proton-induced damage in semiconductors is stronger for lower energy protons as they are more probable to end up embedded in the crystal lattice. This has even been performed intentionally to create p-n junctions in HgCdTe as an alternative to the diffusion technique [**42**]. As will be shown in a later chapter, damage factors can be normalized and correlated to NIEL curves, which can be calculated given the weighted combination of constituent elements in a semiconductor [**43**]. This allows the extrapolation of damage factors through a continuum of charged particle energies, such as the proton spectra in Figure 1.10a. With this information, spacecraft mission planners can estimate the change in a parameter of interest due to charged particle irradiation over the mission life of a satellite using [**32**]:

$$\text{Carrier recombination rate, } \tau^{-1} = t_m \cdot \int_0^{\infty} \kappa_{\tau^{-1}}\left(E_{ref}\right) \frac{NIEL(E)}{NIEL(E_{ref})} \cdot \frac{d\varphi(E)}{dE} dE, \quad (1.7)$$

where t_m is the mission duration, $\kappa_{\tau^{-1}}$ is the recombination rate damage factor characterized at a proton kinetic energy of E_{ref}, *NIEL* values are from calculated curves at specified energies, and the final term is the differential proton energy spectrum similar to Figure 1.10.

Recent empirical work performed by Morath *et al.* quantified the performance degradation rates of III-V based *nBn* detector structures with various designs, materials, energy bandgaps, and operating temperatures vs. monoenergetic proton irradiation [**44**].

Here, relationships were established between 63 MeV proton irradiation damage factors for dark current density, lateral optical collection length, and quantum efficiency. It was concluded that these degradations stemmed from the displacement-damage-induced reduction of an unmeasured, lower-level parameter: *minority carrier recombination lifetime*. Hubbs *et al.* reached the same conclusion after performing ground-truth proton irradiation tests on a complete III-V *nBn* MWIR focal plane array (FPA) [**45**].

In this work, a measurement system was designed and constructed to directly measure the minority carrier recombination lifetimes of prototype IR detector structures at the wafer die level, to include both HgCdTe and the new 6.1 Å T2SL *nBn* technology being considered. It is unique for two reasons: 1) it is designed to be portable which allows *in-situ* lifetime characterization vs. stepwise proton irradiation by deploying it to radiation sources across the country, and 2) through cryogenic cooling, it maintains samples at mission operating temperatures throughout entire irradiation experiments which enables post-radiation annealing studies. The typical radiation test found in literature is a single, large dose performed on room temperature samples.

The main conclusions in this dissertation are derived from analyses on data acquired from this measurement system at a monoenergetic proton source. Radiation tolerances of the minority carrier lifetime and post-radiation annealing effects are compared between HgCdTe and 6.1 Å T2SL *nBn* detector structures, the effects of doping and other design parameters on the lifetime damage factors in III-V materials are investigated, and a damage factor vs. proton energy (NIEL) study was performed on III-V structures which will allow spacecraft mission planners to extrapolate lifetime damage factors in these materials through any proton differential energy spectra of interest.

Chapter 2

Charge Carrier Dynamics

2.1 Introduction

The goal of this chapter is to introduce terminology and provide an overview of fundamental semiconductor physics in effort to provide an understanding of the primary metric used in upcoming analyses. Multiple texts were used as general references [**6**,**46**,**47**,**48**]. It is assumed the reader is familiar with the concepts of conduction and valence energy bands derived from the application of quantum mechanics and Schrodinger's wave equation to bound particles in a crystalline lattice.

2.2 Semiconductors in Equilibrium

Equilibrium implies that no external forces are acting on the semiconductor. These include voltages, electric fields, magnetic fields, and temperature gradients. The distribution of electrons (*n*) and holes (*p*, lack of an electron) in the conduction and valence bands, respectively, with respect to energy (*E*) are expressed as

$$n(E) = g_c(E) f_F(E) \tag{2.1}$$

$$p(E) = g_v(E)[1 - f_F(E)] \tag{2.2}$$

where g_c and g_v are the density of quantum states in the conduction and valence bands, respectively, and f_F is the Fermi-Dirac probability function. The density of states

functions, derived from quantum mechanics, represent the number of allowed quantum states in which the respective charge carrier is allowed to reside and is defined as

$$g_c(E) = \frac{4\pi(2m_n^*)^{3/2}}{h^3} \cdot \sqrt{E - E_c} \tag{2.3}$$

$$g_v(E) = \frac{4\pi(2m_p^*)^{3/2}}{h^3} \cdot \sqrt{E_v - E} \tag{2.4}$$

where m_n^* and m_p^* are the density of states effective masses of electrons and holes, respectively, and E_c and E_v are the energy levels of the conduction and valence bands, and h is Planck's constant. The Fermi-Dirac function represents the probability of an electron occupying a state at the specified energy, and is expressed as

$$f_F = \frac{1}{1+e^{(E-E_F)/kT}} \tag{2.5}$$

where E_F is the Fermi energy level, *k* is Boltzmann's constant, and *T* is temperature. If E_F is several *kT* from both E_c and E_v then Eq. 2.5 can be reduced to the Boltzmann approximation by neglecting the *1* in the denominator. Eq. 2.5 can then be rewritten as

$$f_F = e^{-(E-E_F)/kT}. \tag{2.6}$$

To find the total number of equilibrium electrons (n_0) in the conduction band, an integral can be performed on the distribution in Eq. 2.1 from E_c to +∞:

$$n_0 = \int_{E_c}^{\infty} \frac{4\pi(2m_n^*)^{3/2}}{h^3} \cdot \sqrt{E - E_c} \cdot e^{-(E-E_F)/kT} dE. \tag{2.7}$$

After making a change of variable using the gamma function [**6**], Eq. 2.7 can be reduced:

$$n_0 = N_c e^{-(E_c-E_F)/kT} \tag{2.8}$$

Here, N_c represents the effective density of states function for the conduction band:

$$N_c = 2\left(\frac{2\pi m_n^* kT}{h^2}\right)^{3/2} \tag{2.9}$$

Following similar treatment for the equilibrium concentration of holes in the valence band (p_0), but integrating Eq. 2.2 from $-\infty$ to E_v, the analogs to Eq. 2.8-2.9 become

$$p_0 = N_v e^{-(E_F - E_v)/kT} \tag{2.10}$$

$$N_v = 2\left(\frac{2\pi m_p^* kT}{h^2}\right)^{3/2}. \tag{2.11}$$

2.2.1 Intrinsic Carrier Concentration

An intrinsic semiconductor has a perfect crystal lattice such that no impurities or dopants are present. In equilibrium the concentration of holes in the valence band equal the number of electrons in the conduction band: $n_0 = p_0$. The product of these carrier densities equal the square of the intrinsic carrier concentration, n_i and this is known as the law of mass action:

$$n_i^2 = n_0 p_0 = N_c N_v e^{-(E_c - E_v)/kT} = N_c N_v e^{-E_g/kT} \tag{2.12}$$

$$n_i = \sqrt{N_c N_v}\, e^{-E_g/kT} \tag{2.13}$$

where $E_g$is the bandgap energy of the semiconductor. Note that the intrinsic carrier concentration is constant for stable temperature and independent of the Fermi energy level. Under influence of external forces $np \neq n_i^2$ as will be explained in section 2.3. The power in using semiconductors to make practical devices, however, comes from adding impurities which alter electrical characteristics.

2.2.2 Extrinsic Carrier Concentration

Extrinsic semiconductors contain impurities or defects that create an inequality between electron and hole concentrations. The intentional addition of impurities in a semiconductor is called “doping,” and this process is carefully controlled to tailor electrical characteristics of the material. Doping can be either n-type or p-type depending on how many valence electrons reside in the added impurity atoms. Consider a Phosphorous atom added as a substitutional impurity to Si, for example. Being from group V in the period table, it has five valence electrons while Si only has four. When it replaces a Si atom in the lattice, four of the valence electrons will be covalently bonded to the surrounding Si atoms, and the fifth electron will be free to travel through the material. This is referred to as a donor impurity atom because it donates an electron to the conduction band of the Si lattice without creating a new hole in the valence band, in this case making the Si lattice more n-type. The opposite is true for acceptor impurity atoms (i.e. elements from groups II and III) which have less valence electrons than Si and readily accept electrons from the valence band, thereby adding a hole to the valence band without adding an electron to the conduction band. The ability of these impurities to add carriers to their associated energy bands is a function of temperature; however, their energy levels are typically close enough (described as “shallow”) to the valence or conductions bands such that minimal thermal excitation is needed for complete ionization.

The law of mass action from Eq. 2.12 also applies to extrinsic semiconductors as $n_i^2 = n_0 p_0$; however, in this case $n_0 \neq p_0$. The equilibrium carrier concentations may be

calculated for an extrinsic semiconductor starting with charge neutrality condition, which states that the density of positive charges must equal that of the negative charges:

$$n_0 + N_a^- = p_0 + N_d^+ \tag{2.14}$$

Here, N_a^- represents the acceptor impurity atom concentration which has become negatively charged ions after accepting electrons, and N_d^+ represents the donor impurity atom concentration which has become positively charged ions after donating their electrons to the conduction band. Using the law of mass action to substitute p_0 with n_i^2/n_0 (assuming semiconductor is more n-type doped and impurities are fully ionized), the quadratic formula may be used to find the equilibrium electron concentration:

$$\mathrm{n_0} = \frac{(N_D - N_A)}{2} + \sqrt{\left(\frac{N_D - N_A}{2}\right)^2 + n_i^2} \tag{2.15}$$

In n-type materials, since $n_0 > p_0$, electrons are considered the *majority* carrier while holes are considered the *minority* carrier. The minority carrier concentration in the example above can be calculated using the result of Eq. 2.15 and the law of mass action:

$$\mathrm{p_0} = \frac{n_i^2}{n_0} \tag{2.16}$$

It is important to note that at high temperatures Eq. 2.15 approaches $n_0 \cong n_i$ due to the strong temperature dependence of n_i shown in Eq. 2.13. In other words, extrinsic semiconductors approach intrinsic behavior at high temperatures.

The Fermi energy level, which may be thought of as a chemical potential, determines the statistical distribution of electrons and is a logarithmic function of impurity concentrations, where

$$\mathrm{E_f} = E_c - kT \ln\left(\frac{N_C}{n_0}\right) \tag{2.17}$$

$$\mathrm{E_f} = E_v + kT \ln\left(\frac{N_V}{p_0}\right) \tag{2.18}$$

In the above equations, if $N_d^+ \gg n_i$ then $n_0 = N_d^+$. Likewise, if $N_a^- \gg n_i$ then $p_0 = N_a^-$. For a compensated n-type semiconductor, $n_0 = N_d^+ - N_a^-$ and for a compensated p-type semiconductor $p_0 = N_a^- - N_d^+$. The Fermi energy is an important parameter in device operation because it remains constant throughout a system (e.g. in a p-n junction).

2.3 Semiconductors in Non-Equilibrium

When a semiconductor is perturbed by an external force, such as photons from a laser pulse demonstrated in this work, additional electrons and holes are created which can exist in addition to n_0 and p_0, thus the total carrier concentrations become

$$\mathrm{n} = n_0 + \delta n \tag{2.19}$$

$$\mathrm{p} = p_0 + \delta p \tag{2.20}$$

where δn and δp are the concentrations of "excess" electrons and holes, respectively. The law of mass action does not apply under these non-equilibrium circumstances, as

$$n\mathrm{p} = (n_0 + \delta n)(p_0 + \delta p) \neq n_i^2, \tag{2.21}$$

however the work herein is concerned with the time it takes for the system to return back to equilibrium. This occurs naturally through carrier recombination over certain lifetimes, or recombination rates, via several different mechanisms discussed below. At the top level, there are two different types of carrier recombination: *radiative* and *non-radiative*. Radiative recombination occurs when an electron in the conduction band recombines with a hole in the valence band and the excess energy is emitted in the form of a photon. Non-radiative recombination can be described as the absence of a photon when an electron-hole pair is annihilated, where the excess energy is transferred to the lattice by

formation of a phonon (thermal lattice vibration). In general, the total recombination rate (carrier density loss per unit time) can be described as

$$R_{total} = R_{radiative} + R_{non-radiative} \tag{2.22}$$

The two different non-radiative recombination mechanisms considered here are Shockley-Read-Hall (SRH) and Auger, the former a problem for new III-V detectors while the latter is intrinsically limiting the improvement of HgCdTe detectors. Each recombination mechanism contributes to the overall recombination lifetime of charge carriers in a material, and it will be shown that their relative dominance varies with temperature. The overall recombination rates and lifetimes, respectively, can be expressed as

$$R_{total} = R_{radiative} + R_{SRH} + R_{Auger} \tag{2.23}$$

$$\frac{1}{\tau_{total}} = \frac{1}{\tau_{radiative}} + \frac{1}{\tau_{SRH}} + \frac{1}{\tau_{Auger}} \tag{2.24}$$

2.3.1 Shockley-Read-Hall Recombination

The SRH theory presumes the existence of states in the forbidden energy gap (between E_v and E_c) at an energy E_T due to either atomic impurities or structural imperfections. These imperfections are commonly referred to as traps or recombination centers. There are four possible non-radiative actions for carriers interacting with SRH traps: 1) capture of a conduction band electron by an empty trap; 2) electron emission from an occupied trap to the conduction band; 3) electron emission from an occupied trap to the valence band, also known as hole capture; and 4) capture of a valence band electron by an

unoccupied trap, also known as hole emission. These scenarios are illustrated in Figure 2.1

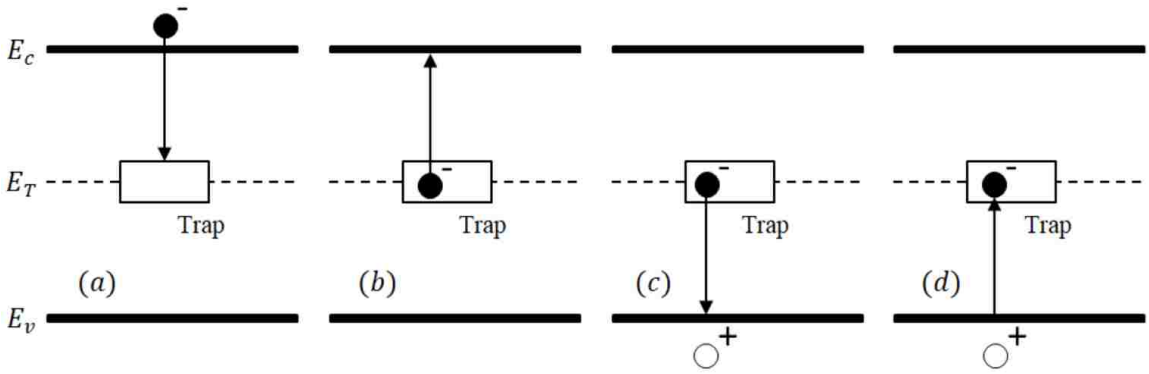

Figure 2.1: The four SRH recombination processes: (a) electron capture, (b) electron emission, (c) hole capture, and (d) hole emission.

In the models proposed by Shockley, Read and Hall circa 1950s, the recombination lifetime in a highly doped p-type semiconductor is determined by the minority carrier electron behavior [**49**,**50**]:

$$\tau_{n0} = \frac{1}{\sigma_n v_n N_t} \tag{2.25}$$

Likewise, the recombination lifetime in a highly doped n-type semiconductor is determined by the minority carrier hole behavior:

$$\tau_{p0} = \frac{1}{\sigma_p v_p N_t} \tag{2.26}$$

Here the subscripts indicate the carrier polarity, σ is the capture cross-section, and v is the thermal velocity of the subscripted carrier. The thermal velocities are also functions of mass according to

$$v_{n,p} = \left(\frac{3kT}{m_{n,p}}\right)^{1/2} \tag{2.27}$$

Each of the four SRH recombination sub-processes has its own associated recombination rate; however, the aforementioned authors formulated a net SRH recombination rate as

$$R_{SRH} = \frac{np - n_i^2}{\tau_{p0}(n + n_1) + \tau_{n0}(p + p_1)} \tag{2.28}$$

where n_1 and p_1 are the free electron and hole concentrations, respectively, that would exist if the Fermi energy level were located at the trap energy level, E_T. These can be expressed as

$$n_1 = N_c e^{(E_T - E_c)/kT} \qquad p_1 = N_v e^{(E_v - E_T)/kT} \tag{2.29}$$

Using the expressions for carrier concentrations in non-equilibrium (Eq. 2.19-2.20) and assuming a *low-level injection*, where the excess carrier densities are much lower than the background doping concentrations [$\delta n = \delta p \ll (n_0 + p_0)$], it can be shown that

$$\tau_{SRH} \cong \frac{\tau_{p0}(n_0 + n_1) + \tau_{n0}(p_0 + p_1)}{(n_0 + p_0)} \tag{2.30}$$

This is the SRH contribution to the minority carrier lifetime, and equals the minority carrier lifetime when SRH recombination is the dominant mechanism, as is the case with the 6.1 Å T2SL detector materials in this study. It is also important to note that the low-level injection condition is highly applicable to the materials studied herein as the excess carrier densities generated by impingent light upon a space-based detector can be approximated to be on the order of 1×10^{12} cm^{-3} [**51**] whereas a typical detector structure in this work has a background doping concentration $\geq 1 \times 10^{14}$ cm^{-3}.

In the case of *high-level injection*, where [$\delta n = \delta p \gg (n_0 + p_0)$], Eqs. 2.28 and 2.30 can be approximated to

$$R_{SRH} \cong \frac{\delta_n}{\tau_{p0} + \tau_{n0}} \tag{2.31}$$

$$\tau_{SRH} \cong \tau_{p0} + \tau_{n0} \tag{2.32}$$

The implications of high vs. low injection will be discussed in a subsequent chapter when the time dependence of δn is derived from the continuity equation.

As will be shown later with empirical studies, useful information about a semiconductor may be gained by characterizing carrier lifetimes vs. temperature. Each carrier recombination mechanism reacts differently to changes in temperature. The theory of these relationships will be discussed here in order to provide a basic understanding of upcoming analyses.

For trap concentrations with energy levels above mid-bandgap, there are three distinct temperature regions for the behavior of SRH recombination [**52**]:

Region I: $E_T < E_f < E_c$ $\qquad \tau_{SRH} \cong \tau_{p0}$ (2.33)

Region II: $E_i < E_f < E_T$ $\qquad \tau_{SRH} \cong \frac{N_c}{\tau_{p0} n_0} e^{-E_T/kT}$ (2.34)

Region III: $n_1 < n_i < p_1$ $\qquad \tau_{SRH} \propto e^{E_g/2kT - E_T/kT}$ (2.35)

In region I, the SRH lifetime scales with $T^{-1/2}$ due to the temperature dependence of the thermal velocity (see Eq. 2.26 and 2.27). In region II, the lifetime increases exponentially with temperature, and in region III the lifetime decreases exponentially with temperature. These relationships were simulated and plotted in Figure 2.2.

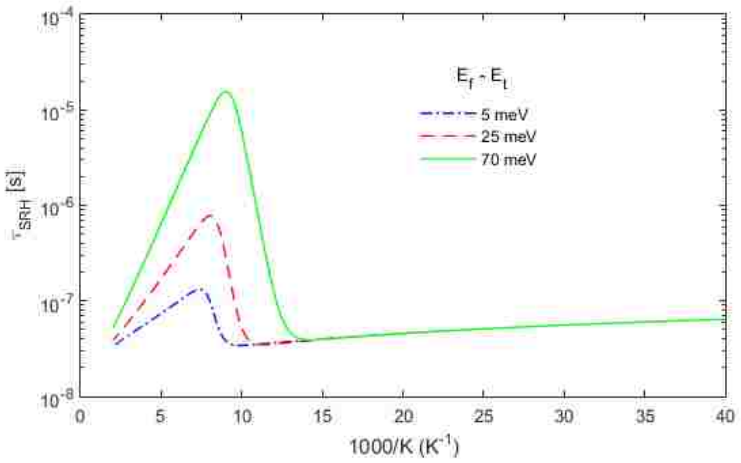

Figure 2.2: SRH recombination lifetime vs. temperature for three distinct regions.

The position of the defect energy level relative to the valence and conduction bands significantly affects the SRH lifetime. To illustrate this, τ_{SRH} was again simulated vs. temperature but for several different energy separations between E_c and E_T. See Fig. 2.3. An interesting takeway from this is that the closer the trap energy is to the middle of the bandgap, the shorter the SRH lifetime becomes.

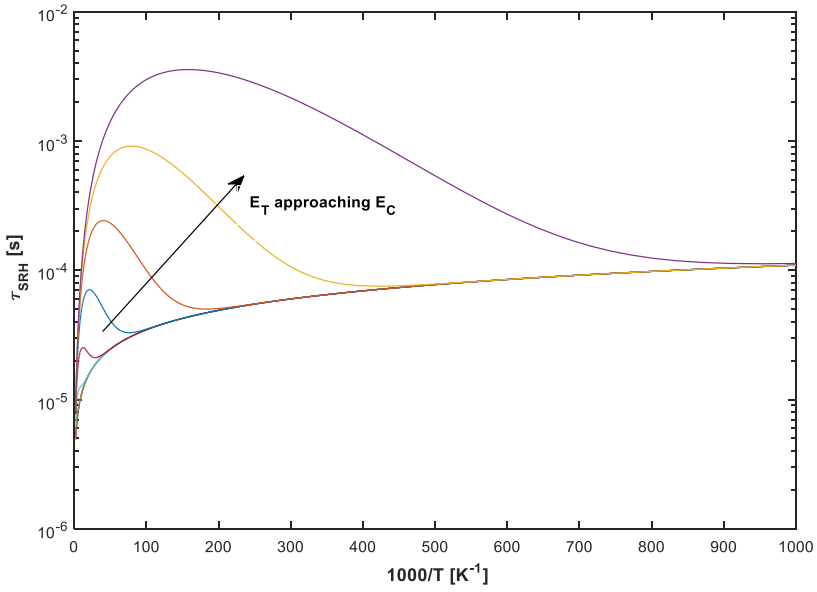

Figure 2.3: SRH recombination lifetime vs. temperature for various trap energy levels.

2.3.2 Radiative Recombination

Radiative recombination, also referred to as bimolecular recombination, occurs when an electron from the conduction band recombines with a hole in the valence band emitting the excess energy in the form of a photon. The radiative recombination rate can be specified for each carrier type and is proportional to the electron and hole concentrations

$$R_n = R_p = Bnp \tag{2.36}$$

where B is known as the radiative recombination coefficient. Without external perturbation, the net radiative recombination rate is

$$R_{rad} = B(np - n_0 p_0) \tag{2.37}$$

In non-equilibrium conditions the electron and hole concentrations become Eqs. 2.19 and 2.20 where it is assumed $\delta n = \delta p$. The radiative recombination rate for non-equilibrium becomes

$$R_{rad} = B(n_0 + p_0 + \delta n)\delta n \tag{2.38}$$

The general expression for the radiative recombination lifetime is

$$\tau_{rad} = \frac{1}{B(n_0 + p_0 + \delta n)} \tag{2.39}$$

and in *low-level injection* conditions described previously, the radiative recombination lifetime can be approximated as

$$\tau_{rad} \cong \frac{1}{B(n_0 + p_0)} \tag{2.40}$$

For *high-level injection*, Eqs. 2.38 and 2.39 can be approximated, respectively, as

$$R_{rad} \cong B(\delta n) \tag{2.41}$$

$$\tau_{rad} \cong \frac{1}{B\delta n} \tag{2.42}$$

Since the radiative recombination rate is shown to linearly increase with excess carrier concentration, it follows that higher injection yields more photons. This is the fundamental basis for light emitting diode (LED) and solid-state laser operation. However, if the injection of excess carriers becomes too high, an additional non-radiative recombination mechanism, Auger, will begin to dominate as it is a stronger function of excess carrier density.

The temperature dependence of radiative recombination stems from the $E_g^2/T^{3/2}$ factor in the expression for B [**53**]:

$$B = \frac{(2\pi)^{3/2}}{3} \cdot \frac{\hbar q^2}{m_0^2 c^2} \cdot n \left(\frac{m_0}{m_e + m_h}\right)^{3/2} \cdot \left(1 + \frac{m_0}{m_e} + \frac{m_0}{m_h}\right) \cdot \frac{E_g^2}{(kT)^{3/2}(m_0 c^2)^{1/2}} \qquad (2.43)$$

As the temperature approaches absolute zero, so does the radiative recombination rate coefficient. Above zero τ_{rad} will increase by the factor $T^{3/2}$ until intrinsic effects begin to dominate. When this occurs τ_{rad} will start decreasing exponentially. A simulation of this behavior is plotted in Figure 2.4.

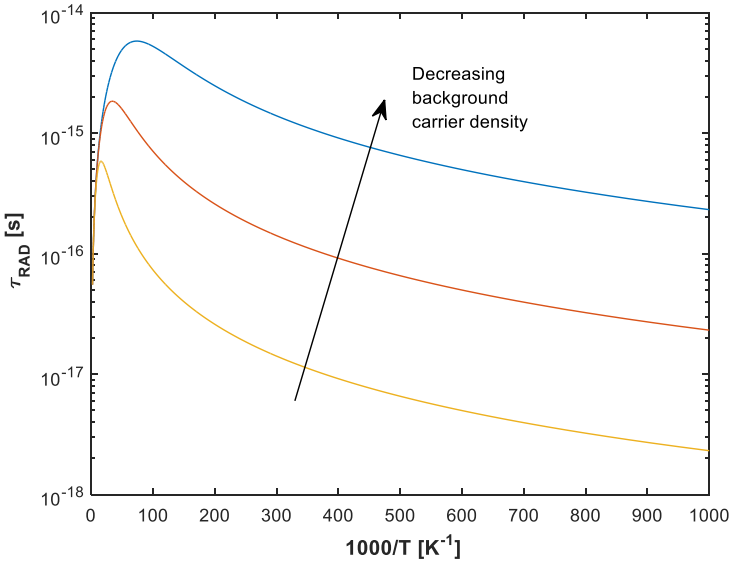

Figure 2.4: The dependency of radiative recombination on temperature.

2.3.3 Auger Recombination

Auger recombination is an inherently non-radiative, three-body process which is a strong function of excess carrier density, and therefore temperature. It involves either one electron and two holes or one hole and two electrons. A simplified diagram of each case is depicted in Fig. 2.5.

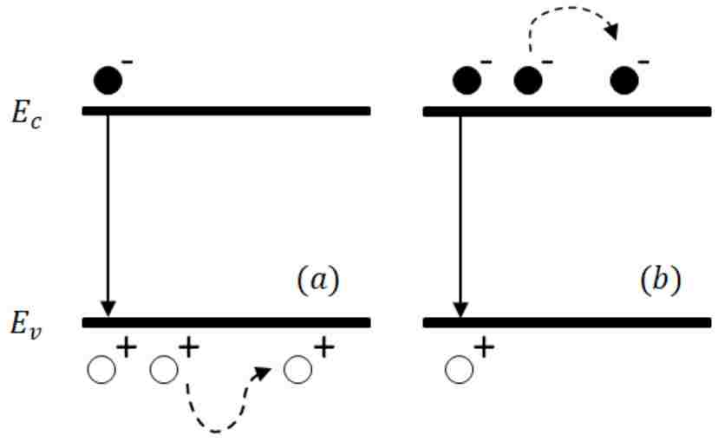

Figure 2.5: Energy level diagram of the Auger recombination process in which electron-hole recombination energy is imparted to 3rd party carriers, and subsequently into the lattice as phonons when they relax. Type (a) would be more prevalent in a heavily doped p-type material, while type (b) more prevalent in a heavily doped n-type material.

When a carrier recombines across the bandgap, instead of creating a photon, its excess energy is transferred toward the excitation of a neighboring carrier of the same polarity which subsequently emits a phonon as it relaxes back to its original energy in its respective band. The net Auger recombination rate can be expressed as

$$R_{Auger} = C_n\left(\frac{np-n_i^2}{n_i^2}\right)\left(\frac{n}{n_o}\right) + C_p\left(\frac{np-n_i^2}{n_i^2}\right)\left(\frac{p}{p_o}\right) \tag{2.44}$$

where C_p and C_n are coefficients for the cases in Fig. 2.5a and 2.5b, respectively. Expressed in terms of lifetime, Eq. 2.44 can be rewritten as

$$\tau_{Auger} = \frac{n_i^4}{(n_o+p_o+\delta)(np_oC_n+pn_oC_p)} \tag{2.45}$$

There are several different subtypes of Auger recombination depending on which energy bands are involved, for instance the valence band interactions can have contributions from the light-hole, heavy-hole, or split-off bands depicted in Fig. 2.6.

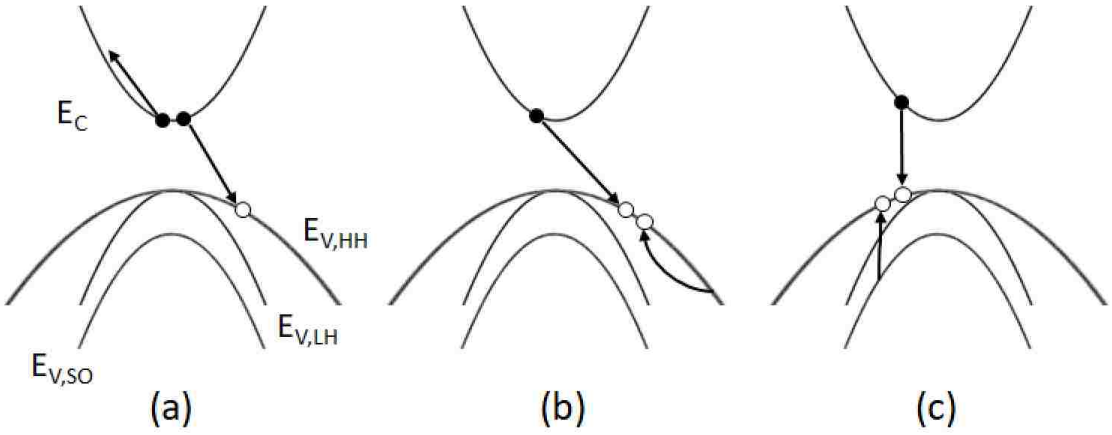

Figure 2.6:Auger recombination mechanisms:(a) AM1, (b) AM3, (c) AM7

For a nondegenerate n-type semiconductor, like the materials characterized in this dissertation, it can be assumed the AM1 process is the primary sub-process for Auger recombination. According to [**54**], C_n may be expressed as

$$C_n = \frac{8(2\pi)^{5/2}q^4m_o}{h^3} \cdot \frac{(m_nm_o)|F_1F_2|^2n_o(kT/E_g)^{3/2}}{\varepsilon_\infty^2(1+\mu)^{1/2}(1+2\mu)} \cdot e^{\left[-\left(\frac{1+2\mu}{1+\mu}\right)\left(\frac{Eg}{kT}\right)\right]} \tag{2.46}$$

where ε_∞ is the dielectric constant at high frequency, $\mu = m_n/m_h$, and $|F_1F_2|$ is the overlap of the Bloch function between involved states. For an intrinsic semiconductor with *low-level injection*, Eq. 2.45 may be approximated as

$$\tau_{Auger}^i \cong \frac{n_i}{2C_n} \tag{2.47}$$

If the semiconductor is n-type extrinsic under *low-level injection*, the Auger lifetime may be approximated in terms of the intrinsic lifetime as

$$\tau_{Auger} \cong \frac{2n_i^2}{(n_o+p_o)n_o} \cdot \tau_{Auger}^i \tag{2.48}$$

A simulation of the Auger lifetime in these example conditions is plotted in Fig. 2.7. Multiple concentrations of background carriers are included to emphasize their strong effect on recombination lifetime.

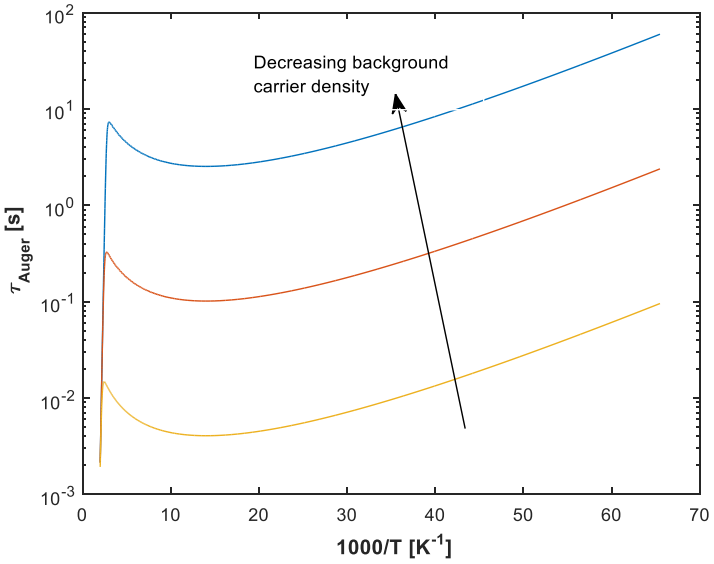

Figure 2.7: The dependence of Auger recombination on temperature.

2.4 Application to Optoelectronic Devices

As described in section 1.2, photo-detection is based on the photo-electric effect during which an electron-hole-pair (ehp) is generated through the transfer of photon energy to an atom. These photo-generated electrons and holes are then able to move around the crystalline lattice (carrying charge, the movement of which is the definition of electrical current) of a semiconductor until they are annihilated through one of the recombination mechanisms outlined above. Each carrier type has the same electric charge magnitude, $q = 1.60 \times 10^{-19}$ C, but opposite polarity where the electron is negative and hole is

positive. If electrical contacts are applied to a semiconductor, and the charge carriers persist long enough to reach them, these photo-generated electrons and holes may be sensed (known as collected) by circuitry, thereby creating photon-to-electron transduction enabling the construction of light-sensing devices.

It is important to understand that there are two different carrier transport mechanisms that can contribute to photo-generated current: *drift* and *diffusion*. These are processes by which electrons and holes move within a semiconductor. Drift is the movement of charge due to electric fields, such as an applied bias voltage, and diffusion is the flow of charge due to carrier density gradients. Since transport of electrons and holes each contribute to total current, there are four subcomponents: electron drift, hole drift, electron diffusion, and hole diffusion. These are shown, in respective order, in the three-dimensional equation for total current density [A/cm^2] below:

$$J_{total} = J_{drift} + J_{diffusion} = qn\mu_n E + qp\mu_p E + qD_n \nabla n - qD_p \nabla p \qquad (2.49)$$

The drift and diffusion subcomponents are generalized, respectively, as

$$J_{drift} = qE\left(n\mu_n + p\mu_p\right) \qquad (2.50)$$

$$J_{diffusion} = q\left(D_n \nabla n - D_p \nabla p\right) \qquad (2.51)$$

where E is an electric field [V/cm], n and p are electron and hole concentrations [cm^{-3}], $D_{n,p}$ is the diffusion coefficient (also known as diffusivity) for the subscripted carrier type [cm^2/s], and $\mu_{n,p}$ is the mobility coefficient of the subscripted carrier type [cm^2/V-s]. The diffusivity and mobility parameters are not independent of each other and can be expressed using the *Einstein relation* below:

$$\frac{D_n}{\mu_n} = \frac{D_p}{\mu_p} = \frac{kT}{q} \qquad (2.52)$$

The diffusivity indicates how well a carrier is transported in a semiconductor given a carrier concentration gradient, and the mobility indicates how well a carrier is transported in a semiconductor given the force of an electric field.

Creative engineering is required to maximize the collection probability of photo-generated carriers, specifically by separating them by polarity to avoid early recombination. Two different charge collection schemes will be discussed below: that of p-n photodiodes most commonly used in everyday devices which has both drift and diffusion components, and that of the relatively new *nBn* structures being developed for high performance IR imaging (characterized in this work) which rely almost solely on diffusion. It is hypothesized that the choice of collection scheme is consequential to the radiation tolerance performance of a detector.

2.4.1 p-n Junction Photodiodes

A p-n junction is constructed by conjoining (sequentially through growth) extrinsic p-type and n-type semiconductors. The majority carriers from each side diffuse into the other; however the atoms near the junction losing their charge carriers to diffusion become ionized, and this creates an electric field opposing further diffusion, therefore maintaining equilibrium. This is demonstrated in Fig. 2.8.

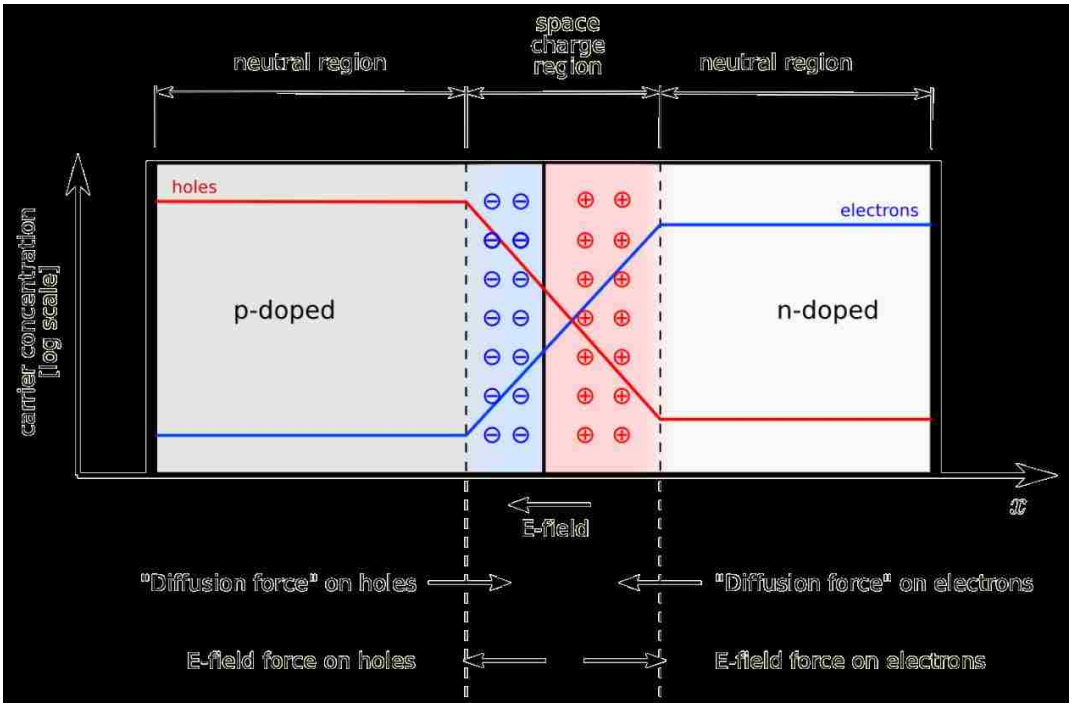

Figure 2.8: Schematic of a p-n junction

This “built-in” electric field creates a depletion region, also known as a space charge region, in which there exist no charge carriers. With electrical contacts, a photodiode can be created through application of a reverse bias (positive and negative voltages on n-type and p-type sides, respectively) which serves to widen the depletion region via stronger electric field. When impingent photons create electron-hole pairs in the depletion region, the electric field quickly prevents immediate recombination by separating the electrons from the holes, each carrier type drifting toward opposite neutral regions, subsequently reaching electrical contacts for collection. In addition to this drift current, carriers that are photo-generated in either neutral region within one diffusion length of the space charge region have a chance at diffusing into the space charge region then drifting toward contacts via the electric field. The diffusion length is highly dependent on the minority carrier lifetime and is defined for electrons and holes below, respectively, as

$$L_D^n = \sqrt{D_n \tau_n} \tag{2.53}$$

$$L_D^p = \sqrt{D_p \tau_p} \tag{2.54}$$

and may be described as the average distance each charge carrier travels before annihilation through recombination.

2.4.2 *nBn* Structure

The most popular unipolar barrier detector design is that of the *nBn* structure, where the term *nBn* refers to the device composition: n-type contact | Barrier | n-type absorber. This is demonstrated in Figure 2.9.

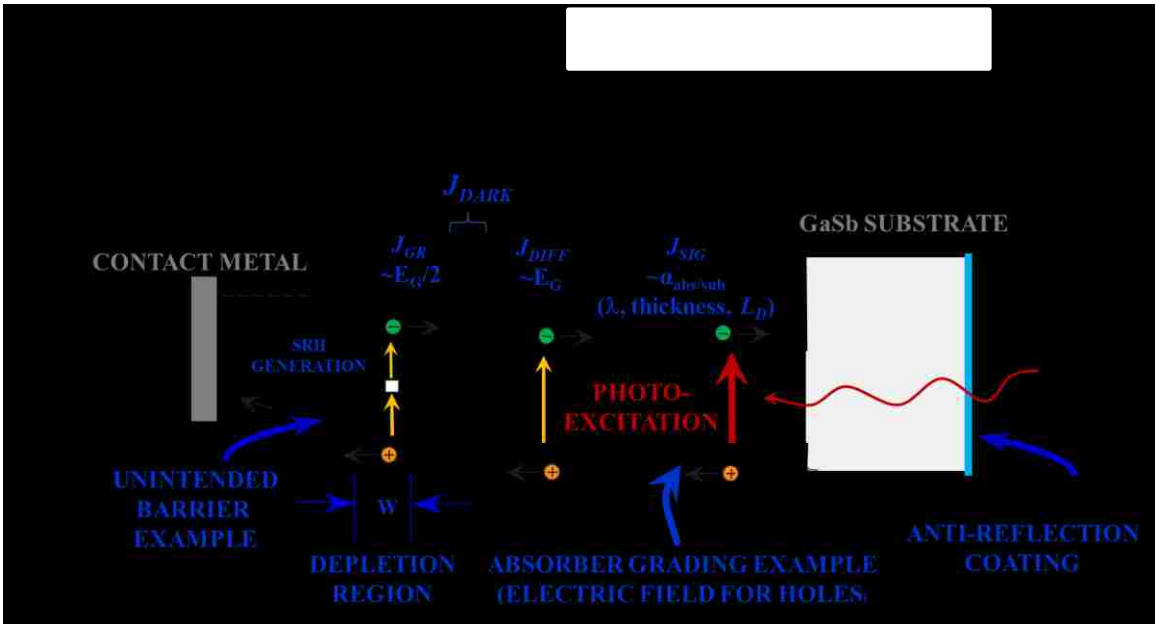

Figure 2.9: *nBn* detector structure with slight E-field due to graded absorber

The function of a unipolar barrier is to block the flow of one carrier type without impeding the flow of the other. In the *nBn* structure, electrons (majority carriers) are blocked while holes (minority carriers) are allowed to diffuse to the contact as photo-

current (signal) with the help of band-bending from a reverse bias voltage. The significance of impeding majority carrier flow is the removal of dark current sources such as surface recombination and G-R due to SRH recombination. To visualize this, an Arrhenius plot (dark current vs inverse temperature) is shown in Figure 2.10 comparing the different dark current behaviors between *nBn* and conventional p-n devices. Dark diffusion current varies as $T^3 e^{-E_g/kT}$ whereas dark G-R current varies as $T^{3/2} e^{-E_g/2kT}$ [**55**]. Since there is no depletion region in *nBn* devices in which G-R may occur, dark current due to G-R is totally suppressed causing the Arrhenius curves of the different devices to separate. This gives *nBn* devices two significant advantages in temperature regions where the curves are separated: 1) they can operate at warmer temperatures with the same dark current as a conventional p-n device, and 2) they can provide higher sensitivity, or signal-to-noise-ratio (SNR), than a conventional p-n device while operating at the same temperature. This is highly attractive to the IR sensing community due to the great cost and complexity of on-board cooling systems required for mitigating this noise.

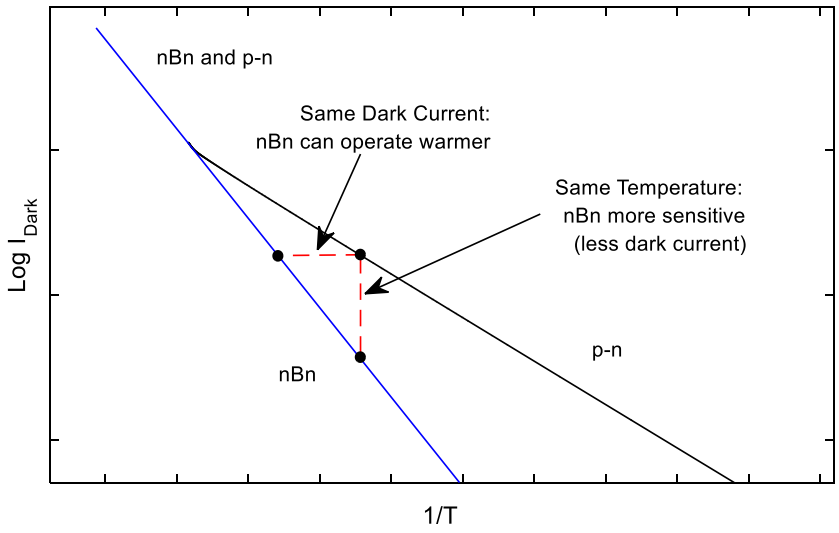

Figure 2.10: Arrhenius plot of dark current comparing *nBn* vs conventional p-n devices.

Although *nBn* devices may be fabricated in bulk semiconductor materials, as was done in the original demonstration by Maimon and Wicks [**21**], it has been found advantageous to use T2SL absorbers for several reasons [**56**]. First, it is important to understand that careful engineering must be exhibited in growing these barriers. Besides its location within the structure, which determines what current sources will be blocked [**57**], an ideal *nBn* barrier will have zero valence band offset (VBO), a large conduction band offset, and will be lattice-matched to its surrounding n-type materials (contact and absorber). One benefit of using a T2SL absorber is being able to tune (by carefully designed superlattice and growth) the conduction and valence band energies separately, making it easier to achieve zero VBO while still obtaining a desired absorber energy bandgap (detection cutoff wavelength). Another benefit is their inherently low Auger recombination rates due to electrons and holes residing in different layers, increasing minority carrier lifetime. The 6.1 Å group of III-V materials are an attractive option for creating T2SL *nBn* devices due to their very similar lattice constants and the several other reasons already discussed. This is the current focus of many research and development efforts, and more detail about barrier infrared detectors and related experiments can be found in the literature [**58**] [**59**] [**60**] [**61**] [**62**] [**63**] [**64**].

2.4.3 Performance Metrics

Regardless of charge carrier collection technique, each detector will have associated metrics for sensitivity and noise. Although there are many figures of merit, here the focus will be on quantum efficiency and dark current for sensitivity and noise, respectively, as the degradation of which are typically reported vs. charged particle fluence in ground-

truth radiation experiments. Quantum efficiency (denoted QE or η) is the ratio of how many photo-generated charge carriers are collected to how many photons are impingent upon the detector. For the conventional p-n junction photodetector, the quantum efficiency is expressed as

$$\eta_{p-n} = (1 - R)\left[1 - \frac{e^{-\alpha W_D}}{1+\alpha L_D}\right] \tag{2.55}$$

where R is the reflection coefficient, α is the absorption coefficient, W_D is the width of the depletion region, and L_D is the diffusion length of the minority charge carrier. For the *nBn* detector, which has no depletion region, the quantum efficiency is expressed as [**45**]

$$\eta_{nBn} = \left(\frac{\alpha L_D}{\alpha^2 L_D^2 - 1}\right) \times \left[\frac{\alpha L_D - e^{-\alpha L_A}\sinh(L_A/L_D)}{\cosh(L_A/L_D)} - \alpha L_D e^{-\alpha L_D}\right] \tag{2.56}$$

where L_A is the length of the absorber material. Since the *nBn* detector relies solely on diffusion for photo-collection, it is important that the diffusion length of the minority carriers be longer than the length of the absorber region, otherwise the photo-generated electron-hole pairs will likely annihilate each other through recombination before collection. Figure 2.11 provides a simulated comparison of quantum efficiency as a function of minority carrier lifetime between these device types. Recall from Equations 2.53-54 that L_D is proportional to $\sqrt{\tau}$. This is important due to the assumption that reductions in minority carrier lifetimes are directly related to increases in proton fluence.

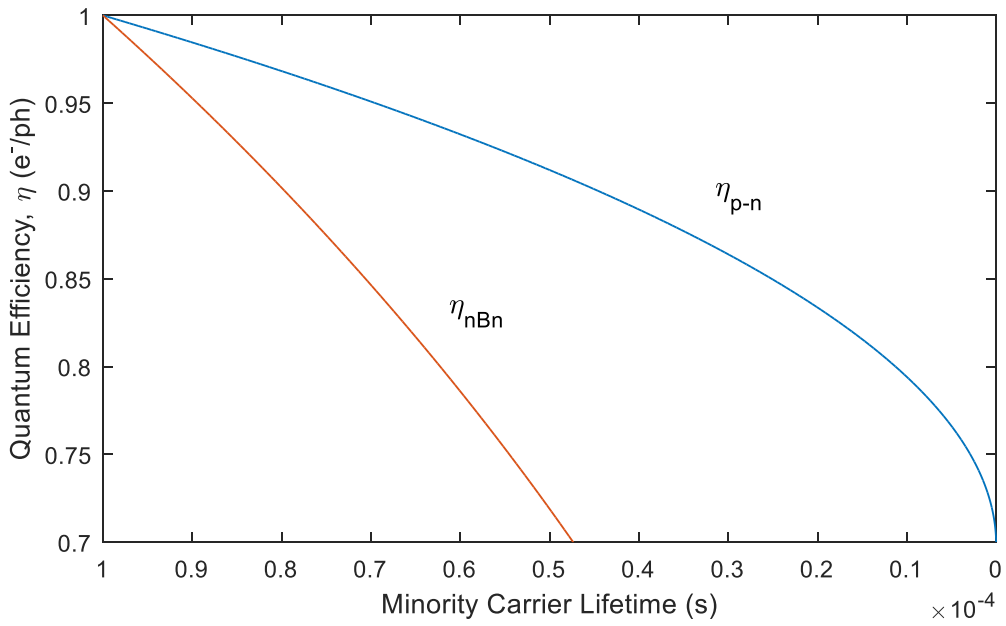

Figure 2.11: Quantum efficiency vs. minority carrier lifetime for a conventional p-n junction and *nBn* detector

It is obvious from this simulation that the sensitivity of *nBn* detectors has a stronger dependence upon minority carrier lifetime.

The temperature dependencies of the dark currents for each of these devices were compared in the previous section; however, they are also functions of diffusion length, and therefore minority carrier lifetime. For the p-n junction, the dark current is proportional the reverse saturation current of a diode

$$J_{D,p-n} \propto J_0 = q\left(\frac{n_p D_n}{L_n} + \frac{p_n D_p}{L_p}\right) \tag{2.57}$$

Therefore the p-n junction dark current scales with minority carrier lifetime as $\tau^{-1/2}$. The *nBn* detector has two different dark current regimes dependent on the width of the diffusion length relative to that of the absorber region. For $L_D \gg L_A$, which is the desirable case, the dark current for an *nBn* detector may be expressed as [**65**]

$$J_{D,nBn} = \frac{qn_i^2 L_A}{N_D \tau} \tag{2.58}$$

In the other regime, where $L_D \ll L_A$ the dark current for an *nBn* detector transitions to

$$J_{D,nBn} = \frac{qn_i^2}{N_D}\sqrt{\frac{D}{\tau}} \tag{2.59}$$

The transition to the 2nd, less desirable, regime is expected to occur only at high proton fluence levels which are expected to reduce the diffusion length via decreased minority carrier lifetimes.

2.5 Summary

The semiconductor physics relevant to two different infrared photodetector types, as well as the characterization method to be introduced in the next chapter, were discussed in detail. The competing detector architectures and their different charge collection schemes were compared as were some basic performance metrics as functions of both temperature and minority carrier lifetime, the latter of which is expected to decrease with increasing charged-particle fluence. The *nBn* detector certainly has multiple advantages (lower cost, higher operating temperatures, etc.), however its overall performance having stronger dependence on minority carrier lifetime, relative to the conventional p-n junction architecture, may ultimately prevent it from usurping the proverbial throne in radiation environments in which HgCdTe is seated.

After decades of being the dominant performer, HgCdTe may finally have a worthy competitor in the form of 6.1 Å T2SL *nBn* devices. In fact, it has already been deployed in terrestrial applications by the military [**66**]; however, space-based detectors have more stringent requirements and it is yet to be determined if HgCdTe will soon be

ousted from this arena. The work discussed in the following chapters was performed in effort to aid such determinations for the infrared space-based detector community by comparing the radiation tolerances, through direct measurement, of the minority carrier lifetimes between conventional p-n junction HgCdTe (II-VI) and T2SL *nBn* (III-V) devices, specifically InAs/InAsSb.

Now that the relevant terminology, fundamental physics, and device structures of interest have been introduced, the minority carrier lifetime characterization technique employed in this work will be discussed in detail.

Chapter 3

Experimental

3.1 Introduction

As mentioned in section 1.4, previous ground-truth radiation experiments deduced that the main culprit for IR detector performance degradation (i.e. quantum efficiency, dark current) was decreasing minority carrier lifetime with increasing proton fluence, specifically displacement damage. In this work, a characterization system was designed and implemented to directly measure minority carrier recombination lifetime as a function of accumulated proton fluence. Lifetime characterization itself is nothing new, and there are several different techniques used quite commonly across multiple industries; however, this system is unique in that it was designed to be portable in order to be deployed to radiation sources across the country while maintaining samples at cryogenic temperatures throughout the entire duration of these experiments. This cryogenic temperature control also enables post-radiation annealing studies, which have yielded interesting information on differences between II-VI and III-V detector materials. The typical ground-truth experiment found in the literature is performed with one large proton fluence dose at room temperature, whereas the experiments performed in this work were performed with multiple, smaller doses (with lifetime characterizations between) with samples maintained at temperatures representative of operating conditions

a space-based detector would likely see on orbit. The following sections will detail different aspects of the characterization system and experiments able to be performed with it, to include: samples, optics, excess carrier injection, portability, temperature control, automation, radiation test protocol, data acquisition and data analysis. In addition, there will be a discussion about the radiation source used in this work.

3.2 Time-Resolved-Photoluminescence

The lifetime characterization technique chosen for this work was time-resolved-photoluminescence (TRPL). Pros and cons of this method vs. others will be discussed at the end of this dissertation. Here, concentrations of excess, photo-generated carriers are generated, commonly described as 'injected', into semiconductor samples via laser pulses to induce non-equilibrium. Between laser pulses, these excess carriers recombine via the various mechanisms described in Chapter 2. The amplitude of the photoluminescence (PL) emitted from the sample via radiative recombination is recorded as a function of time and can be described as a PL transient. The minority carrier lifetime, given optimal conditions (namely low-level injection), is extracted as the time constant of a single exponential curve fitted to the PL transient based on the following general solution by Ahrenkiel and Lundstrom [**67**], starting with the continuity equation which describes the temporal rate of change of the excess carrier concentration:

$$\frac{d\Delta p}{dt} = -r(N_D \Delta p + \Delta p^2), \tag{3.1}$$

where Δp is the minority carrier hole concentration (assuming an n-type material), N_D represents the majority carrier electron concentration, and r is the recombination rate expressed as

$$r = \frac{N_t \sigma_p v_{th}}{N_D}, \tag{3.2}$$

where N_t is the defect, or trap, density, σ_p is the minority carrier hole capture cross section, and v_{th} is the thermal velocity of the minority carrier holes. In the low-level injection condition, the squared term in Eq. 3.1 may be omitted which simplifies its solution to

$$\Delta p(t) = \Delta p_0 e^{-rN_D t} = \Delta p_0 e^{-t/\tau}, \tag{3.3}$$

where p_0 represents the initial concentration of excess minority carrier holes at time = 0. This is the curve-fitting equation used in this work, and low-level injection is always attempted; however, it should be noted that to accurately extract an absolute minority carrier lifetime, one must account for the effects of photon recycling and surface recombination. Here, for simplicity and for the sake of comparing results of widely varying samples, τ will be considered an *effective* lifetime, a close but underestimated approximation of the true minority carrier lifetime. Outside the low-level injection condition the solution to Eq. 3.1 becomes non-exponential, and under high-level injection the effective lifetime approaches the sum of the majority and minority carrier lifetimes [**68**]. Simulated transients for low-level injection are shown in Figure 3.1 for various minority carrier lifetime values and are representative of typical data acquired by this measurement system.

The laser used to inject excess carriers must be of an appropriate wavelength such that the photons have enough energy to create electron-hole pairs across the bandgap of the material being probed, but not so energetic that all the photons get absorbed by the surface rather than the intended absorbing region. In this work, a laser with λ = 1535 nm

was used with a pulse energy and FWHM width of 8.9 µJ and 3.34 ns, respectively. The

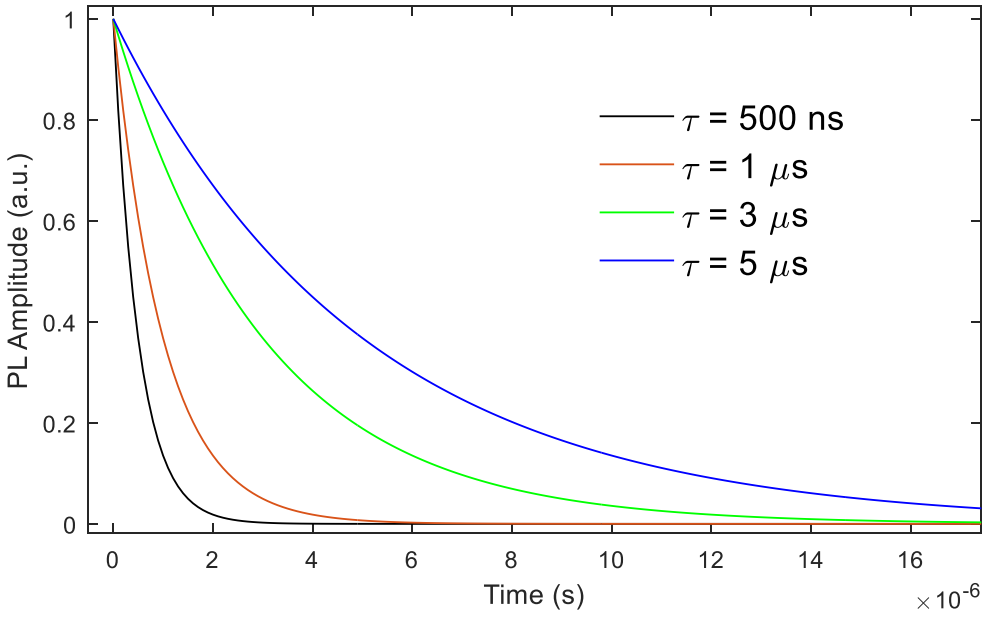

Figure 3.1: Simulated PL transients resulting from low-level injection

repetition rate of the pulses was 2.88 kHz, or ~350 µs period, which was plenty of time for the recombination phenomena to take place and carriers to relax back to equilibrium before the next pulse. Additionally, it is important that the pulse width be much shorter than the carrier lifetimes of samples being probed such that it may be approximated as an impulse function, which is valid in this work. Finally, care was taken in placement of the laser relative to the samples such that its natural Gaussian beam divergence resulted in a spot size diameter approximately equal to that of the sample under test (~1 cm^2). This ensured uniform illumination, or excess carrier injection, across samples.

Although the typical sample is a 5 x 5 mm to 1 x 1 cm square, PL from an area comprising only a 2 mm diameter in the center of each sample was imaged onto a detector, as shown in Figure 3.2, to record PL transients. This is due to the use of single

pixel, 1 mm^2 detector coupled with f/2 optics. A 2" diameter, off-axis (90º) gold, f/2, parabolic mirror was positioned a focal length away from the samples (4") to capture emitted PL, collimate it, and reflect it to a secondary mirror. The secondary mirror was of the same design, but was f/1 with half the focal length, which served to focus the collimated PL onto the 1 mm^2 detector pixel.

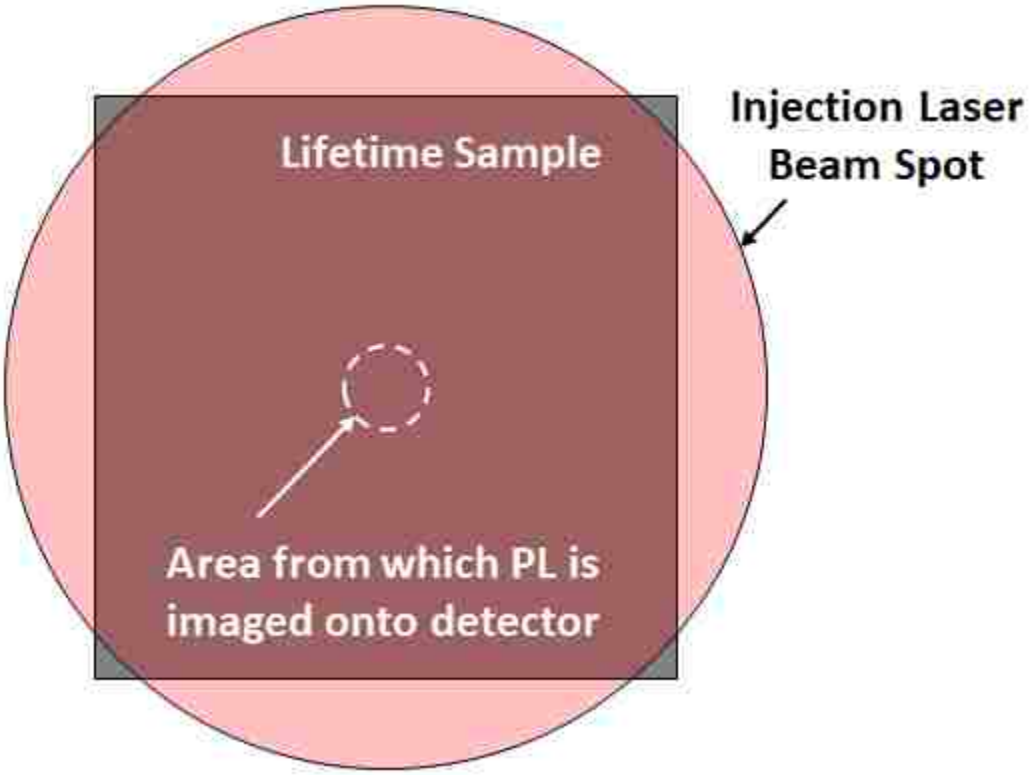

Figure 3.2: Example of PL imaging with laser spot size relative to sample

Two PL detectors were available, for use one at a time, each with a different cutoff wavelength and pre-amplifier bandwidth, depending on the cutoff wavelength of samples under test. For MWIR samples, a λ_c = 6 µm HgCdTe detector with a 300 MHz bandwidth was used, and for LWIR samples, a λ_c = 10.6 µm HgCdTe detector with a 700

MHz bandwidth was used. Both were thermoelectrically cooled in four stages down to 195 K.

To eliminate laser reflections and other undesirable light from reaching the PL detector, a long-pass-filter (LPF) was installed directly in front of the detector which transmitted all wavelengths above 1.6 μm (PL from samples) while completely blocking all wavelengths below 1.6 μm. Recall that the injection laser wavelength was 1.535 μm.

In order to achieve the low-level injection conditions for reasons discussed above, the intensity of the laser pulses had to be significantly attenuated. This was accomplished by putting both neutral density (ND) filters a half-wave plate/polarizing beam splitter combination in the laser path for bulk and fine-tuning attenuation, respectively. ND filters transmit light according to

$$\mathrm{T}_{ND} = P_0 \times 10^{-ND}, \tag{3.4}$$

where T is % transmission, P_0 is the optical power incident on the filter, and *ND* is the neutral density value specified on the filter, typically but not necessarily in integers. For example, an ND filter with value 2.0 will transmit 10^{-2} = 1% of incident light intensity. The transmission of the half-wave plate and polarizer combination may be expressed as

$$\mathrm{T}_{wp} = P_0 \sin(2\theta), \tag{3.5}$$

where θ is the angle of the half-wave plate's orientation with respect to the position in which the subsequent polarizing beam-splitter reflects nearly 100% of incident electric fields. The laser pulse fluence, *F*, can be calculated according to

$$F = \frac{P}{\pi\omega_e^2 R_R}, \tag{3.6}$$

where *P* is the pulse power, ω_e is the 1/e radius of the beam spot, and R_R is the repetition rate of the pulses. This will be scaled down with the attenuators according to Equations

3.4-3.5; therefore; with knowledge of the cryostat window transmission at the laser wavelength (T_W), Fresnel reflection coefficient (R_f), length of absorber region (L) and absorption coefficient of the sample (α), an estimate of the excess carrier density (ΔN) injected into a sample with each laser pulse can be expressed by

$$\Delta N = T_W(1 - R_f)\left(\frac{P}{\pi\omega_e^2 R_R}\right)\left(\frac{\lambda}{hcL}\right)(1 - e^{-\alpha L})\sin(2\theta_{WP})\,(10^{-ND}). \qquad (3.7)$$

A simulation of injected excess carrier density vs. half-wave plate angle, using Equation 3.7, is shown in Figure 3.3 for various ND filter values.

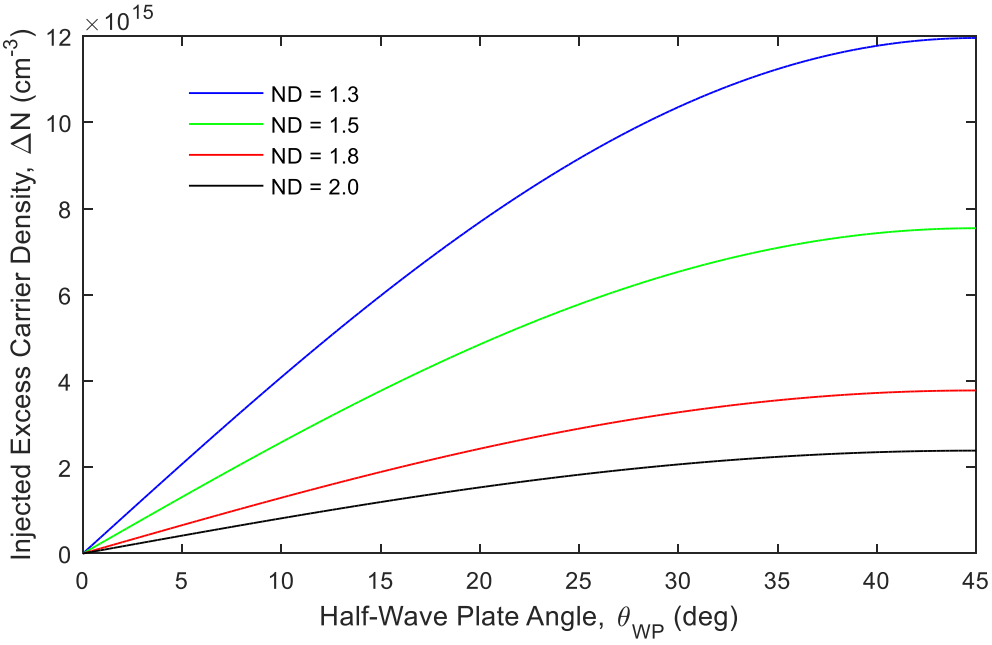

Figure 3.3: Injected excess carrier density vs. laser attenuation

Although this can provide useful information, exact doping concentrations (which would provide a target threshold for ΔN) and absorptions coefficients are rarely known due to the proprietary nature of samples received and/or the inability of either party to measure these parameters. This is not problematic, however, as the best practice is to attenuate the laser as much as possible while still retaining a measurable PL signal. In other words,

absolute knowledge of the excess carrier density being injected is not a prerequisite for extracting minority carrier lifetime from PL transients.

A 12-bit oscilloscope was employed to digitize the signal output from the PL detector vs. time. To reduce noise, an enhanced resolution (ERES) function was applied [**69**], which is similar to smoothing the signal with a simple moving average filter, at the cost of reduced bandwidth which was never reduced further than that of the detector preamplifier being used. The horizontal time base was chosen for each sample such that the end of the transient 'tail' would be captured, that is, when the output from the PL detector returned back to the pre-injection baseline.

Low-level injection requires relatively faint laser pulses. This results in a relatively faint PL emission (signal) from samples which is often very difficult to detect; therefore, summed averaging is utilized over 10's of 1000's of PL transients for a single lifetime measurement. This is performed 'on-board' the oscilloscope after which a single, summed average PL transient is recorded for subsequent analysis. A glass slide in the beam path reflects minimal energy toward a single pixel InGaAs detector which is used to optically trigger the oscilloscope on the laser pulses. A optical schematic of the TRPL system is shown in Figure 3.4.

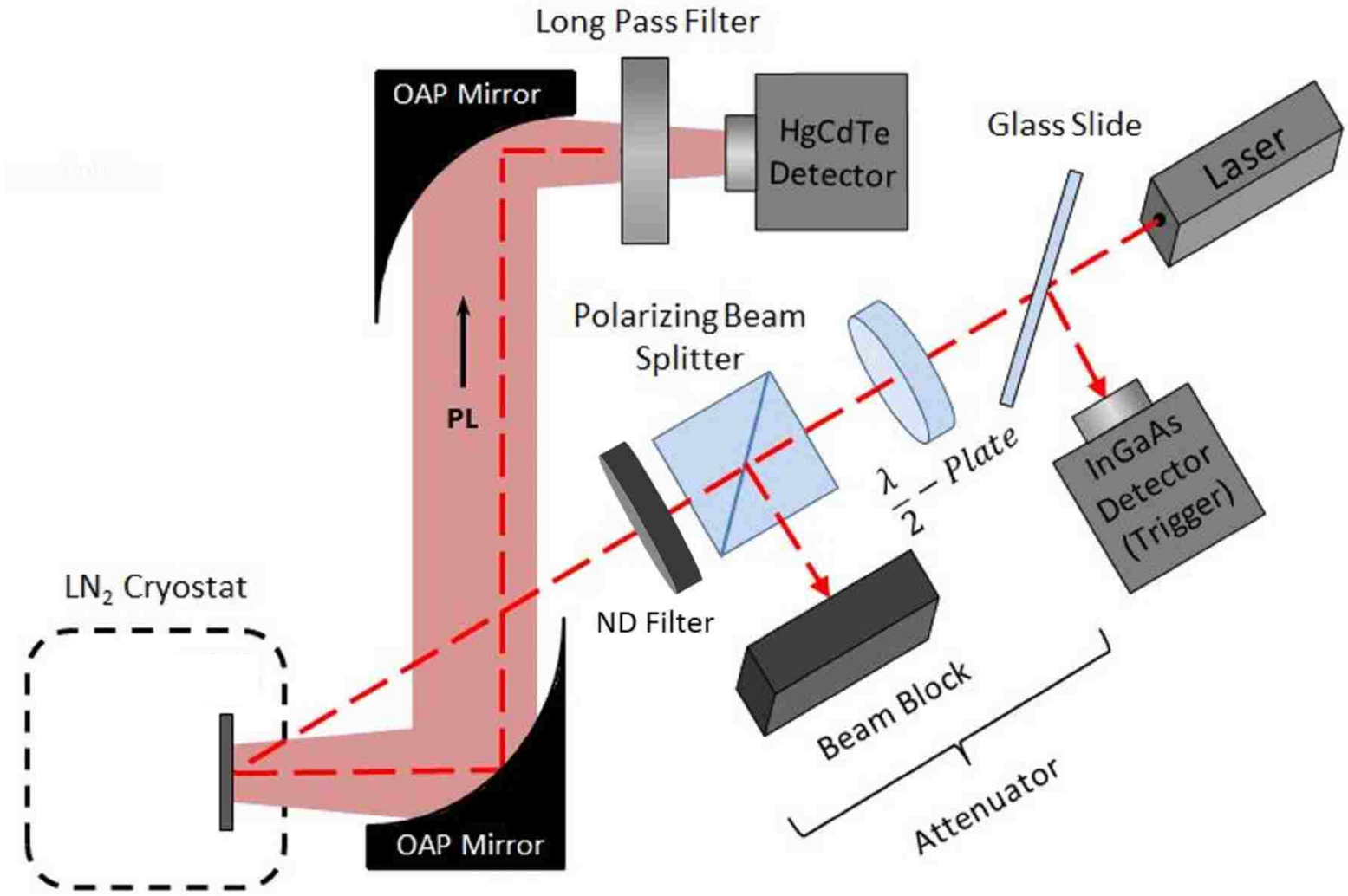

Figure 3.4: Schematic of the TRPL test system

3.3 Lifetime Samples

When evaluating a new prototype detector material system, 'lifetime samples' are often grown for characterization, which are unprocessed semiconductor wafer dies. In such samples, of which many are characterized in this work, a 'cap' is included to mitigate surface recombination. This is a wide bandgap heterojunction which helps retain injected excess carriers in the absorber region to promote higher radiative recombination probability and, therefore, stronger PL emission. For example, the epitaxial structure of a III-V T2SL lifetime sample is provided in Table 3.1.

Table 3.3: Epitaxial structure of a lifetime sample

Layer	Material	Thickness (Å)
Substrate	GaSb:Zn	∞
Buffer	GaSb	800
Barrier	$Al_{1-x}Ga_xSb$	1000
Superlattice Absorber (x200 periods)	GaSb	20
	InSb	1
	InAs	25
	InSb	1
Barrier	$Al_{1-x}Ga_xSb$	1000
Cap	GaSb	100

Lifetime samples were received in a large variety of sizes and shapes; therefore, it was often necessary to manually cleave these wafer dies. It was decided that the optimum size was 5x5 mm in order to fit five samples per cryostat window without risk of having the laser beam overlap onto more than one sample at a time. Cleaving was accomplished by gently scribing a line on a sample against a straight-edge, placing sample over a rounded Q-tip handle centered on the scribe line, and applying pressure on sample edges until it cleaved along the scribed line. This is illustrated in Figure 3.5.

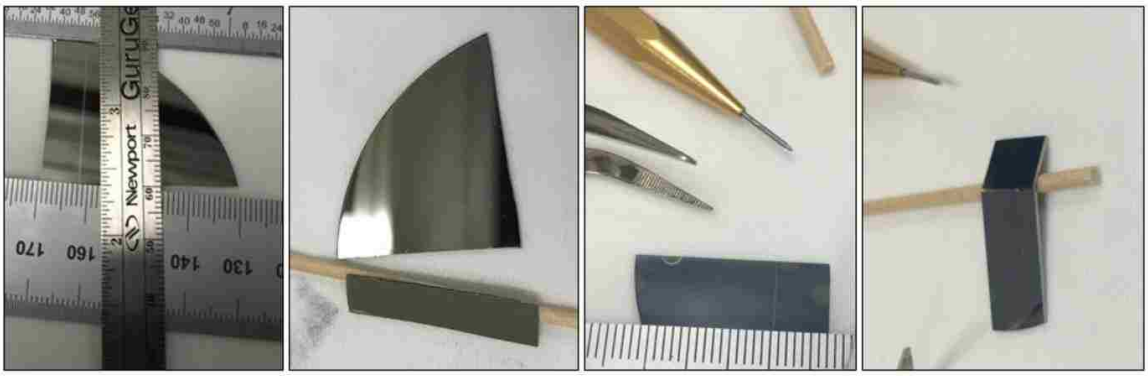

Figure 3.5: scribing (a) and cleaving (b) along first axis, scribing (c) and cleaving (d) along second axis

3.4 Cryostat and Temperature Control

All samples were mounted in an optical cryostat cooled with a continuous flow of liquid nitrogen (LN_2) supplied by gravity from a permanently affixed five liter holding tank. To prevent unnecessarily high flow rates, the gas flow from the exhaust port was throttled down to approximately 5 standard cubic feet per hour (SCFH) with a regulator. This enabled hold times ranging from 12-15 hours with samples maintained at 120K.

A custom sample holder assembly, consisting of a 4-way elbow and mounting discs, was designed and fabricated which both mated to the cryostat's cold finger and allowed samples to be placed as close to the four optical windows as possible, without touching, in order to maximize PL emission toward the collection optics. In addition, a threaded hole was tapped in the bottom of this assembly in which a radiation tolerant temperature sensor (Cernox®) was placed. Samples were affixed to the circular discs using rubber cement or silicone vacuum grease and were designed to be easily removable from the 4-way elbow. The assembly and mounted samples are shown in Figure 3.6.

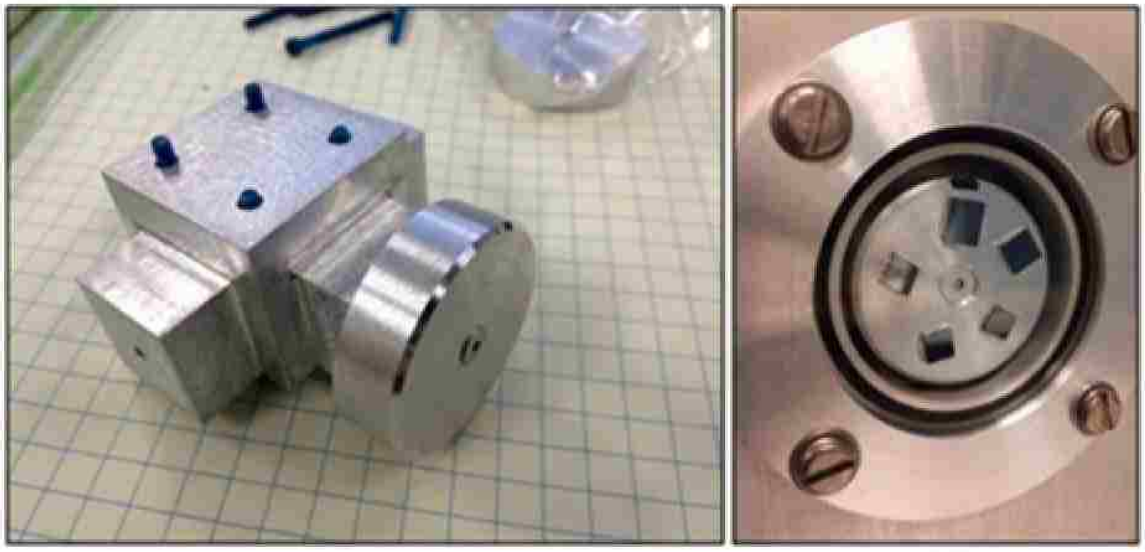

(a) (b)

Figure 3.6: (a) 4-way cold finger elbow, and (b) 5x5 mm samples mounted on disc

This entire assembly, including the screws, was fabricated out of aluminum so they wouldn't become radioactive with proton irradiation as would other metals, such as copper. The propagation depth of 63 MeV protons through aluminum was taken into consideration (using SRIM analysis software [**70**], which stands for *Stopping Range of Ions in Matter*) when determining the thicknesses of the sample holding discs. They are thick enough such that protons with kinetic energies ≤ 63 MeV will not reach samples that may be mounted on the other side of the cryostat facing the opposite window. Assuming all samples are 5x5 mm, as shown in Figure 3.6b, up to 20 samples could be characterized at one time if all four windows are utilized.

To maintain samples at a constant temperature, a variable electrical current was supplied through a resistive heating element on the cold finger, controlled using readings from the temperature sensor near the samples and a proportional-integral-derivative (PID) controller programmed with the calibrated response curve of the Cernox® sensor. Once

PID values were optimized, this enabled sample temperature change and stabilization on the order of time indicated in Figure 3.7. Temperature histories were always logged with a temporal resolution of ≤ 5 seconds such that they could be plotted as shown below.

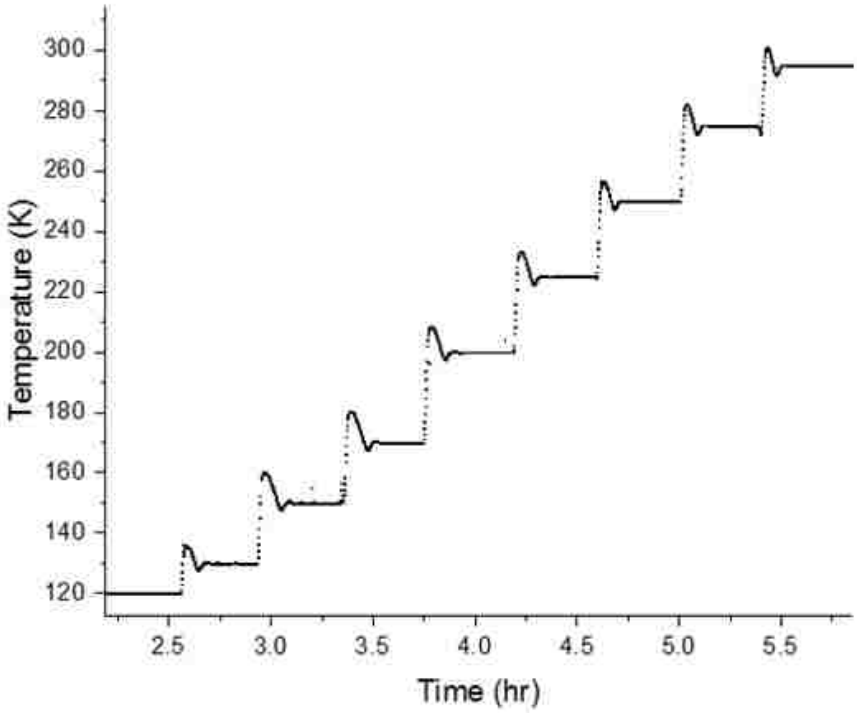

Figure 3.7: Example of sample temperature history

Barium fluoride (BaF_2) windows were installed, each 2 mm thick, to achieve very high optical transmission at both the injection laser and sample cutoff wavelengths while being able to maintain high vacuum within the cryostat. The transmittance for this material is shown in Figure 3.8 [**71**]. Care had to be taken to prevent water contacting these windows, e.g. condensation forming due to relatively poor internal vacuum pressure in combination with cryogenic temperatures, as this would lead to permanent damage in the form of cloudiness and presumably loss of transmission. If this occurred the window would be discarded immediately.

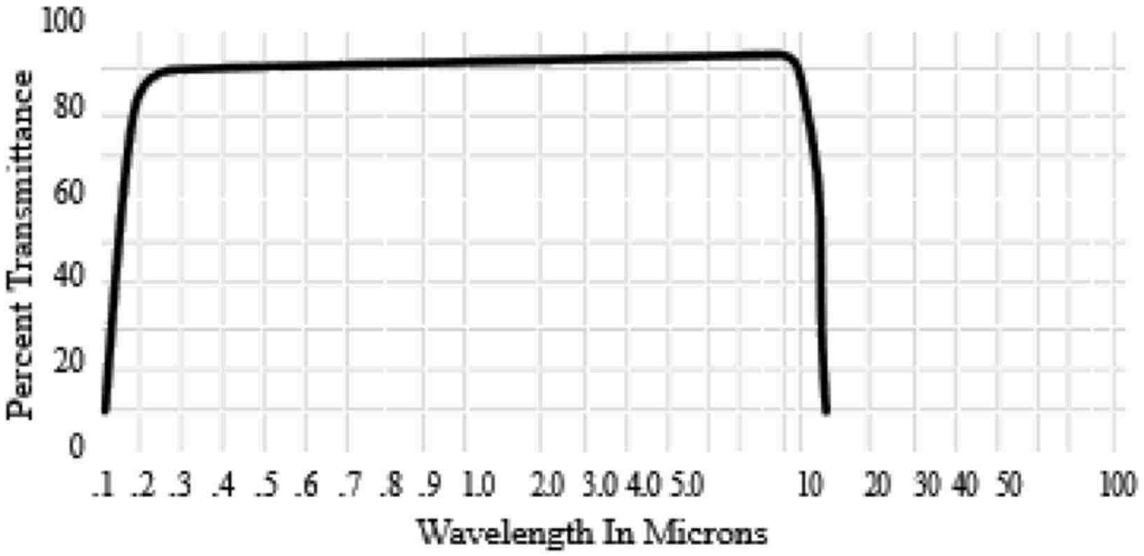

Figure 3.8: Transmission spectrum of the BaF_2 sample windows

During the first proton irradiation experiment with this system, it was noticed via Geiger counter that these BaF_2 windows became slightly radioactive, proportional to dose fluence. Therefore, after the larger doses in the schedule, i.e. adding TID 50 krad to bring the cumulative dose from TID 50 to TID 100 krad, the cryostat assembly was set aside (away from the human populated characterization area) with lead bricks in front of the windows and checked with a Geiger counter approximately every hour until the readings became negligible.

Since these windows were reused for multiple radiation experiments, the transmission spectrum of one of these windows was measured via Fourier-transform infrared spectroscopy (FTIR) before and after being subjected to a cumulative proton fluence of 2.25×10^{12} p/cm^2. This value corresponds to three complete dose schedules outlined in section 3.7. It was found that there was no significant change in transmission (less than 2%). Even if transmission had largely decreased, it would have resulted in a lower PL amplitude and SNR, not necessarily affecting extracted lifetime values.

3.5 Automation

Several functions of the TRPL test system were automated to mitigate human error, increase time efficiency, and enable long duration, overnight, unsupervised tests. To move from one sample to another, the entire cryostat assembly was physically moved by a four-motor system which included custom-designed metal fabrications. Three motors served to move the cryostat (samples) horizontally, vertically, and parallel (focus) with respect to the incident laser beam. The 4th motor rotated the cryostat around its vertical axis in order to move a different, orthogonal, window into the beam path. This allowed the sensitive optics to remain unmoved throughout the duration of an experiment. Figure 3.9 contains physical images of the cryostat and the motor system on which it is mounted.

Figure 3.9: (a) Cryostat/LN_2 feeder assembly; (b) cryostat on motor assembly; (c) cryostat removed, showing how its base plate is rotating on the 4th motor.

The cryostat/LN_2 feeder assembly simply lifts off the motor assembly, so that it can be taken into a radiation chamber for dosing, and is returned to the exact same position due to hemispherical recesses under the plate which mate to the ball bearings visible in Figure 3.8c.

The laser attenuation system was also automated. ND filters of values ranging from 0 to 4 were placed in a motorized, 12-position wheel for bulk attenuation. The half-wave plate was also mounted in a motor which rotated circularly about the propagation axis of the laser beam for fine attenuation.

All automation was controlled by a custom graphical user interface (GUI) developed by the author using the LabVIEW programming environment. This includes all motor movement (sample and attenuation changes), oscilloscope setting changes, temperature control, temperature logging, and data acquisition. See Figure 3.10.

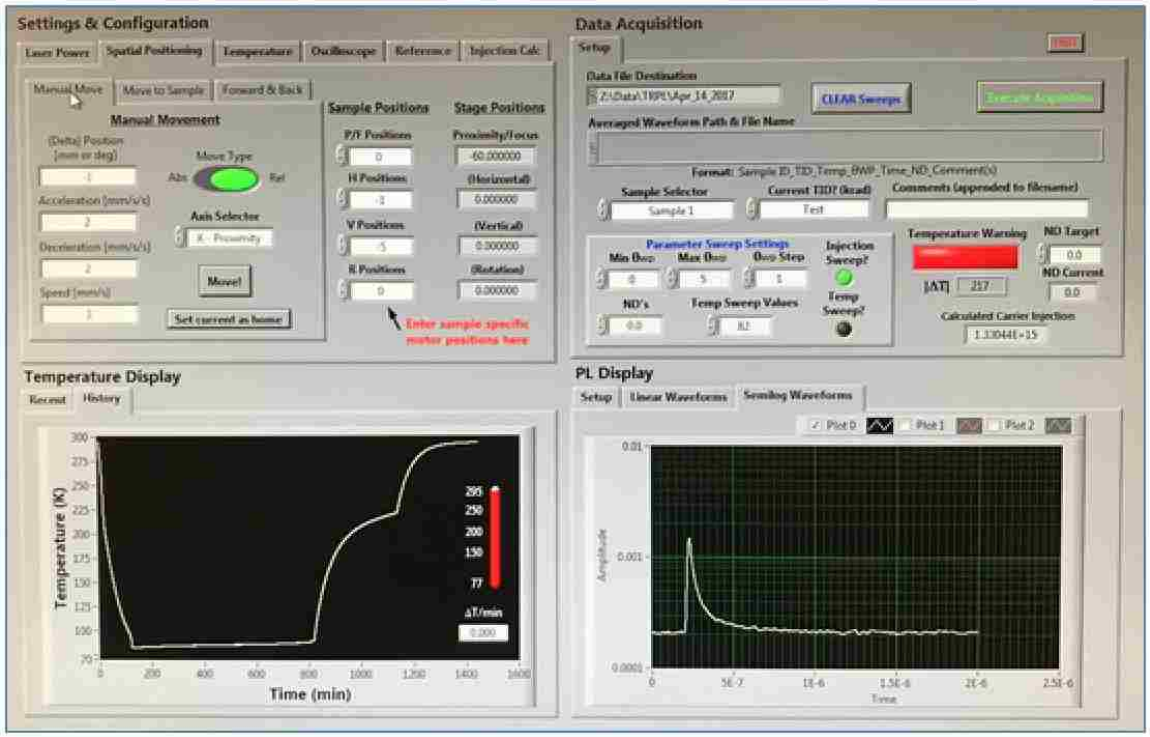

Figure 3.10: Custom GUI for TRPL control and data acquisition.

Several preparations are needed before running an automated data collection routine: optimizations for sample positions, oscilloscope settings, and laser attenuation. Optimal motor positions must be recorded and provided to the software so it knows precisely how to move the cryostat to get the laser beam centered on each sample. This is accomplished roughly at first by tracking the laser beam with an IR viewer card by hand and using manual motor jog command to get the beam onto the sample of interest. For fine tuning and final position optimization, the motors are manually jogged left/right/up/down for several iterations until the PL amplitude on the oscilloscope is maximized. All motor positions are recorded and fed to the software. This is repeated for each sample. Once accomplished, the user may move any sample into the laser beam by selecting it by name from a drop-down menu and clicking a single move button.

Once sample positions are known and recorded, attenuation optimization is performed. Here, the vertical resolution of the oscilloscope is maximized (1 mV per division in this case) and the laser pulse intensity is attenuated as much as possible until the PL signal becomes barely measurable. Then, typically, five injection pulse intensities (sometimes referenced by the fine tuning attenuator position in angle of the half-wave plate, θ_{WP}) above this value are selected for use in characterization. Each sample is assigned its own, different, injection-level settings, i.e. sample #1 may require ND = 2 paired with θ_{WP} = 2, 4, 6, 8, 10 degrees, while sample #2 may require ND = 1.3 and θ_{WP} = 1, 2, 3, 4, 5 degrees. This effort is undertaken due to the aforementioned importance of achieving the low-level injection condition.

Finally, the oscilloscope (PL signal digitizer) settings must be optimized. The vertical resolution is maximized such that the peak of the PL transient is not clipped

while being injected with its highest assigned injection-level. This must be performed at the coldest planned temperature of the characterization due to the fact that the peak amplitude of PL emission is directly proportional to injection-level and inversely proportional to temperature. The horizontal resolution must be configured such that the tail of the PL transient is captured, as this is the most important region for extracting minority carrier lifetime through curve fitting. Next, the ERES function is increased to reduce noise until the reduction in bandwidth is no lower than that of the preamplifier of the detector being used (300 MHz for MWIR, 700 MHz for LWIR). Finally, it is ensured that summed averaging mode is enabled so that a single, final transient may be downloaded after thousands of PL transients have been averaged. Again, this is performed for each sample and the configuration for each is saved on-board the oscilloscope for recall as needed by the TRPL automation GUI.

Once these preparations are complete, the user can simply select a mode of operation, press a single button, and return many hours later with data ready for processing. The available modes of operation are: manual, injection sweep, and temperature sweep. In manual mode, a summed average PL transient is instantly downloaded from the oscilloscope after the user has positioned the sample of interest in the laser beam. With an injection sweep, summed-average PL transients will be downloaded for every sample at every assigned injection-level at the current temperature, with all attenuator and cryostat motor movements automatically handled. With a temperature sweep, injection sweeps are repeated after samples reach each of the user-provided temperature values. The TRPL software will wait to collect data after

temperature changes until certain time delay and temperature check conditions have been met.

3.6 Portability

One of the unique attributes of this TRPL system is that it was designed for the purpose of traveling cross-country to radiation sources. Two optical breadboards were used, each with carrying handles. The optics required alignment only once during re-assembly after travel due to them remaining fixed during characterization. To aid this process, collars were affixed to optical posts before travel when alignment was optimized, eliminating the need to re-adjust heights upon re-assembly. Optical post holders were never removed for travel; therefore, the only optical alignment needed was azimuth adjustment. The packing configurations are shown in Figure 3.11.

Figure 3.11: (a) cryostat assembly, and (b) optical breadboard packed for travel.

As mentioned previously, the cryostat assembly is portable relative to the rest of the TRPL system. This was made possible to allow the cryostat loaded with samples to be transported into the radiation chamber for dosing while the rest of the sensitive equipment remained in an area safe for humans, where post-radiation characterizations took place. A long (~100 ft.) cable was used to continuously maintain stable sample temperatures with the PID controller reading from the temperature sensor and supplying current to the resistive heating element, even while the cryostat assembly was sealed off in the radiation chamber.

3.7 Radiation Experiments

During these deployments, up to twelve unique detector structures, or lifetime samples, in the form of wafer dies (pre-processing) were held at 120 K while minority carrier lifetimes were optically probed before and after step-wise proton irradiation, typically at a kinetic energy of 63 MeV reaching total ionizing doses (TID) of 0, 5, 10, 20, 50, 100 krad [Si]. Hereon, unless otherwise noted, 1 TID is equivalent to a proton fluence (Φ_p) of 7.5×10^9 (p/cm^2). In addition to characterizing minority carrier lifetime as a function of proton fluence, it is also characterized as a function of temperature before and after proton irradiation, including subsequent thermal anneals. Information that can be extracted from these tests include minority carrier lifetime damage factors, recombination mechanism dominance vs. temperature, trap energy level changes, and lifetime recovery phenomena via post-radiation thermal annealing. The typical radiation test protocol for characterizing the change in minority carrier lifetime as a function of proton fluence is shown in Figure 3.12.

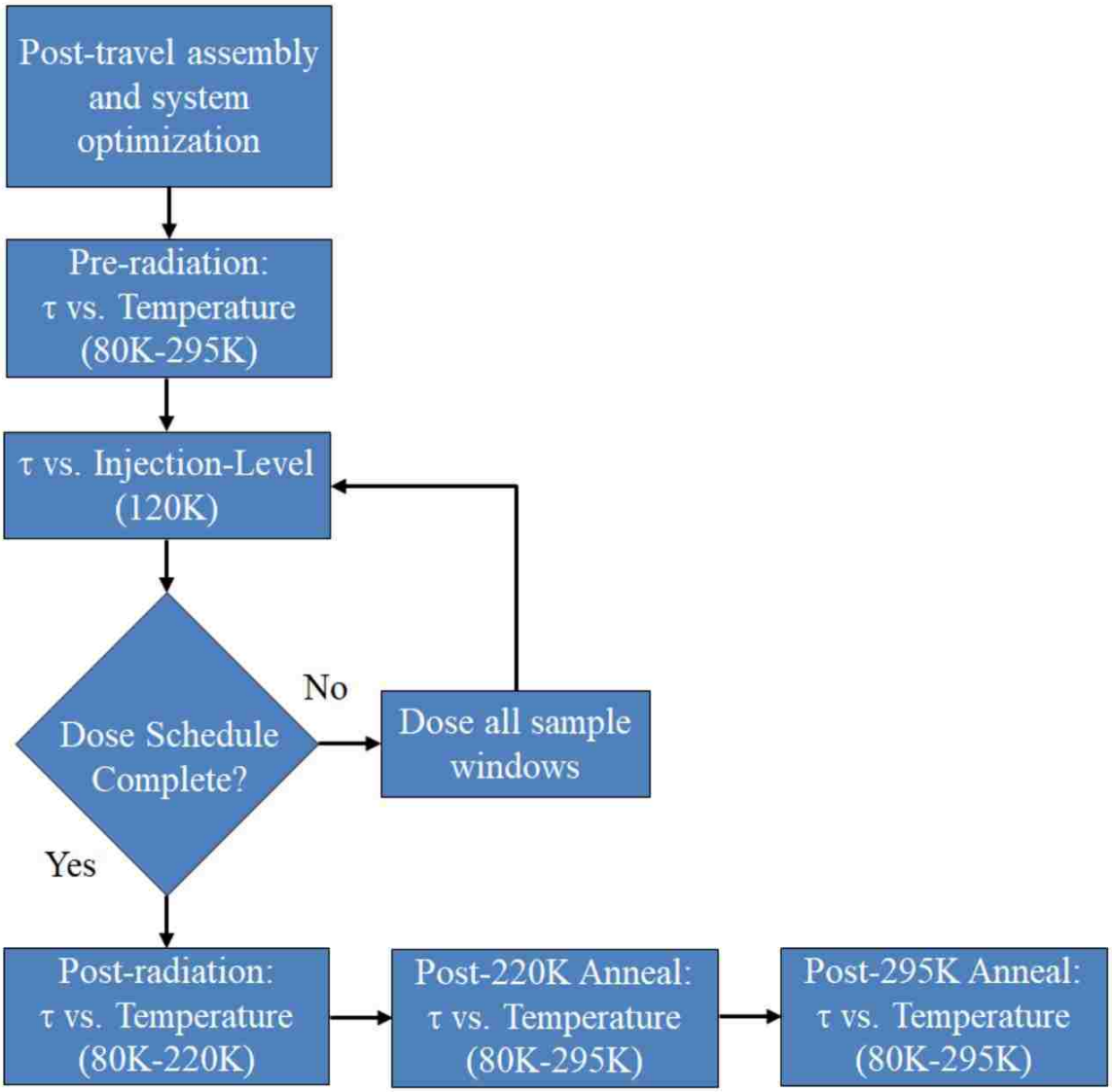

Figure 3.12: Typical radiation test protocol for minority carrier lifetime vs. proton fluence

These were multi-day experiments as each of the four temperature sweeps could take up to twelve hours to complete, and depending on various circumstances, there could be long wait times between proton dosing opportunities.

A custom designed 'alignment plate' was fabricated which mated to both a sample window on the cryostat and the aperture head at the end of the proton beam line. This served two purposes: (1) it forced perfect alignment of the samples within the proton

beam, and (2) its thickness prevented protons from traveling through undesired regions of the cryostat. This was critical for both accuracy and safety, as the cryostat's cold finger, just above the sample windows, was made out of copper and could have become radioactive if exposed. The alignment plate is shown in Figure 3.13.

Figure 3.13: Alignment plate used to mate cryostat to proton beam.

Another unique attribute of this TRPL system is that it maintains samples at 120K for the duration of all radiation testing. This is to prevent the 'healing' of radiation-induced damage, which is a function of temperature, between radiation exposure and lifetime characterization. Vacancies and interstitials, created through displacement damage, have a certain mobility dependent on temperature; therefore, it is possible for at least some of these pairs to recombine, or 'anneal out' at higher temperatures. Data will be presented on this phenomenon in a later chapter. Figure 3.14 shows a complete temperature log for an actual radiation experiment. In this example, the 220K anneal shown in the test protocol in Figure 3.12 was skipped.

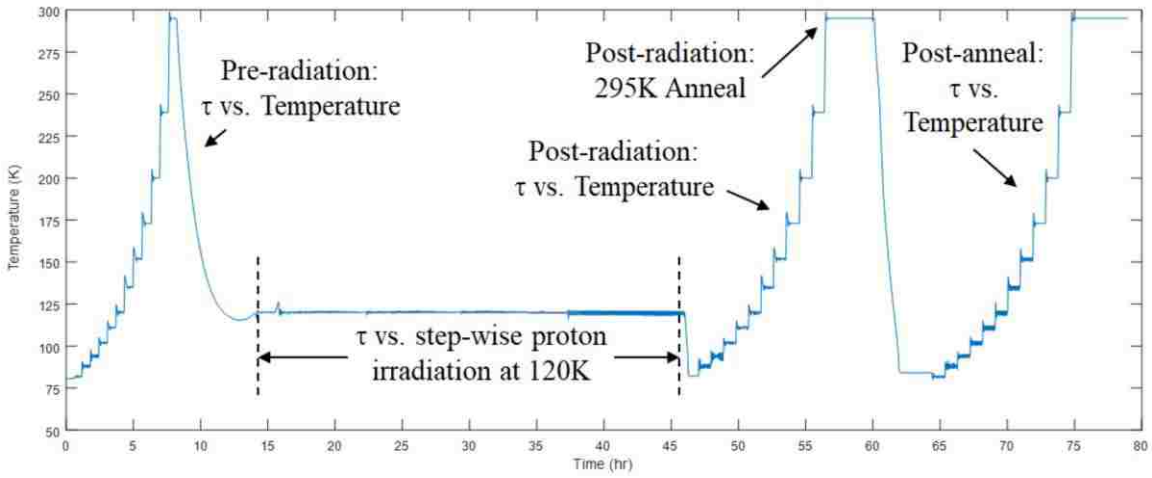

Figure 3.14: Complete temperature log from an actual radiation experiment.

The most important takeaway from these experiments was the rate of minority carrier lifetime (low-level parameter of ultimate device performance) degradation as a function of proton fluence. Under proton irradiation, the defect concentration N_T is, typically, linearly proportional to the time-integrated proton flux or proton fluence Φ_P incident on the material, as given by

$$N_T(\Phi_P) = N_T(0) + \left(\frac{dN_T}{d\Phi_P}\right)\Phi_P, \quad (3.8)$$

where irradiation is being assumed to generate a single type of defect with pre-rad concentration $N_T(0)$ and an introduction rate $(\mathrm{dN}_T/d\Phi_P)$ due to proton irradiation, which is a function of the proton energy and assumed to be constant. As N_T increases, τ will eventually become limited by Shockley-Read-Hall (SRH)-recombination, if not so already, and related to $N_T(\Phi_P)$ according to

$$\frac{1}{\tau(\Phi_P)} = \sigma v_{th} N_T(\Phi_P), \quad (3.9)$$

where σ is the minority carrier capture cross-section for this defect, $v_{th} = \sqrt{3k_BT/m_h}$ is the thermal velocity, k_B is Boltzmann's constant, T is the temperature and m_h is the hole

mass, assuming the irradiated material is n-type. Replacing $N_T(\Phi_P)$ in Eq. 3.8 with Eq. 3.9 leads to

$$\frac{1}{\tau(\Phi_P)} = \frac{1}{\tau(0)} + K_{\tau^{-1}}\Phi_P, \quad (3.10)$$

where $K_{\tau^{-1}} = \sigma v_{th}(\mathrm{dN}_T/d\Phi_P)$ is the lifetime damage factor and $\tau(0)$ is the initial SRH lifetime. Equation 3.10 indicates that a plot of the recombination rate $\tau(\Phi_P)^{-1}$ should be linear with increasing Φ_P which makes for an easily recognizable behavior in the measurement datasets with which to validate this theory and determine values for $\tau(0)$ and $K_{\tau^{-1}}$ using a simple linear fitting routine.

To avoid confusion, it is worth noting that what is referred to herein as the 'lifetime damage factor' is actually the *inverse* lifetime (recombination rate) damage factor as denoted by the subscripts in $K_{\tau^{-1}}$ due to this parameter being a linear function of proton fluence. This will be shown to be true with experimental data. Also, since damage factors are dependent upon the kinetic energy of the impinging protons, all damage factors herein are reported for 63 MeV protons unless otherwise noted.

3.8 Radiation Source

All radiation experiments performed in this work took place at the Crocker Nuclear Laboratory located at the University of California in Davis. The proton source is a 76 inch isochronous cyclotron capable of providing stable, uniform beams with a tunable kinetic energy range from 4 to 68 MeV [**72**]. Sensors were in place for real-time beam monitoring and statistics tracking. These data were used to plot minority carrier lifetimes vs. measured proton fluence as opposed to target proton fluence.

3.9 Summary

Minority carrier lifetime is extracted by curve fitting the photoluminescence decay transients that are generated by injecting excess carriers into the samples via laser pulses. This technique is called time-resolved photoluminescence (TRPL) and is well documented in literature [**73**], [**74**]. A schematic of the experimental setup used in this study was provided in Figure 3.4. Briefly, a ~ 3.34 ns laser pulse from a 1.535 μm passively Q-switched laser is directed towards the sample held in a liquid nitrogen continuous-flow cryostat set to 120 K. The laser pulse is attenuated significantly to lower the pulse power level to achieve the low-level injection condition. The resulting excitation of an excess electron-hole carrier density Δn in the samples leads to photoluminescence as the excess carrier density returns to its quiescent state $\Delta n = 0$. A pair of off-axis parabolic (OAP) mirrors is used to collect the light and direct it toward a single-pixel HgCdTe detector with a 6.0 μm or 10.6 μm cutoff wavelength connected to an oscilloscope to digitize the resulting optical PL transient.

Solving the continuity equation for Δn following a laser injection pulse that initially generates $\Delta n = \Delta n_0$ by applying the low injection condition (i.e. p-type: $\Delta n \ll N_A$) leads to $\Delta n(t) = \Delta n_0 e^{-t/\tau}$. In practice this means once the $PL(t)$ falls below a certain threshold value it should decay as a single exponential. An example of actual PL transients from a MWIR *nBn* detector structure which reflect this single-exponential behavior are shown in Fig. 3.15. After an initial rapid decay, attributable to surface recombination, only a single exponential-dependence remains, forming the long-tail region which appears linear on a semi-logarithmic plot. The tails of these transients are

fitted to obtain τ at each new TID level, and then τ^{-1} is plotted vs Φ_p. The slope of this relationship is the rate of change of the minority carrier recombination rate as a function of proton fluence and is called the lifetime damage factor, $K_{\tau^{-1}}$, which is the radiation hardness metric used herein to compare performance between samples.

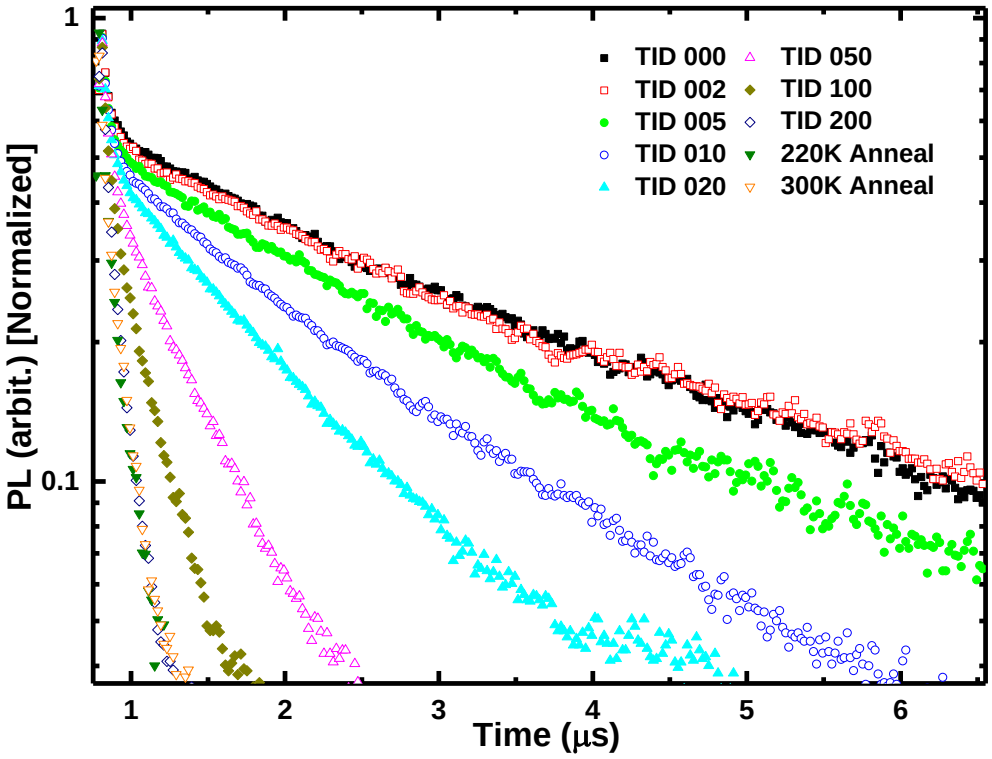

Figure 3.15: Example of normalized TRPL transients from an III-V *nBn* sample changing as a function of step-wise irradiation with 63 MeV protons up to the listed TID levels. Exponential fitting on the semi-log plot is applied in the long-tail linear region to determine τ.

Chapter 4

Minority Carrier Lifetime Studies

4.1 Introduction

In this chapter, each experiment that yielded information beneficial to the IR detector community will be discussed with empirical evidence. It will be shown that there exist significant differences in lifetime damage factors and thermal annealing phenomena between III-V and II-VI detector technologies, which is arguably the most important result from this work. A time dependence on III-V annealing is also validated through a multi-week study. A NIEL study was performed on four differently doped, InAs/InAsSb T2SL *nBn* samples in which lifetime damage factors were extracted for protons of different kinetic energies. This enables the extrapolation of these damage factors for a continuous range of proton kinetic energies which will help spacecraft mission planners estimate higher level detector parameters such as dark current and quantum efficiency based on orbit and mission duration. The effect of doping concentration on lifetime damage factors was also studied.

Not all studies performed in this work were performed as a function of proton irradiation. This characterization system was also employed to perform a variety of parameter studies in which lifetime vs. temperature was characterized as a function of a parameter of interest. For example, optimal MBE growth conditions were determined for an IR detector research group by characterizing minority carrier lifetime vs. temperature

for multiple identical samples that were grown at different temperatures. Lifetime characterizations were also performed for III-V p-type prototype designs as well as III-V designs incorporating Bismuth surfactants, the latter of which has become a new R&D effort due to its ability to introduce large bandgap energy changes with relatively small doping concentrations. III-V *nBn* structures with doping gradients in the absorber were also characterized, in which the gradient creates a built-in electric field intended to aid photo-generated, minority carrier holes reach the contact for collection via drift transport. Finally, lifetime was characterized for different III-V absorber types as well as pre- and post-hydrogenation, the latter of which had an intent of filling natural III-V structure SRH traps with hydrogen ions.

It should be understood that none of the samples characterized in this work were grown by the author, but rather sourced from many different research groups, including large corporations, small businesses, and universities. Due to the proprietary nature of competitive business, as is present in every industry, exact sample designs were not always provided, i.e. doping concentration, superlattice design, thicknesses, etc. Regardless, the data resulting from these characterizations provides an eye-opening snapshot of the relative performance between these two competing IR detector material technologies.

Sample sets #1-5 should be considered part of the same experiment, which was an effort to characterize a large variety of samples sourced from different research groups. Experiment results, data analyses, and trends will be presented here; however, fundamental physics-based explanations will be sought in the following chapter.

4.2 Lifetime vs. Proton Irradiation

Various proton irradiation experiments will be shown in this section, for both II-VI and III-V detector samples. Data will be introduced incrementally, as different sample sets were characterized under slightly different test conditions, e.g. different long-pass filters or detector cutoff wavelengths. For each set, the test conditions will be specified along with tabulated sample information.

Lifetime damage factors and annealing phenomena between the competing material systems will be presented first, followed by several lifetime vs. temperature studies in which the effect of various design or growth parameters were examined. Aggregate conclusions will be discussed in the following chapters. All information known about each sample is provided; therefore, if certain parameters (e.g. absorber thickness, elemental mole ratios, doping concentration, superlattice architecture, etc.) are excluded, it should be assumed that this information is proprietary and unable to be shared here.

4.2.1 Lifetime Damage Factors: III-V vs. II-VI

These characterizations took place over multiple radiation experiments spanning a multi-year time period in effort to aggregate data on samples from multiple sources and varying parameters such as doping level, cutoff wavelength, MBE growth conditions, and architecture. All III-V samples in this section are composed of the ‘Ga-free’ 6.1 Å group, namely InAs/InAsSb, and held at 120 K. The details of sample set #1 and additional test parameters are outlined in Tables 4.1 and 4.2, respectively.

Table 4.1: Details of sample set #1

Sample	λ_c (µm)	Composition	Cumulative Dose Schedule (TID)*
A_1	4.2	III-V T2SL nBn | Doping = NID	0 | 2 | 5 | 10 | 20 | 35 | 50 | 100
A_2	4.2	III-V T2SL nBn | Doping = 1 x 10^{16}cm^{-3}	0 | 2 | 5 | 10 | 20 | 35 | 50 | 100
B_1	5.2	III-V T2SL nBn | Doping = 4 x 10^{15}cm^{-3}	0 | 2 | 5 | 10 | 20 | 35 | 50 | 100
B_2	5.2	III-V T2SL nBn | Doping = 8 x 10^{15}cm^{-3}	0 | 2 | 5 | 10 | 20 | 35 | 50 | 100
C_1	4.8	III-V T2SL nBn | 3um Absorber	0 | 2 | 5 | 10 | 20 | 35 | 50 | 100
C_2	4.8	III-V T2SL nBn | 3um Absorber	0 | 2 | 5 | 10 | 20 | 35 | 50 | 100

*1 TID = 7.5 x 10^9 p/cm^2

Table 4.2: Test configuration #1

Detector λ_c (µm)	Pre-amp BW (MHz)	Window	Proton Energy (MeV)	LPF (µm)
10.6	700	BaF_2 (2 mm)	63	3.6

Samples A and B are from the same vendor with a differently doped variant of the same design for each of the two cutoff wavelengths, while the C samples were sourced from a different vendor. An example of raw data, which is representative of those from all samples, collected from the TRPL system is shown in Figure 4.1 for sample A_2.

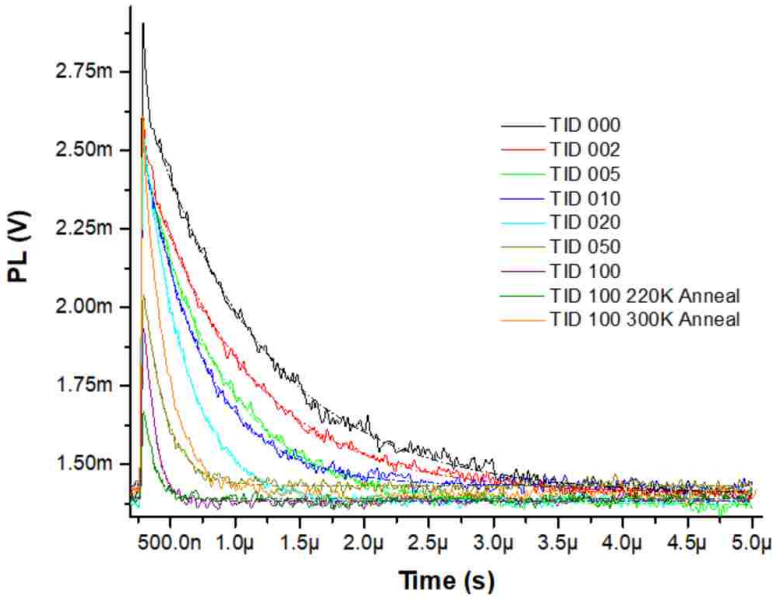

Figure 4.1: Example of TRPL transients vs. cumulative proton fluence from sample A_2. Both PL magnitude and transient times exhibit obvious decreases with increasing proton fluence.

What is shown here is a superposition of all summed average PL transients collected after each proton irradiation dose in the schedule following the test protocol outlined in the previous chapter. It is obvious from this plot that the duration of these PL transients is significantly decreasing with increasing proton irradiation, as expected, attributed to an increase in the SRH trap concentration (N_T) via displacement damage. These transients were fitted to a single exponential function, as discussed previously, to extract the minority carrier lifetime at each cumulative dose level, $\tau(\Phi_p)$. Then, the lifetime damage factor is found through a linear fit of τ^{-1} vs. Φ_p as shown in Figure 4.2.

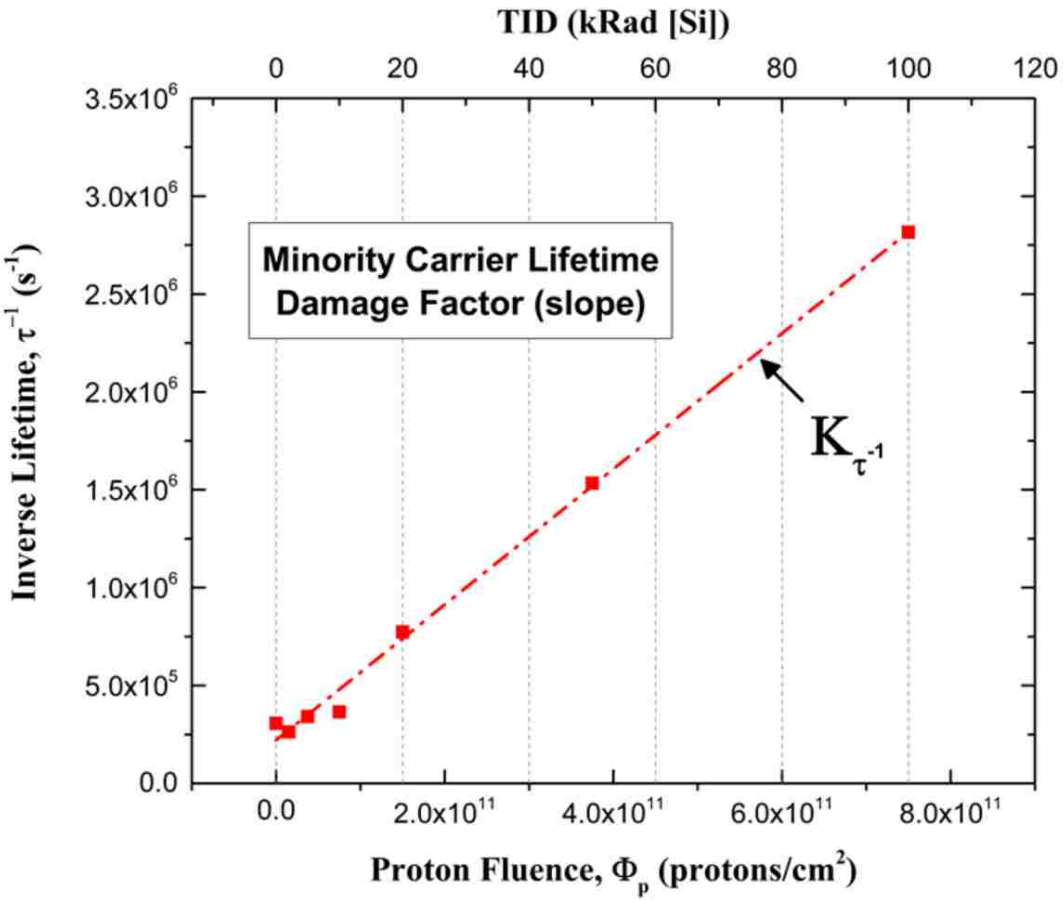

Figure 4.2: Example of lifetime damage factor extraction from τ^{-1} vs. Φ_p

Another phenomenon that is obvious from Figure 4.1 is that the peak amplitude of the PL significantly decreases along with the transient duration. This is one of the reasons that

performing these characterizations at multiple different injection levels is important. As PL amplitude directly correlates with injection level, a highly attenuated laser pulse which produces a nice low-level injection transient before irradiation may produce an unmeasurably weak PL emission at high cumulative proton fluences. The data presented in Figure 4.1 is from one of the multiple injection levels at which characterizations were performed. For final analyses, the data from the lowest injection level which produced a reasonable curve fit after the final dose was selected.

Some additional observations can be made with the post-annealing transients. After the final proton dose characterization, the samples were characterized again at specific temperatures while being warmed up to 220 K (post-rad temperature sweep), then re-characterized at 120 K. Then this was repeated again but up to 300 K. The anneal transients in Figure 4.1 are from the 120 K characterizations after reaching the specified anneal temperature. In this example, it is noticeable that the lifetime slightly decreased after the 220 K anneal, however significantly increased (as did the peak amplitude) after the 300 K anneal. This 'reverse annealing' phenomenon has been observed by others as well [**75**]. Annealing effects on lifetime degradation will be discussed more thoroughly in the next section.

The example analyses shown in Figures 4.1 and 4.2 were repeated for all samples and the results are superimposed for each subset in Figures 4.3-4.5 for easy visual comparison. The larger the slope, the greater the lifetime damage factor is. Also, since it is τ^{-1} that is plotted on the vertical axis, greater vertical magnitudes equate to lower minority carrier lifetimes. These plots can be used to compare quality between samples

by comparing the absolute minority carrier lifetimes as well as its degradation rate as a function of proton fluence.

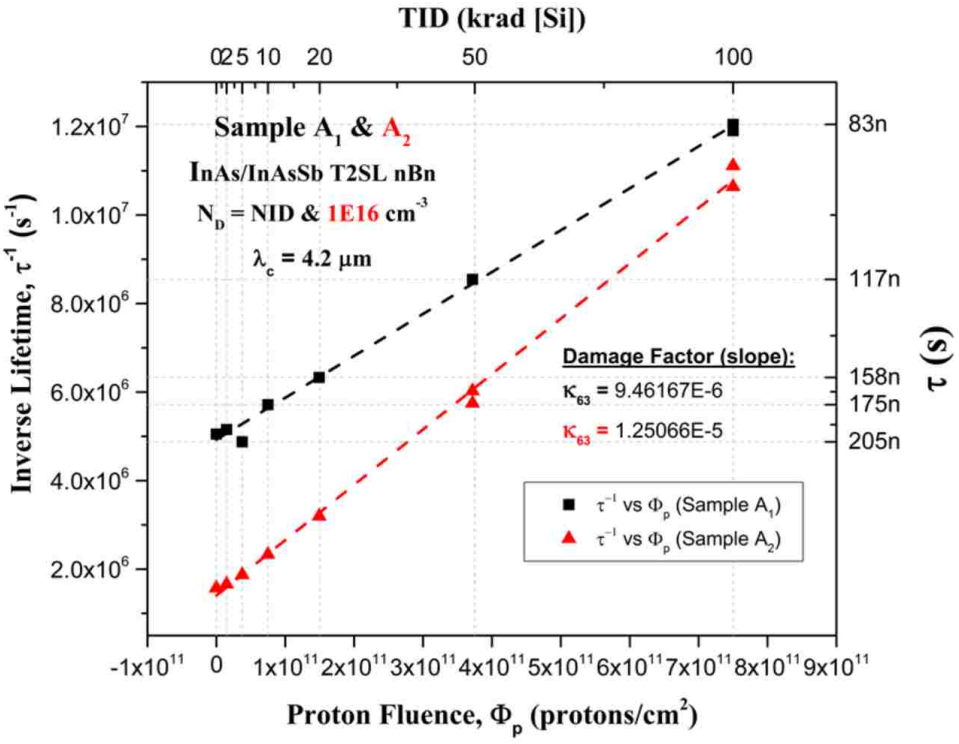

Figure 4.3: Lifetime damage factor extraction for samples A_1-A_2

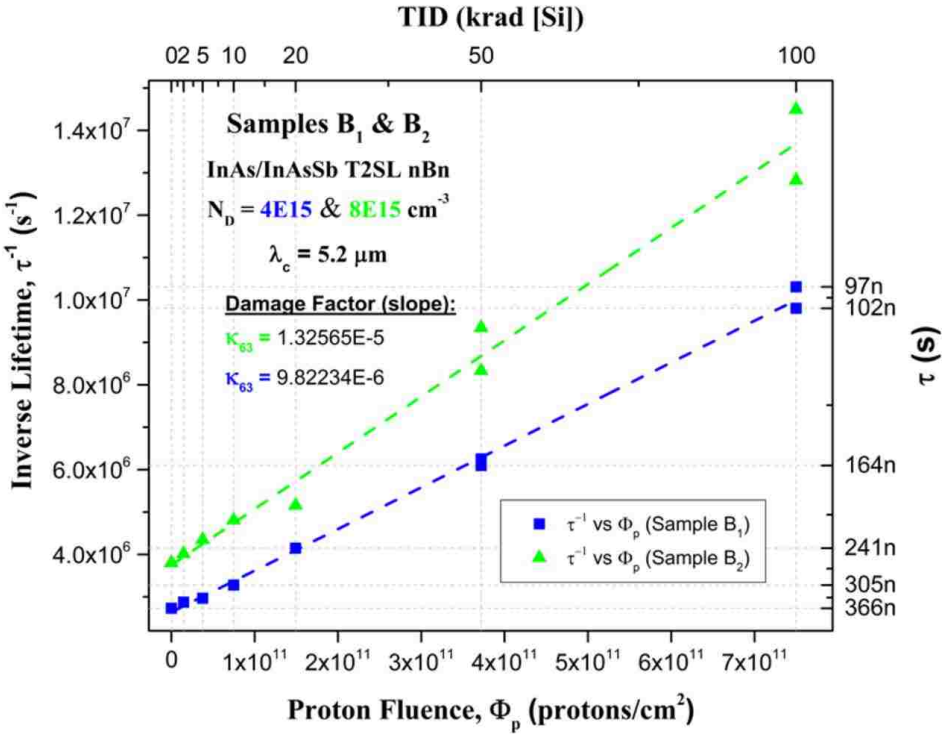

Figure 4.4: Lifetime damage factor extraction for samples B_1-B_2

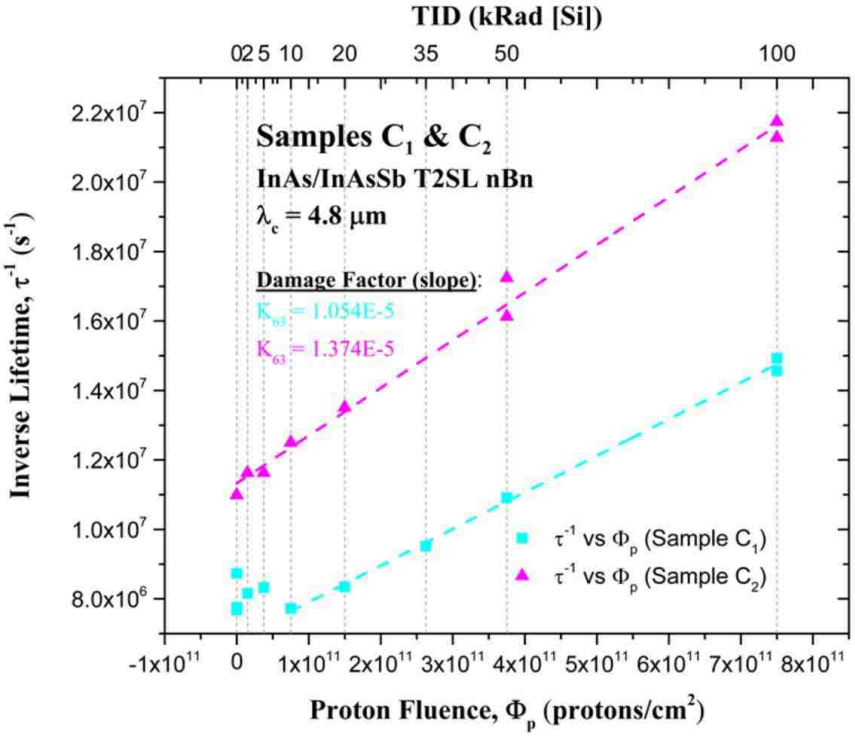

Figure 4.5: Lifetime damage factor extraction for samples C_1-C_2

Some interesting takeaways from these results are that samples with the lower doping concentrations have consistently smaller (better) lifetime damage factors, and the damage factors are very similar over cutoff wavelengths ranging from 4.2 to 5.2 μm, even though the C samples were grown from a different R&D group than the A and B samples.

Sample set #2 included both HgCdTe and InAs/InAsSb T2SL *nBn* structures, representing both the III-V and II-VI elemental groups. Details are outlined in Table 4.3.

Table 4.3: Details of sample set #2

Sample	λ_c (μm)	Composition	Cumulative Dose Schedule (TID)*
D_1	5.0	II-VI HgCdTe	0 | 2 | 5 | 10 | 20 | 50 | 100 | 200
D_2	5.0	II-VI HgCdTe	0 | 2 | 5 | 10 | 20 | 50 | 100 | 200
D_3	5.0	II-VI HgCdTe	0 | 2 | 5 | 10 | 20 | 50 | 100 | 200
E_1	5.4	III-V T2SL nBn	0 | 2 | 5 | 10 | 20 | 50 | 100 | 200
E_2	5.4	III-V T2SL nBn	0 | 2 | 5 | 10 | 20 | 50 | 100 | 200
E_3	5.4	III-V T2SL nBn	0 | 2 | 5 | 10 | 20 | 50 | 100 | 200

*1 TID = 7.5×10^9 p/cm^2

These characterizations were performed with the same test configuration detailed in Table 4.2; however, the proton irradiation dose scheduled was extended to an unusually high 200 krad [Si]. The same analyses shown above were performed, and the superimposed results are shown in Figures 4.6-4.7.

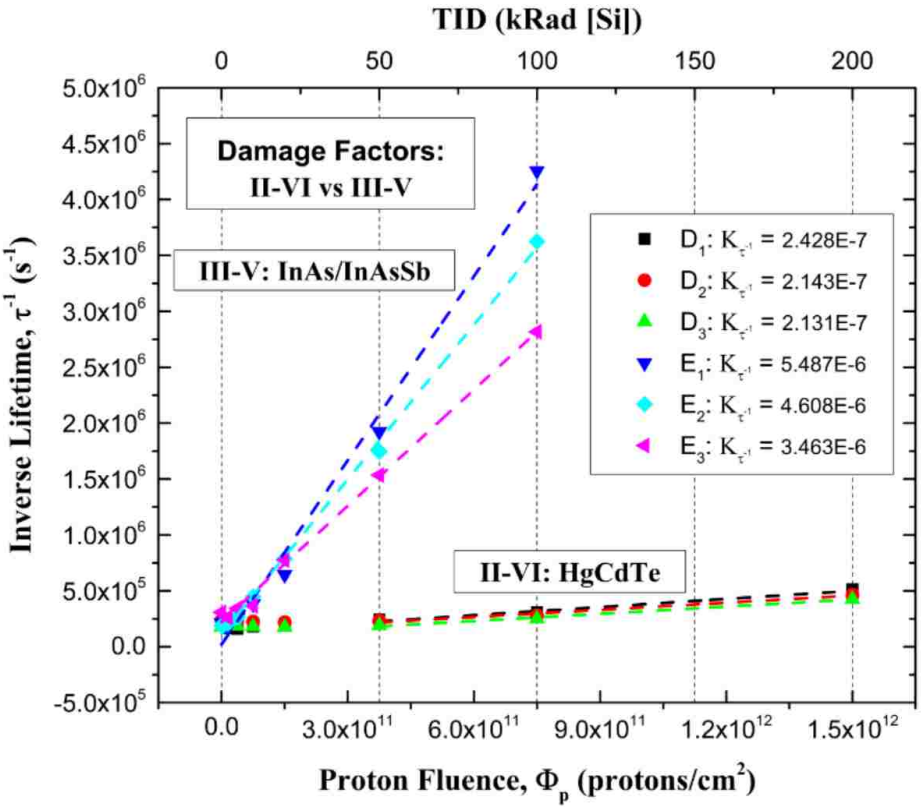

Figure 4.6: Lifetime damage factor extraction for sample set #2.

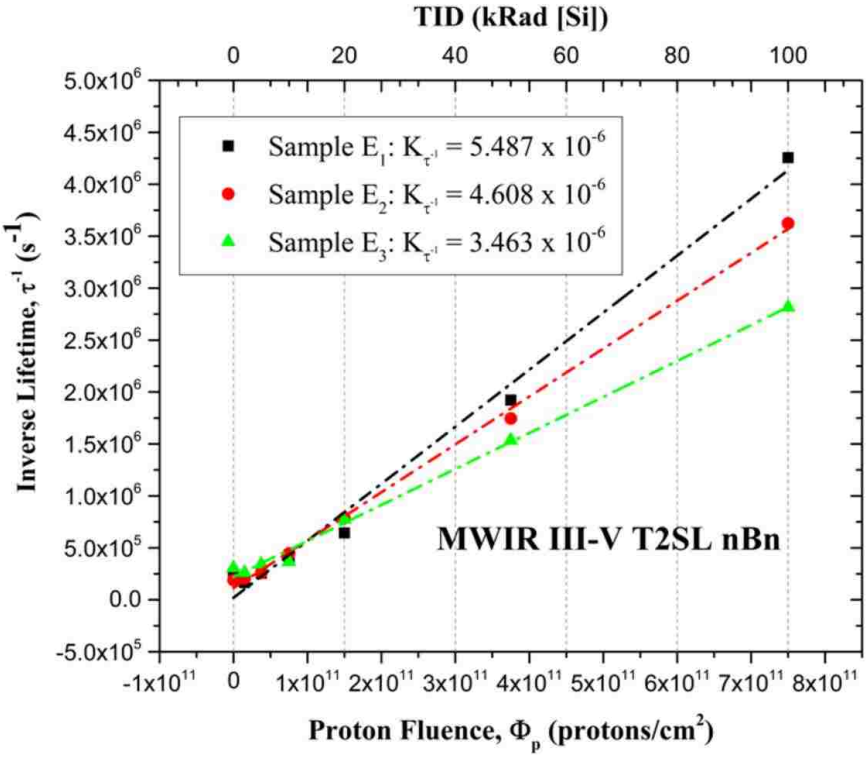

Figure 4.7: Lifetime damage factor extraction for samples E_1-E_3.

On the same scale as the III-V results, the II-VI curve appears nearly flat. This indicates a much lower recombination rate change in HgCdTe with proton fluence resulting in a lower (superior) minority carrier lifetime damage factor. An interesting observation can be made when the HgCdTe results are plotted separately, as is shown in Figure 4.8.

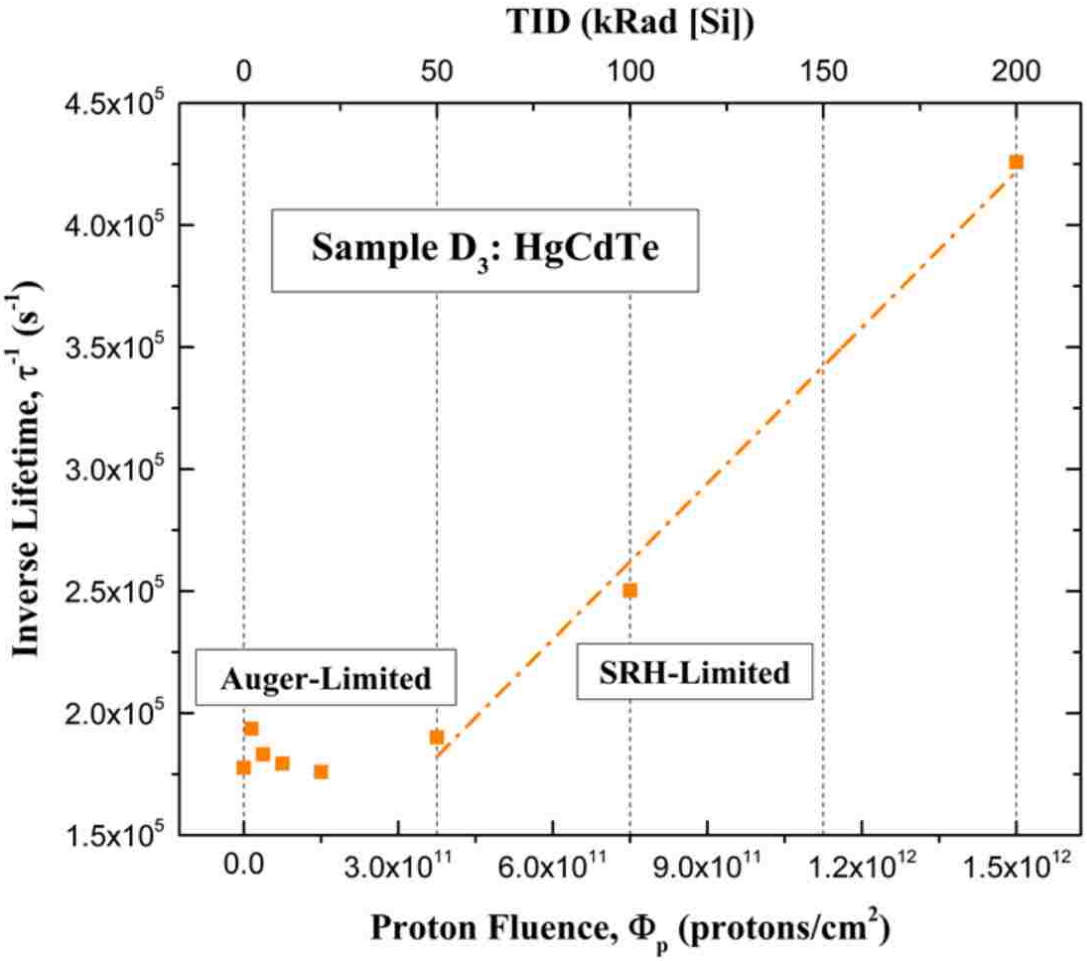

Figure 4.8: Lifetime damage factor and SRH dominance threshold for HgCdTe.

Here, there exists an obvious minority carrier lifetime degradation with proton fluence not easily visible in Figure 4.6; however, the lifetime degradation doesn't begin until a dose level of approximately TID 50 krad [Si]. This is hypothesized to be the minority carrier lifetime in HgCdTe remaining limited by Auger recombination until the proton-

induced displacement damage generates a trap density (N_T) large enough such that SRH recombination becomes the limiting mechanism. After noticing this, the dose schedule was increased to 200 krad [Si] in order to perform a linear fit with more than two data points.

This experiment yielded some critical findings. First, the increase in minority carrier lifetime recombination rates vs. proton fluence was shown to be linear for both material systems and is consistent with results from the previous experiment where samples were sourced from different research groups. Second, the lifetime damage factors in HgCdTe were shown to be significantly (> 10x) smaller than those in the III-V T2SL *nBn* structures. Third, it was shown that all the way up to 200 krad [Si], no samples from either of the competing technologies exhibited a saturation in recombination rate and the recombination rate relationship with proton fluence remained linear. Fourth, an SRH dominance threshold was found in HgCdTe, indicating that the popular single dose 'bag tests' found in literature should only be used to extract lifetime damage factors if the sample's minority carrier lifetime is SRH-limited to begin with. For example, if the damage factor analysis was performed on the HgCdTe sample shown in Figure 4.5 from TID 0 – 100 krad [Si], as is done for 'bag tests', it would yield an underestimated damage factor as that slope would be less than that taken here from TID 50 – 200 krad [Si].

The experimental setup was changed for the next and remaining radiation experiments, as outlined in Table 4.4. A 6.0 μm cutoff wavelength detector was employed with a pre-amplifier bandwidth of 300 MHz for its higher sensitivity in the MWIR. Additionally, the long-pass filter was reduced from 3.6 um to 1.6 um widening

the detectable range of PL emissions yet still blocking any reflections that may have been present from the laser.

Table 4.4: Test configuration #2

Detector λ_c (µm)	Pre-amp BW (MHz)	Window	Proton Energy (MeV)	LPF (µm)
6.0	300	BaF_2 (2 mm)	63	1.6

Experiment #3 was a radiation study on variations of a III-V T2SL *nBn* detector grown with a doping gradient in the absorber (example shown in Figure 2.10) which creates a built-in electric field meant to aid, via drift, the photo-generated minority carrier holes to the contact for collection. Details for this sample set and dose schedule are shown in Table 4.5.

Table 4.5: Details of sample set #3

Sample	λ_c (µm)	Composition	Cumulative Dose Schedule (TID)*
F_1	MWIR	III-V T2SL nBn | Graded Absorber	0 | 2 | 5 | 10 | 20 | 50 | 100
F_2	MWIR	III-V T2SL nBn | Graded Absorber	0 | 2 | 5 | 10 | 20 | 50 | 100
F_3	MWIR	III-V T2SL nBn | Graded Absorber	0 | 2 | 5 | 10 | 20 | 50 | 100
F_4	MWIR	III-V T2SL nBn | Graded Absorber	0 | 2 | 5 | 10 | 20 | 50 | 100

*1 TID = 7.5×10^9 p/cm^2

Again, the relationship between minority carrier recombination rate was shown to be linear with proton fluence, and the results are superimposed in Figure 4.9.

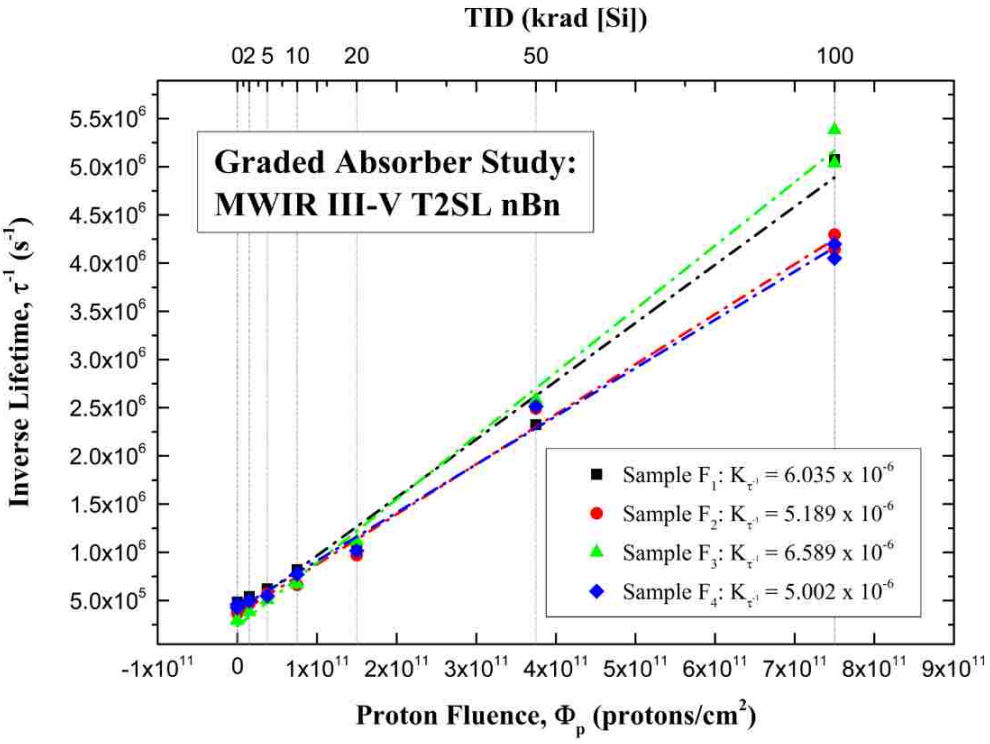

Figure 4.9: Lifetime damage factor extraction for samples F_1-F_4.

Although information on the absorber doping gradients is proprietary, it is obvious that changes in gradient design have an effect on the radiation hardness of the minority carrier lifetime, even when all the samples start with approximately the same lifetime value.

Radiation experiment #4 was similar to #2 in that it included samples from both traditional II-VI HgCdTe and III-V T2SL *nBn* structures. These HgCdTe samples were sourced from two different R&D groups, of which neither were the suppliers of the samples previously discussed ($D_{1\text{-}3}$). Details for this sample set are shown in Table 4.6.

Table 4.6: Details of sample set #4

Sample	λ_c (μm)	Composition	Cumulative Dose Schedule (TID)*
G_1	MWIR	III-V T2SL nBn	0 | 5 | 20 | 50 | 100
G_2	MWIR	III-V T2SL nBn	0 | 5 | 20 | 50 | 100
G_3	MWIR	III-V T2SL nBn	0 | 5 | 20 | 50 | 100
H	5.7	III-V T2SL nBn | N_d = low x 10^{15} cm^{-3}	0 | 5 | 20 | 50 | 100
I	5.4	LPE HgCdTe | N_d = 2.5 x 10^{15} cm^{-3}	0 | 5 | 20 | 50 | 100
J_1	3.9	HgCdZnTe | MBE Prep #1	0 | 5 | 20 | 50 | 100 | 200
J_2	3.9	HgCdTe | MBE Prep #1	0 | 5 | 20 | 50 | 100 | 200
K_1	3.9	HgCdZnTe | MBE Prep #2	0 | 5 | 20 | 50 | 100 | 200
K_2	3.9	HgCdTe | MBE Prep #2	0 | 5 | 20 | 50 | 100 | 200

*1 TID = 7.5 x 10^9 p/cm^2

Notice that from this point forward the cumulative dose schedule evolves to omit the smallest doses. Due to the fact that every sample characterized up to this point, regardless of vendor or design, exhibits the same trend in minority carrier lifetime degradation, it was decided that no damage factor information would be lost when omitting the small 2 and 5 krad doses. Again, the maximum dose in the schedule was increased for most II-VI samples. Superimposed damage factor results are provided for the III-V and II-VI samples in Figures 4.10 and 4.11, respectively.

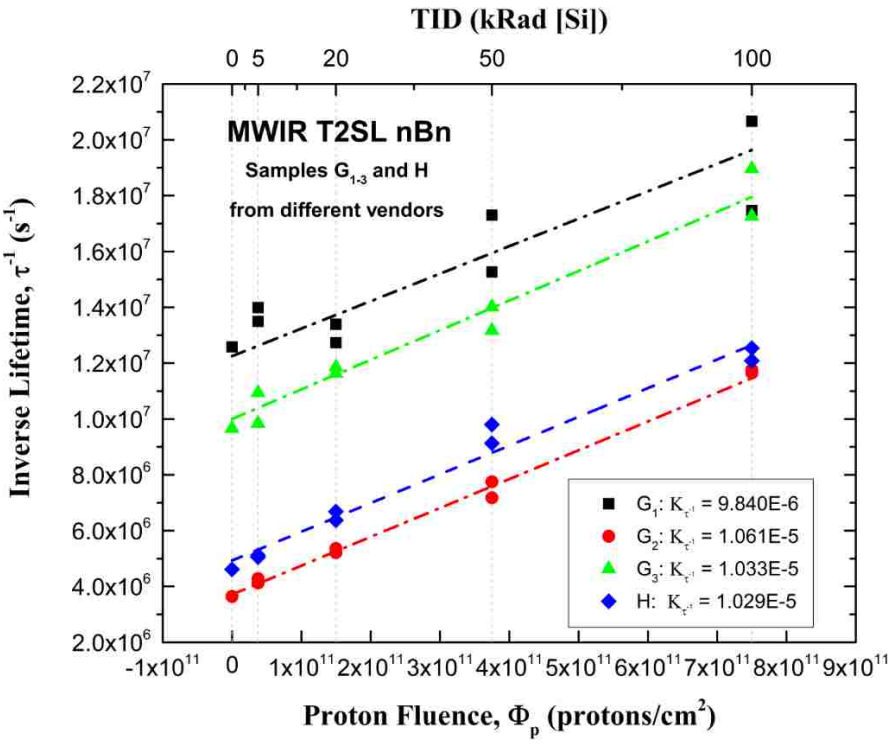

Figure 4.10: Lifetime damage factor extraction for samples $G_{1\text{-}3}$, and H.

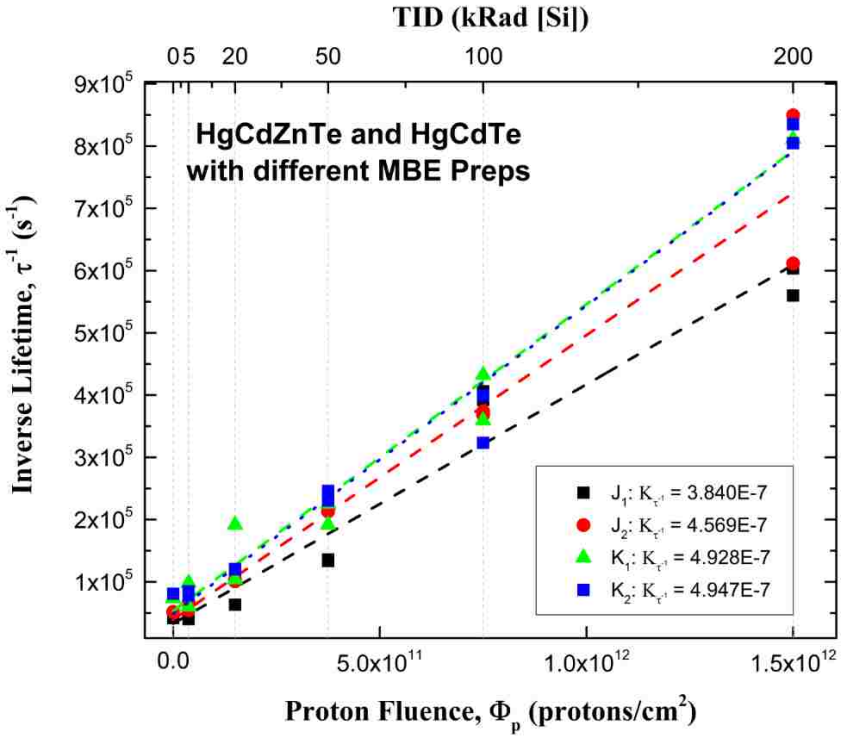

Figure 4.11: Lifetime damage factor extraction for samples $J_{1\text{-}2}$ and $K_{1\text{-}2}$.

The G series and H samples were sourced from different vendors (therefore having presumably different designs); however, it can be seen in Figure 4.10 that the degradation in minority carrier lifetime with proton fluence for these is nearly identical. Since all of these samples are InAs/InAsSb-based, it is reasonable to conclude that their *radiation hardness is more dependent on constituent materials than architecture*.

The final sample set discussed in this section was a study of the effect of lifetime radiation hardness vs. doping in MWIR III-V *nBn* structures. All eight samples were sourced from the same vendor with a high and low doping concentration for each of three different dopants plus a pair that were non-intentionally-doped (NID). Details of this sample set are outlined in Table 4.7.

Table 4.7: Details of sample set #5

Sample	λ_c (µm)	Composition	Cumulative Dose Schedule (TID)*
L_1	MWIR	III-V T2SL nBn | N_D = NID 2.4 x 10^{14} cm^{-3}	0 | 10 | 20 | 50 | 75 | 100
L_2	MWIR	III-V T2SL nBn | N_D = NID 1.1 x 10^{15} cm^{-3}	0 | 10 | 20 | 50 | 75 | 100
M_3	MWIR	III-V T2SL nBn | N_D = Si 1.1 x 10^{15} cm^{-3}	0 | 10 | 20 | 50 | 75 | 100
M_4	MWIR	III-V T2SL nBn | N_D = Si 8.0 x 10^{15} cm^{-3}	0 | 10 | 20 | 50 | 75 | 100
N_1	MWIR	III-V T2SL nBn | N_D = Te 3.0 x 10^{15} cm^{-3}	0 | 10 | 20 | 50 | 75 | 100
N_2	MWIR	III-V T2SL nBn | N_D = Te 9.0 x 10^{15} cm^{-3}	0 | 10 | 20 | 50 | 75 | 100
O_3	MWIR	III-V T2SL nBn | N_D = Be < 1 x 10^{15} cm^{-3}	0 | 10 | 20 | 50 | 75 | 100
O_4	MWIR	III-V T2SL nBn | N_D = Be < 5 x 10^{15} cm^{-3}	0 | 10 | 20 | 50 | 75 | 100

*1 TID = 7.5 x 10^9 p/cm^2

The results for each pair (dopant type) are plotted individually in Figures 4.12-4.15 to show the relative effect of doping level, and they are all superimposed in Figure 4.16 to show the relative effect of doping type. Units of doping concentration are cm^{-3}.

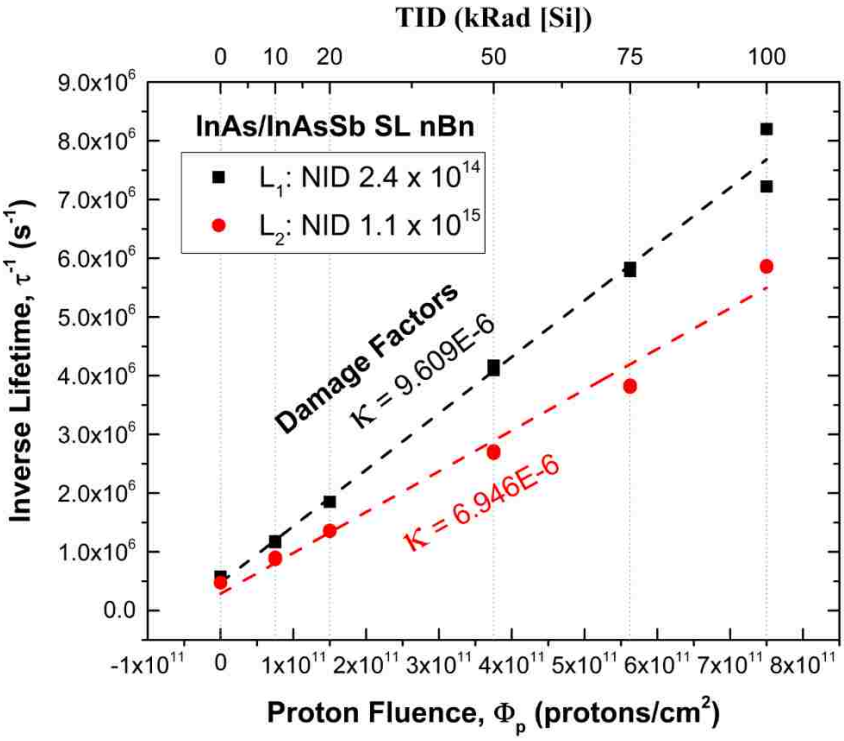

Figure 4.12: Lifetime damage factor extraction for samples $L_{1\text{-}2}$.

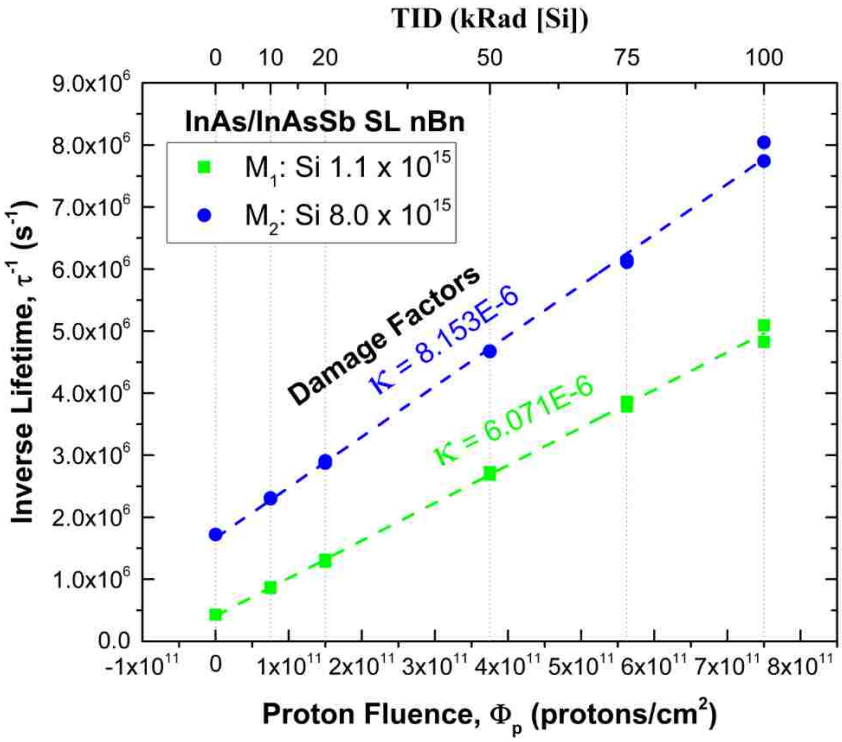

Figure 4.13: Lifetime damage factor extraction for samples $M_{1\text{-}2}$.

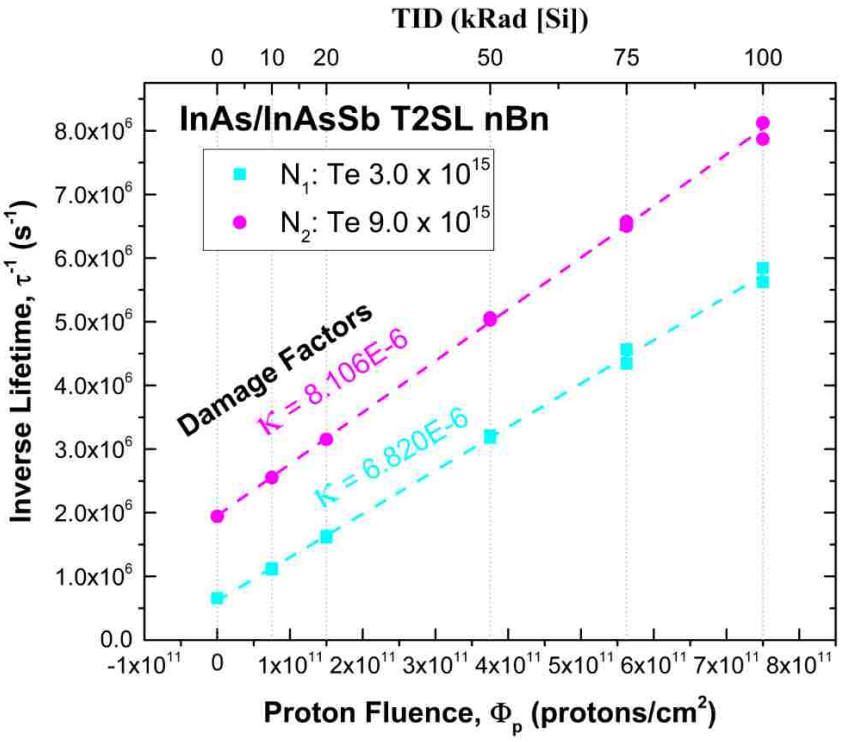

Figure 4.14: Lifetime damage factor extraction for samples $N_{1\text{-}2}$.

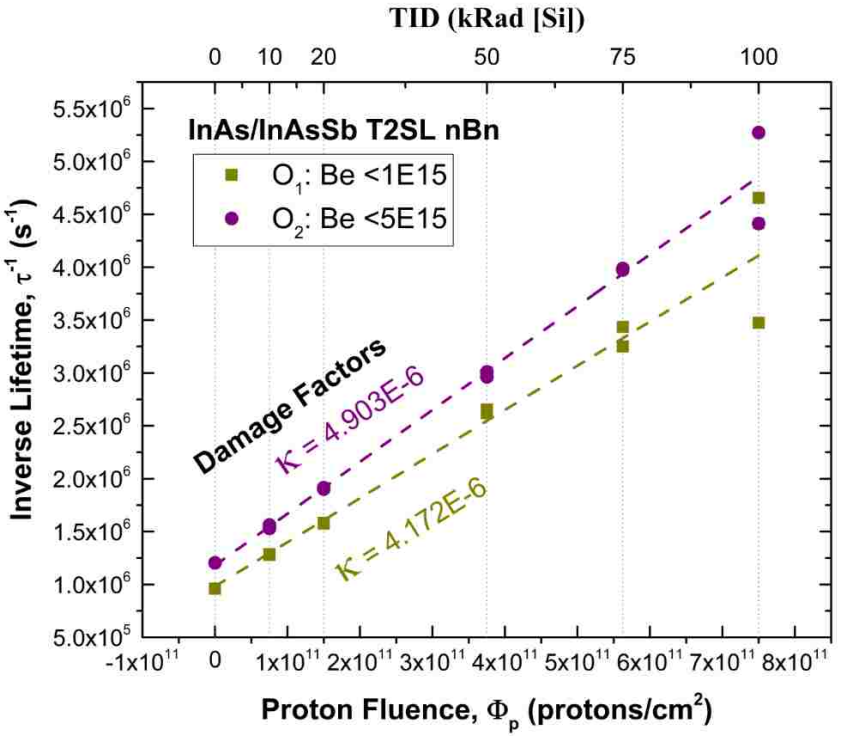

Figure 4.15: Lifetime damage factor extraction for samples $O_{1\text{-}2}$.

It should be noticed from these results that, without exception, the sample with the lower doping concentration results in both a smaller (superior) lifetime damage factor and longer initial minority carrier lifetime.

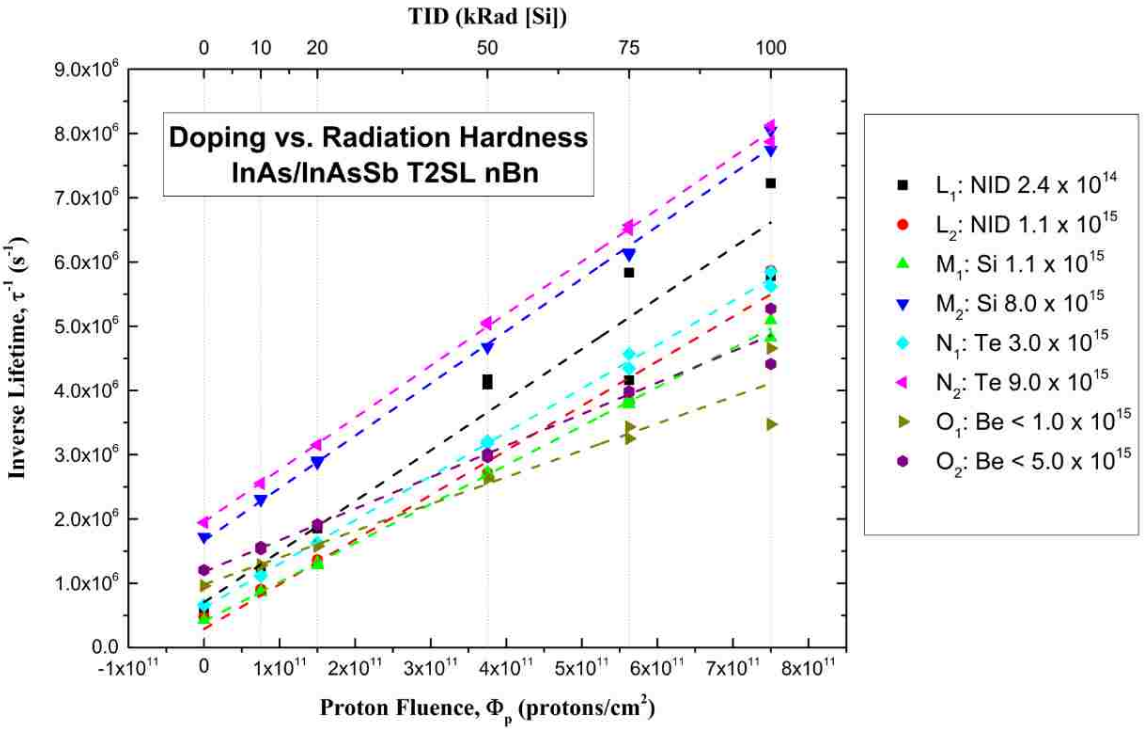

Figure 4.16: Lifetime damage factor extraction for sample set #5.

The takeaway from Figure 4.16 is that using Beryllium as a dopant results in better radiation hardness as far as minority carrier lifetimes are concerned, while results for NID, Silicon, and Tellurium dopants all remain in the same family.

The samples received to date are an indication of the state-of-the-art in space detectors, and Figure 4.17 provides a dramatic snapshot of relative inherent radiation hardness performance between the competing III-V and II-VI technologies, as far as minority carrier lifetime is concerned. HgCdTe remains the dominant performer using the lifetime damage factor metric by over an order of magnitude, regardless of sample vendor.

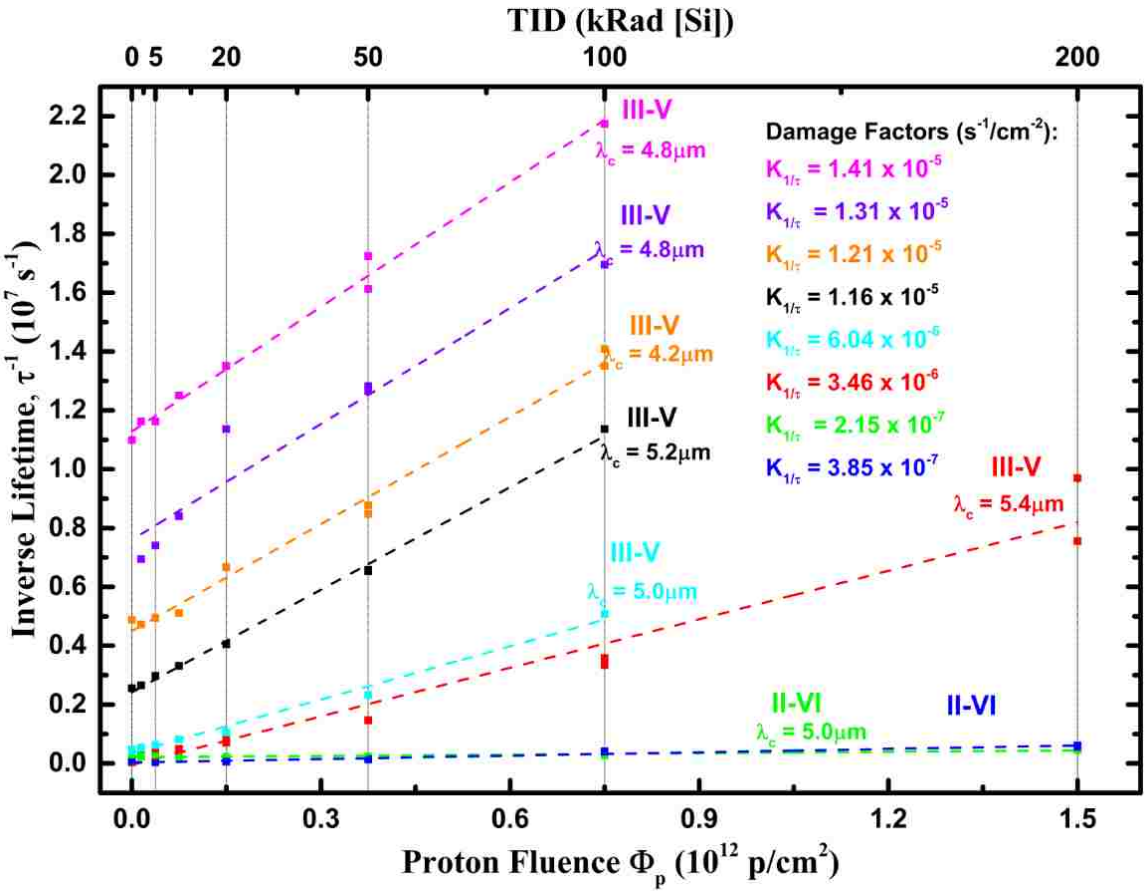

Figure 4.17: Aggregate lifetime damage factor results between competing III-V and II-VI infrared detector technologies.

4.2.2 Post-radiation Annealing: III-V vs. II-VI

Recall from the radiation test protocol outlined in Chapter 3 that minority carrier lifetime was characterized as a function of temperature both before and after radiation and subsequent anneals. These data will be reviewed in this section, and there exist significant differences in annealing phenomena between III-V and II-VI samples, including annealing temperature thresholds, annealing time dependence, and post-annealing lifetime changes.

Although lifetime damage factors appear largely agnostic to sample structure, absolute lifetime is not; therefore, the lifetime vs. temperature curves vary from sample to sample as researchers try new designs. There is, however, a noticeable dependence in post-irradiation lifetime recovery on constituent materials. This work revealed that the post-anneal behavior in HgCdTe samples is nearly identical, regardless of which R&D group it was sourced from, and the case is similar for the III-V samples, though there is a large disparity here between the two material systems.

A superposition of four temperature sweeps for a HgCdTe sample is shown in Figure 4.18, showing the lifetime vs. temperature behavior before radiation, after the entire proton irradiation dose schedule, and after two subsequent thermal anneals.

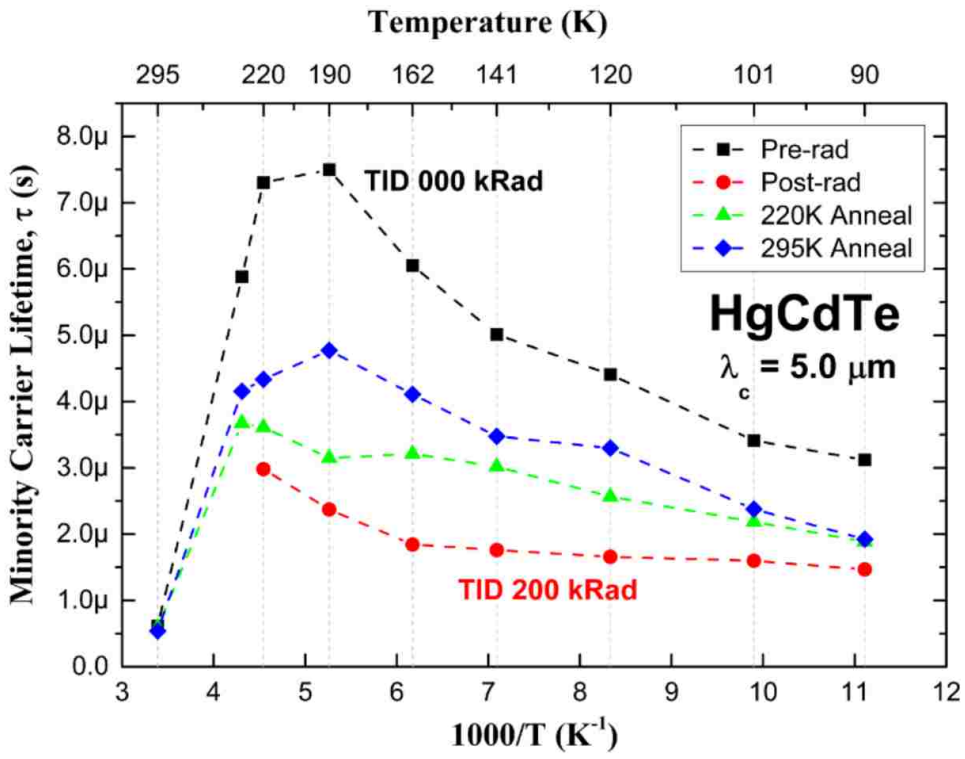

Figure 4.18: Lifetime vs. temperature sweep example (HgCdTe).

The duration of these anneals was determined by how long it took to complete a full characterization of all samples at least once, typically 1-2 hours, as it was believed that

post-anneal lifetime recovery was a function of temperature alone, not time. From Figure 4.18, it is obvious that the minority carrier lifetime was significantly improved after each level of annealing, indicating that the mobility of the defects created in the crystal lattice is a strong function of temperature, allowing defect pairs (i.e. vacancies and interstitials) to recombine thus removing their electronic effects from the structure. A satellite mission planner would be most interested in the lifetime recovery at the operating temperature (120 K for all radiation testing in this work); therefore, a convenient visual representation of these data points can be included relative to those in the irradiation study as shown in Figure 4.19.

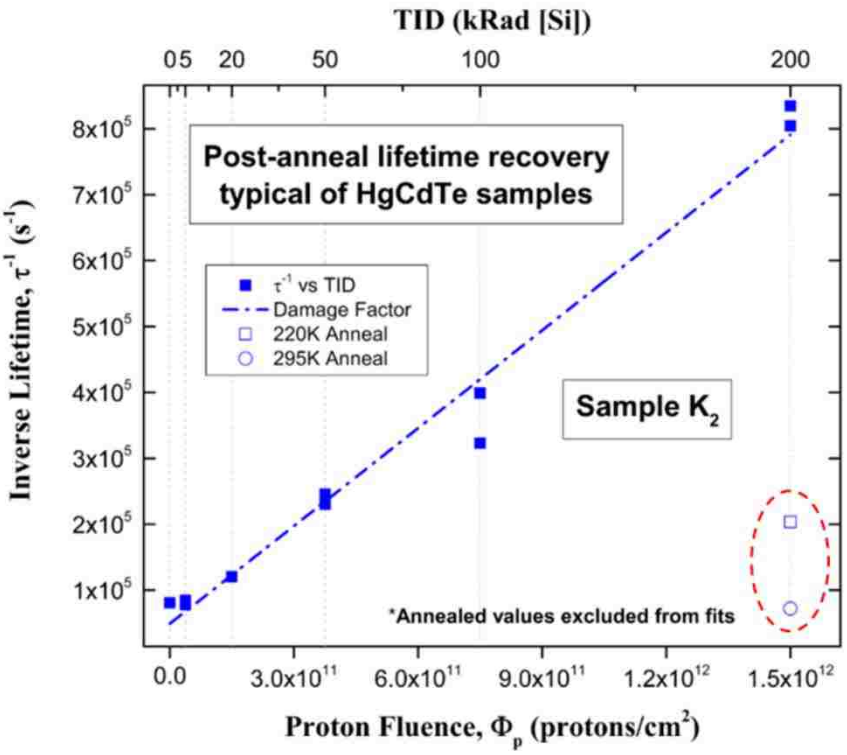

Figure 4.19: Post-anneal lifetime recovery example (HgCdTe).

The same analyses were performed for the III-V samples as well. Figure 4.20 contains the superposition of temperature sweeps for samples $G_{2\text{-}3}$ (MWIR III-V T2SL *nBn*).

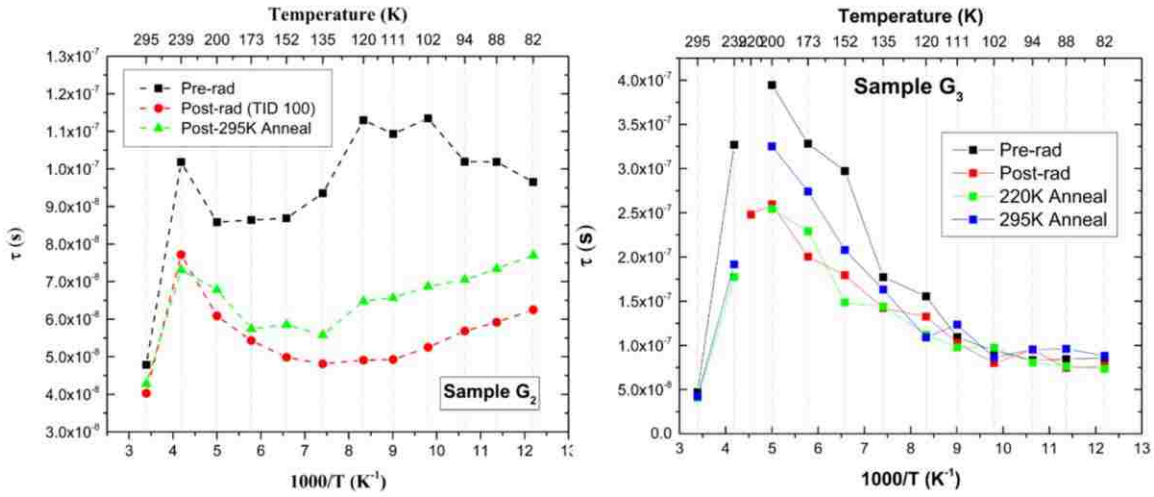

Figure 4.20: Lifetime vs. temperature sweep examples (InAs/InAsSb).

The 220 K anneal temperature sweeps were soon abandoned for the III-V samples after repeatedly observing no recovery in the minority carrier lifetime, indicating that the mobility of the defects created in these structures has a higher temperature threshold than that of HgCdTe. The best case scenario witnessed for lifetime recovery in III-V samples is shown in Figure 4.21, where the post-anneal lifetimes recovered to their values at approximately TID 50 krad [Si].

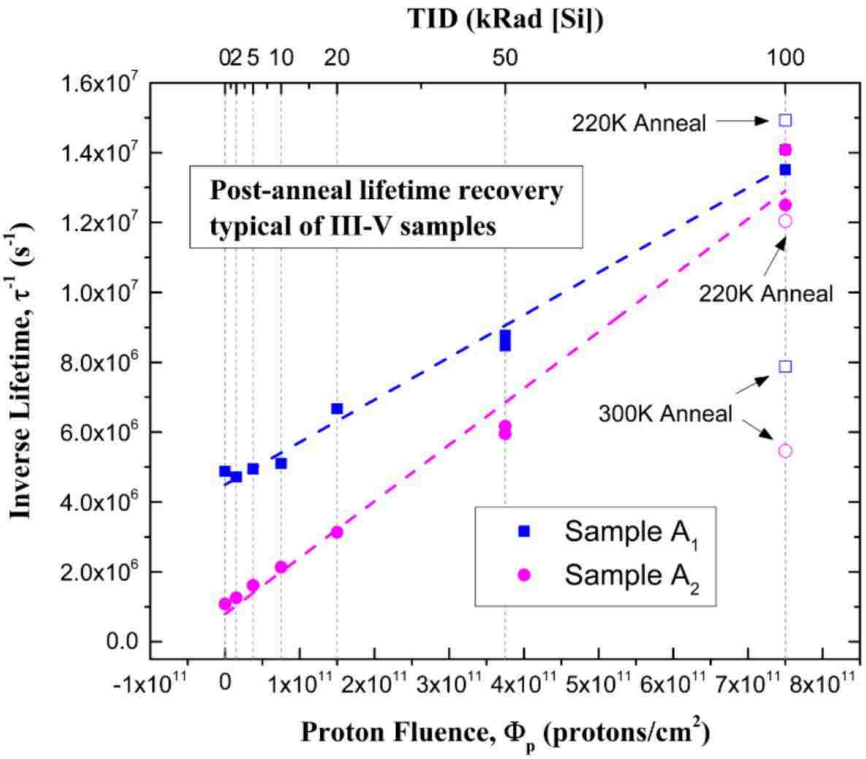

Figure 4.21: Post-anneal lifetime recovery example (InAs/InAsSb).

Clearly, the differences in annealing phenomena between the II-VI and III-V samples is significant, both in magnitude of lifetime recovery and in the dependence of defect mobility on temperature.

Finally, a study was performed on the annealing time dependence on some III-V samples from set #5. II-VI samples were excluded here due to their previously observed, near complete recovery after short durations at 300 K, also referred to herein as room temperature (RT). Here, the minority carrier lifetimes were characterized per the normal test protocol, and then temperature sweeps were performed after RT anneals with durations of one day, two weeks, and 4 weeks. Example data from sample L_1 are shown in figure 4.22.

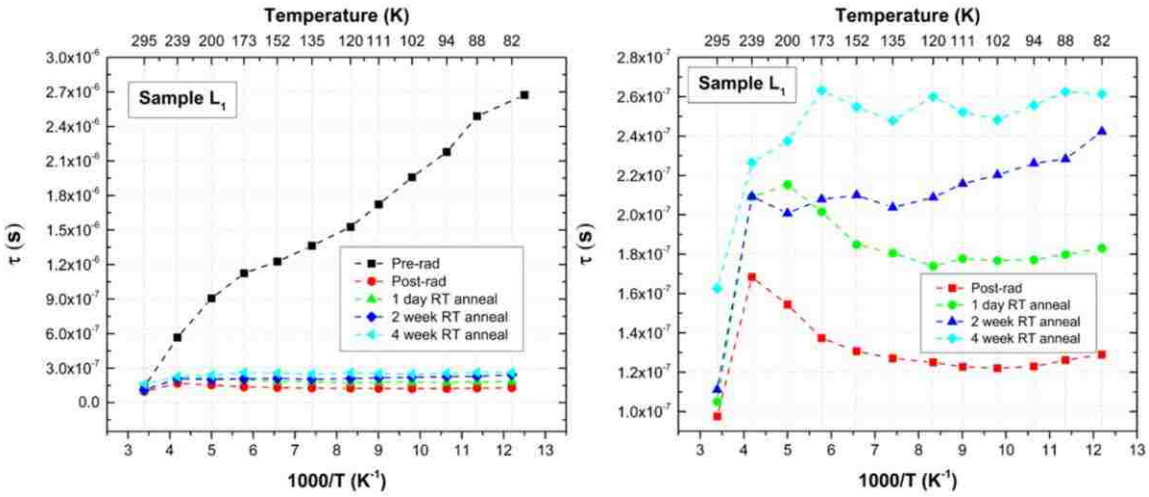

Figure 4.22: Time dependence of post-anneal lifetime recovery for L_1.

This experiment conclusively indicates that there does exist a time dependence on lifetime recovery through annealing; however, the magnitude of the lifetime recoveries remained very small.

4.2.3 III-V T2SL *nBn* NIEL Study: 63 vs. 8.2 MeV

Here, data and analyses are presented on the degradation of minority carrier lifetime in several InAs/InAsSb superlattice detector structures resulting from 8.2 and 63 MeV stepwise proton irradiation to correlate damage factors with NIEL. Preceding research efforts on the effects of charged particle radiation on semiconductor parameters has been performed on several different electronic devices and materials [**29**,**31**,**32**], all of which conclude that damage factors, regardless of parameter, exhibit a linear relationship with calculated non-ionizing-energy-loss (NIEL) of the weighted combination of constituent elements [**76**,**77**,**33**]. This work reveals that InAs/InAsSb T2SLs follow the same behavior; however the damage factors more closely follow the Coulombic rather than nuclear subcomponent of total NIEL. This knowledge allows mission planners and

designers to extrapolate parameter damage factors to different proton energies as differential proton energy spectra are highly dependent on orbit altitude and trajectory [**35**]. In addition to relating InAs/InAsSb T2SL lifetime damage factors to NIEL, these results show that lower initial n-type doping levels result in higher radiation tolerance (lower τ degradation rate).

In order to quantify the difference between 8.2 MeV and 63 MeV lifetime damage factors, different copies of each sample must be tested at each proton energy. Sample set #6, used for this low energy proton study and detailed in Table 4.8, was comprised of pristine (non-irradiated) versions of samples A_1, A_2, B_1, and B_2 previously characterized at 63 MeV.

Table 4.8: Details of sample set #6

Sample	λ_c (μm)	Composition	Cumulative Dose Schedule (TID)*
A_1	4.2	III-V T2SL nBn | Doping = NID	0 | 2 | 5 | 10 | 20 | 35 | 50 | 100
A_2	4.2	III-V T2SL nBn | Doping = 1 x 10^{16}cm^{-3}	0 | 2 | 5 | 10 | 20 | 35 | 50 | 100
B_1	5.2	III-V T2SL nBn | Doping = 4 x 10^{15}cm^{-3}	0 | 2 | 5 | 10 | 20 | 35 | 50 | 100
B_2	5.2	III-V T2SL nBn | Doping = 8 x 10^{15}cm^{-3}	0 | 2 | 5 | 10 | 20 | 35 | 50 | 100

*1 TID = 1.372 x 10^9 p/cm^2

Again, TID values are represented in krad [Si]; however, where 1 krad for the previously used 63 MeV protons is equivalent to a particle fluence of 7.5×10^9 p/cm^2, 1 krad for 8.2 MeV protons in this experiment is equivalent to ~1.4×10^9 p/cm^2, thus requiring less fluence to reach an equivalent total ionizing dose.

The test configuration had to be changed to accommodate the lower energy protons due to the fact that they would not have penetrated the 2 mm thick BaF_2 windows according to SRIM analysis. A window made out of a 3 mil (0.003 inch) sheet of Dura-Lar® was crafted which allowed transmission of the injection laser pulses, MWIR PL

emission from samples, and the 8.2 MeV protons. Using a thin film as a window generated a new set of challenges. First, when high vacuum is created within the cryostat, as is necessary for cryogenic cooling, the film becomes concave. To prevent the film from contacting the samples, a thinner Aluminum sample holder disc was fabricated (5 mm vs. the previously used 10 mm). Second, with the cryostat undergoing cryogenic cooling, water had a tendency to condense on the film window. This was solved by creating a constant flow of dry nitrogen (N_2) across the film window with a fan spreading nozzle [**78**]. Finally, vacuum hold times within the cryostat suffered with the thin film window requiring more frequent vacuum pumping. The resulting test configuration is outlined in Table 4.9.

Table 4.9: Test configuration #3

Detector λ_c (µm)	**Pre-amp BW (MHz)**	**Window**	**Proton Energy (MeV)**	**LPF (µm)**
6.0	300	Duralar® (3 mil)	8.2	1.6

Data resulting from this experiment followed the same trends as those taken with the same samples with 63 MeV protons (linear increase in recombination rate with proton fluence), the major difference being that the low energy protons degraded the minority carrier lifetime at a much higher rate. For visual comparison, the results from both high and low energy protons from sample B_1 are superimposed in Figure 4.23. This is representative of the results from all four samples.

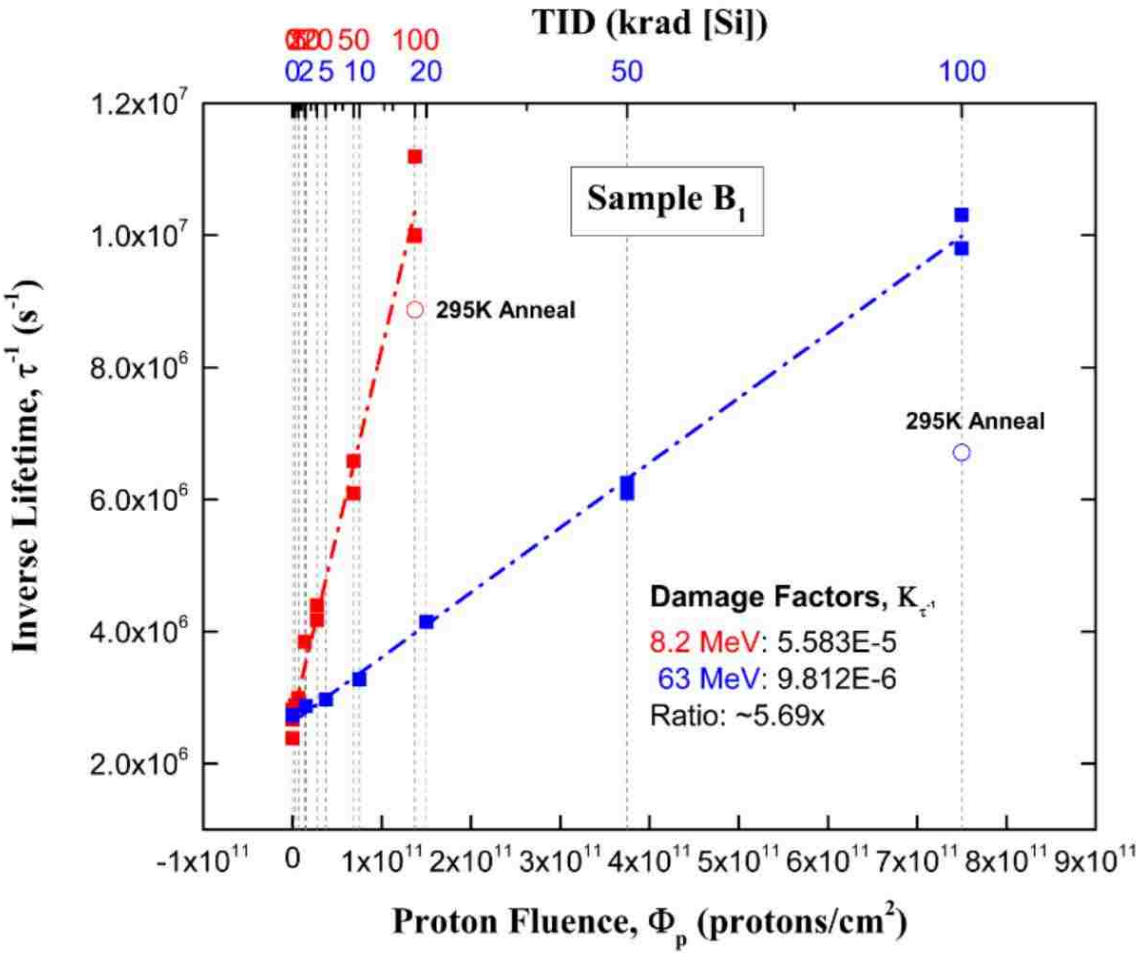

Figure 4.23: plot of reciprocal lifetime (τ^{-1}) vs. proton fluence (Φ_p) for two different energies (8.2 and 63 MeV). Damage factors ($K_{\tau^{-1}}$) are slopes of linear fits.

The low energy proton damage factors are ~4-6 times higher (worse) than their high energy proton counterparts. A numerical summary of these results is provided in Table 4.10. These results were as expected due to the higher probability of lower kinetic energy particles of becoming embedded in the semiconductor lattice during which a large amount of energy is imparted to the material according to NIEL (shown below). Results were also in-line with previously reported results on Si and GaAs [**27**].

Table 4.10: Low vs. high energy proton lifetime damage factors

Sample	λ_c (μm)	Doping [cm^{-3}]	K_{63} [τ^{-1}/Φ_p]	$K_{8.2}$ [τ^{-1}/Φ_p]	K Ratio
A_1	4.2	NID	9.50×10^{-6}	4.92×10^{-5}	5.18
A_2	4.2	1×10^{16}	1.62×10^{-5}	6.85×10^{-5}	4.24
B_1	5.2	4×10^{15}	9.81×10^{-6}	5.58×10^{-5}	4.57
B_2	5.2	8×10^{15}	1.33×10^{-5}	6.06×10^{-5}	5.69

In order to use these results to predict damage factors for a continuum of proton kinetic energies, they must be related to the NIEL values of the detector material, which were generated with the SR-NIEL calculator [**43**] for $InAs_{0.5}Sb_{0.5}$ with displacement threshold energies (E_d) of 21 eV each for In, As, and Sb, respectively.

Both the NIEL curve and the damage factors were normalized at a proton energy of 8.2 MeV. The 63 MeV damage factors were plotted on a relative scale using the right vertical axis. See Figure 4.24.

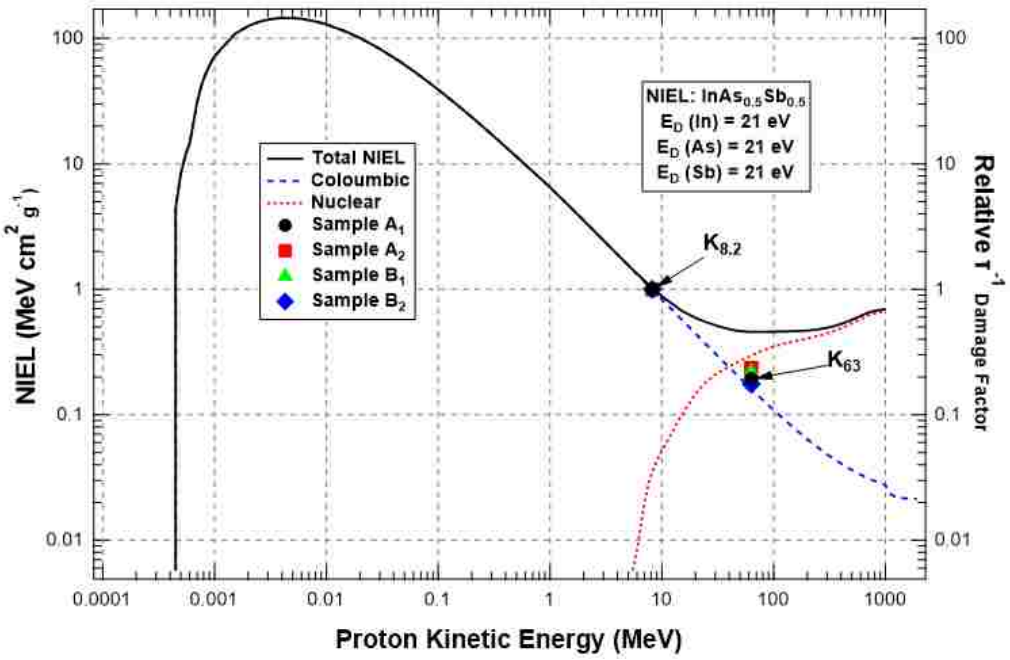

Figure 4.24: Non-ionizing-energy-loss (NIEL) and reciprocal lifetime damage factors vs. incident proton energies for InAsSb.

This reveals that the damage factor dependence on proton energy does indeed follow the NIEL calculations for InAsSb; however, the damage factors follow the Coulombic interaction subcomponent of total NIEL more closely, at least out to 63 MeV. It appears that at energies higher than 63 MeV, where the nuclear interaction subcomponent becomes stronger, the damage factors will increasingly stray from the Coulombic curve toward the nuclear and total NIEL curves.

These results suggest that using total NIEL can result in overestimation of the lifetime damage factors of InAs/InAsSb SLS *nBn* detectors at higher kinetic energies, and this is consistent with similar studies on GaAs structures and InGaAs/GaAs LED lifetime degradation [**76**,**79**]. Since the damage factors exhibit a linear relationship to NIEL it appears that no special treatment is needed to account for complex *nBn*/T2SL structures.

Now that damage factors may be predicted over a wide range a proton kinetic energies, degradation over an entire mission for an InAsSb-based sensor may be predicted using Equation 1.7 (repeated below as 4.1) given the differential proton energy spectra and mission duration (t_m) for a selected shield/orbit combination [**38**].

$$\text{Carrier recombination rate, } \tau^{-1} = t_m \cdot \int_0^{\infty} \kappa_{\tau^{-1}}\left(E_{ref}\right) \frac{NIEL(E)}{NIEL(E_{ref})} \cdot \frac{d\varphi(E)}{dE} dE, \qquad (4.1)$$

For each cutoff wavelength (T2SL design), the samples with the lower doping concentrations exhibited less rapid minority carrier lifetime degradations, or smaller damage factors. Another observation that can be made from Fig 4.23 is the differences in recombination lifetime recovery after room temperature (295 K) annealing. Post-irradiation, the recombination lifetimes were measured through a series of temperature sweeps from liquid nitrogen (LN_2) to room temperatures, then re-characterized at 120 K.

As has been observed in many other III-V materials dosed at 63 MeV to date, lifetimes approximately recovered to their TID 50 (krad [Si]) levels; however, little to no recombination lifetime recovery was seen in these samples that were dosed at 8.2 MeV, as shown in Fig 4.25.

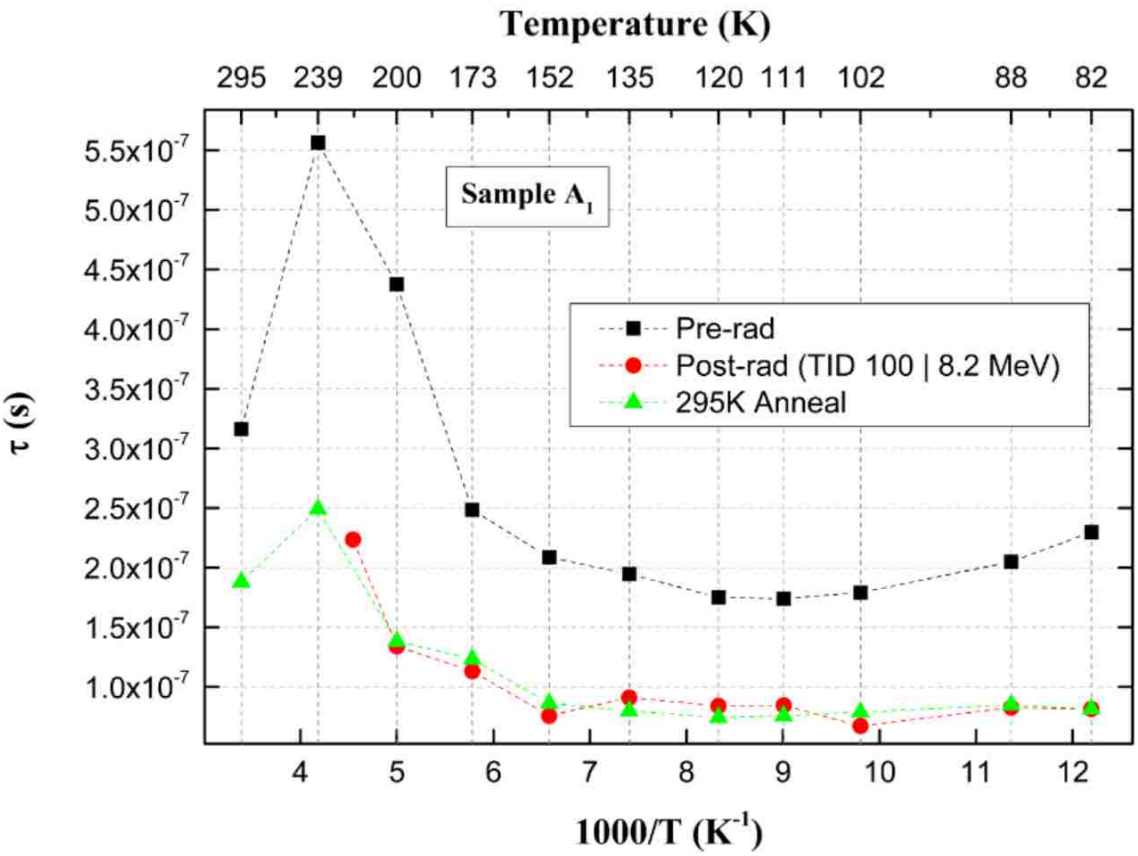

Figure 4.25: Minority carrier lifetime (τ) for sample A_1 vs. temperature for before and after 8.2 MeV proton irradiation and anneals.

4.3 Summary

Presented in this chapter was a study of how minority carrier recombination lifetimes of various MWIR III-V *nBn* and II-VI HgCdTe space detector materials degrade with stepwise, 63 MeV proton irradiation up to fluences of 7.5 x 10^{11} p/cm^2 and higher. Lifetimes were measured using the TRPL technique while samples were held at 120 K to

limit thermal annealing while simulating mission operating conditions. As expected, the recombination rate of each sample was found to increase with proton fluence at a constant rate, implying a linear increase in the material defect concentration with increased proton fluence. The rates of change in the carrier recombination rate of each sample (minority carrier lifetime damage factors), were then plotted together as a function of initial recombination rates (see Chapter 5). Juxtaposing the III-V and II-VI results showed a distinct disparity with the lifetime of the incumbent detector material, HgCdTe, being roughly an order of magnitude more radiation-tolerant to displacement damage from proton irradiation than any of the III-V-based *nBn* materials. Results from the latter also suggest some degree of interrelation between the damage factors and their initial lifetimes. Finally, the annealing behavior of each material's lifetimes revealed that HgCdTe tends to anneal to near 100% recovery at 295 K whereas III-V materials recovered to only about 0-50% under the same conditions.

The samples discussed herein were sourced from several independent research entities or foundries and encompass a variety of cutoff wavelengths and structural designs. Given that the effects of proton irradiation on inverse lifetime follow the same trends regardless of these design differences, it shows that this characterization capability can be a used as a quality feedback mechanism for relative performance between prototype detector structures before major investments are made in flight quality focal plane array (FPA) development. Although improvements have been observed with III-V prototypes, in characterizations performed to date, HgCdTe remains the dominant performer over the InAs/InAsSb T2SL *nBn* technology in terms of lifetime magnitude, lifetime radiation hardness, and post-anneal lifetime recovery (both magnitude and

required time under conditions tested). To quantify this, the radiation hardness of minority carrier lifetimes in some III-V materials have been empirically observed to fall ~16x of that in II-VI materials that were characterized for reference. This is nearly a 5x improvement from the majority of III-V samples tested previously.

Chapter 5

Physics-based Insights

5.1 Introduction

The effects of charged particle radiation on semiconductor compounds can be quite complex at the microscopic level. Atomic-level phenomena are determined by many parameters. Factors from the incoming particle include: kinetic energy, mass, charge, charge polarity, and orientation with respect to target's crystal structure. For the target material, this includes: temperature, atomic masses of constituent elements, atomic bond type, purity, lattice spacing, free carrier concentration, and impurity energy level and polarity. Time is another important factor. Even if a defect is created, e.g. a vacancy-interstitial (V-I) pair via displacement damage, it could immediately recombine therefore removing itself, remain a single point defect, or transfer energy to other atoms creating a defect complex via cascades of collisions. This is termed *defect stability* and is a function of temperature. These stable defects are what influence the electrical properties of a material through the generation of one or more energy levels within the forbidden energy bandgap [**80**]. Textbooks dedicated to this subject [**81**] admit that the link between original displacement damage and final stable defect structures that form is not straightforward and therefore not easy to model.

Displacement damage in a single, pure material (e.g. Silicon), simply creates a V-I pair, the vacancy and interstitial having their own, separate mobilities dependent on

temperature. When impurities are present, e.g. oxygen or phosphorous, the interactions of each counterpart of a V-I pair can manifest differently to alter the electrical properties of the material. For example, some well-known radiation defects in silicon include the A center (vacancy-oxygen pair) and the E center (phosphorous-vacancy pair). This becomes more complex for semiconductor compounds, such as the InAsSb-based samples characterized in this work, where anti-site defects can also interact with vacancies and interstitials.

It is obvious from the previous chapter that the minority carrier recombination lifetime changes significantly with displacement damage, but what is the underlying physical mechanism? Results from other researchers [**82**,**83**,**84**] monitoring resistivity vs. radiation in similar materials have concluded that radiation-induced deep energy level defects change the free-carrier charge balance in a semiconductor by shifting the Fermi level. This shift occurs when the deep levels trap or compensate shallow dopants, thereby preventing ionization to the relevant energy band by trapping their charge carriers.

In this work, it was consistently shown that the minority carrier lifetimes were longer for samples with lower doping concentrations. It follows that reductions in the minority carrier lifetime stem from a Fermi level shift toward the conduction band, increasing the net majority free-carrier concentration via defects residing at levels closer to the conduction than valence band. This is consistent with other results concluding that, in general, the response of III-V compounds (and CdTe) to radiation is increasing n-type carrier concentrations [**85**,**86**,**87**,**88**,**89**]. See Table 5.1.

Table 5.1: Radiation effects on selected semiconductor compounds

Material	Radiation Effect
n-type InSb	n_0 approaches 4 x 10^{16} [cm^{-3}]
p-type InSb	type conversion to n-type
n-type AlSb	n_0 approaches a limiting concentration
p-type AlSb	type conversion to n-type
n-type InAs	n_0 increases indefinitely
p-type InAs	type conversion to n-type
p-type CdTe	type conversion to n-type

Now that it is understood why the minority carrier lifetime decreases in the tested material systems vs. displacement damage, an attempt will be made at understanding the fundamental material properties causing the disparities in both damage factors and post-radiation annealing behavior.

5.2 Damage Factor Disparities: III-V vs. II-VI

A simplified summary of the lifetime damage factor disparities between these competing material systems is shown in Figure 5.1, labeled with some fundamental differences between the elemental compounds.

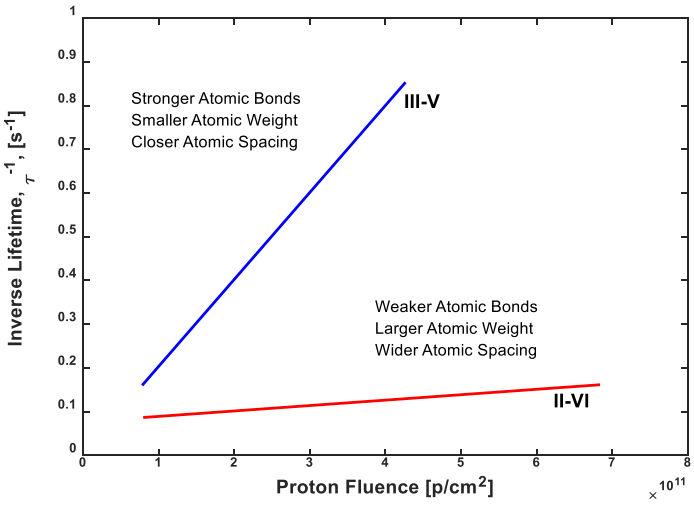

Figure 5.1: Simplified summary of damage factor disparity

Some hypotheses can be derived from this work on the reasons for the fundamental differences in radiation tolerance between these materials, focusing on *differing atomic numbers and bond strengths.* The bond strengths in HgCdTe are relatively low due to a higher prevalence of ionic cohesion [**90**,**91**] with relatively larger atomic numbers of the constituent atoms. The III-V materials have stronger chemical bonds (covalent) and smaller atomic numbers of constituent atoms. It is intuitive to think that weaker bonds in HgCdTe could result in easier displacement damage; therefore, an initial hypothesis was that the larger atoms were not displaced as far away from their origins relative to the displacement of smaller atoms in the III-V materials. The significance of this would be that the vacancy-interstitial defect pairs in heavier atoms more readily recombine almost instantly since they weren't displaced as far, and this could be aided by the higher defect mobility presumably due to weaker bonds.

Consider the energy a relativistic charged particle imparts to the primary knock-on (or recoil) atom in a material. The maximum energy transferred in an elastic collision where momentum is conserved is [**92**]

$$E_p(Max) = \frac{4EMm}{(M+m)^2}, \tag{5.1}$$

where *E* and *M* are the energy and mass of the incident particle and *m* is the mass of the target atom. Simplified to the atomic weight scale this reduces to

$$\mathrm{E_p(Max)} = \frac{4\mathrm{E}}{\mathrm{A}}, \tag{5.2}$$

where *A* is the atomic weight of the target atom.

Using this equation to compare the energies imparted to target particles of averaged atomic weights of $InAs_{0.5}Sb_{0.5}$ (~107) and $Hg_{0.5}Cd_{0.5}Te$ (~142) one can see that,

indeed, less energy is transferred to the larger II-VI atoms; however, the resulting ratio of ~1.33 does not alone account for the observed >10x disparity in lifetime damage factors.

A discussion of radiation effects is held for covalent and ionic materials in *Radiation Damage in Solids* by Billington and Crawford [**92**]. For covalently bound materials, the atoms are more rigidly fixed in position due to the overlapping wave functions of shared electrons having low energy in only certain directions. It is for this reason that the mobility of both vacancies and interstitials in covalently bonded materials is lower than that found in ionic materials. Additionally, dangling covalent bonds readily trap impurities, thereby locking them in place and creating stable defects. Due to the rigid nature of covalent bonds, atomic rearrangement to relieve local stresses cause by point defects is less likely than in ionic crystals.

In a study by Goldschmidt [**93**], it was concluded that the greater the ionicity (electrostatic cohesion) of atomic binding, the more resistive a material is to structural changes. In this case, there are no (or fewer) rigid directional bonds needed to be broken to accommodate atomic rearrangement to alleviate local stresses caused by point defects. Not only are vacancies and interstitials more easily able to recombine, energy imparted to these materials from impacting charged particles is mitigated by the vibration and relaxation of neighboring atoms or ions.

A conclusion that can be made with this information and results of this work is that radiation hardness of a material is more sensitive to differences in bond type (strength) than atomic mass, although atomic mass influences the ionic character in covalent bond structures and vice versa.

5.3 Post-radiation Annealing Disparities: III-V vs. II-VI

The disparity between III-V and II-VI detector structures in post-radiation annealing phenomena must be due to the same chemical bonding differences mentioned above. Although displacement damage is thermodynamically reversible, it was shown in this work that the activation energies (temperature) required to mobilize vacancy-interstitial pairs is higher in the III-V compounds which have a higher degree of covalent bonding. Recall Figure 4.19; here, the lifetime recoveries after the 220 K anneal were 0% and ~85% for the III-V and II-VI materials, respectively. After the room temperature anneal, the lifetime recoveries were approximately 50% and 100% for the III-V and II-VI materials, respectively. The conclusion here is that the temperature threshold for defect mobility in the III-V material system is much higher, which may be problematic for on-orbit annealing. The mobility of lattice defects is reported [**92**] to be

$$\mu_D \propto e^{1/T}, \tag{5.3}$$

which should be used in future analyses in designing post-radiation annealing experiments.

5.4 Summary

The minority carrier lifetime degradations observed vs. proton fluence in this work are attributed to, through displacement damage, the creation of defect concentrations with localized energy levels within the forbidden band gap of the semiconductor material under test. From observations of the relationship between minority carrier lifetime measurements and sample doping concentrations, it is concluded that the net result of these created defects is a shift of the Fermi level toward the conduction band, ultimately

altering the free carrier charge concentrations to be more n-type. This conclusion was consistent with results from other researchers on similar materials, which are summarized in Table 5.1

Initially counterintuitive, it is materials with higher prevalence of ionic bonding are both more tolerant to radiation and whose damage is more readily reversible. This is due to ionic bonds, which rely on a non-directional electrostatic attraction (Coulombic), that allow the vacancies and interstitials to more freely diffuse throughout a solid and annihilate each other more readily (higher % V-I recombination immediately after displacement with respect to covalently bonded III-V material) and at lower temperatures.

Microscopic analyses can be quite complex and difficult to model. Fortunately, it is the net macroscopic effect that these atomic rearrangements induce on electrical properties, such as reduction in minority carrier lifetime, that are of ultimate importance in determining the quality of a detector material. Extrapolating empirically determined damage factors using NIEL curves has been become standard for this reason.

Chapter 6

Final Discussions

6.1 The Challenge of Improving Space-based Detectors

Irradiation by high energy particles ubiquitous in space (e.g. electrons, protons, gamma and x-rays) can lead to ionizing and/or non-ionizing damage of semiconductor-based photodetectors depending on the material, design and passivation scheme as well as the nature of the incoming particle [**94**]. Ionization damage or total ionizing dose effects result when the incoming particle loses its energy by creating additional excited charge, which then becomes trapped at surfaces or in passivating dielectric layers. In the case of HgCdTe photodiodes or III-V Sb-based *nBn* detectors, excess electron-hole pair creation occurs which can charge surfaces and lead to increased surface leakage. For irradiation with massive particles such as protons, non-ionizing or displacement damage results when the incoming particle loses its energy via collisions with atoms, displacing them from their lattice sites and generating Frenkel pairs (i.e. vacancy-interstitial). These can diffuse and recombine or form stable defects or defect complexes. Depending on their nature, as depicted in Figure 6.1, these additional defects can act as recombination centers and decrease the minority carrier recombination lifetime τ, which can manifest as degradation of the detector performance (i.e. decrease in quantum efficiency η and increase in dark-current density J_D). The rate of the performance degradation is thus intimately dependent on the rate of τ degradation shown in this work. This connection

makes the lifetime degradation rate a key parameter in the overall radiation tolerance of a detector.

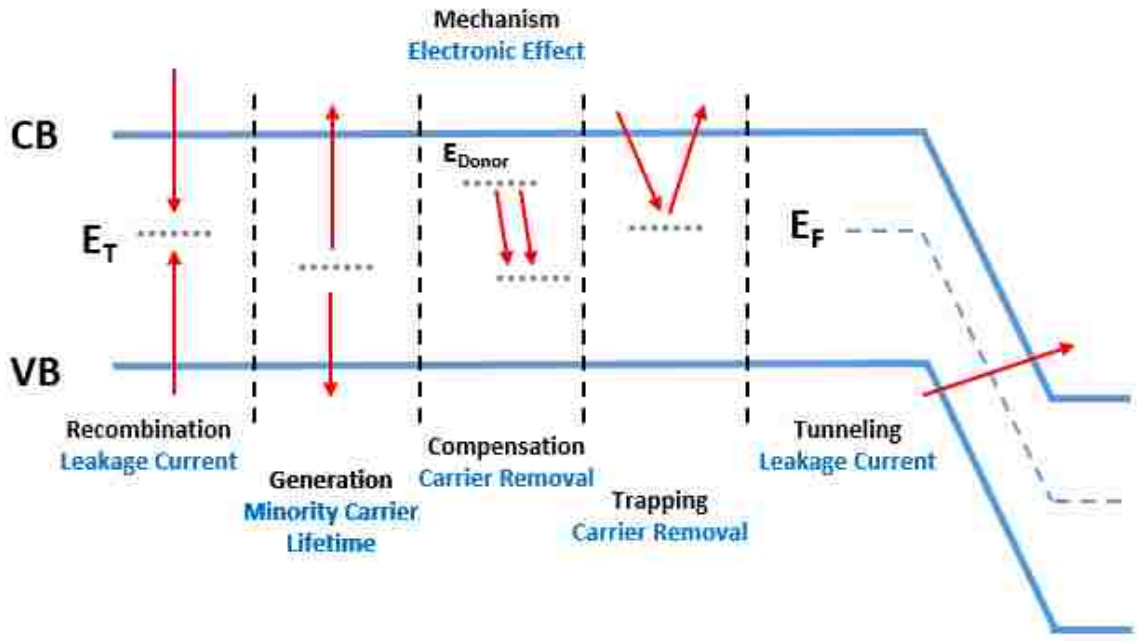

Figure 6.1: Electronic manifestation of displacement-damage-induced defects within a semiconductor.

6.2 Conclusions

The experiments performed in this work verified the hypothesis that, with charged particle radiation, the minority carrier lifetime is the culprit for degradations in higher level detector performance metrics such as dark current and quantum efficiency. Using this TRPL system to directly measure the radiation tolerance of the minority carrier lifetime on pre-processed samples can provide more rapid, inexpensive quality feedback to researchers by characterizing up to 20 samples (designs) at a time before investments are made in processing complete detectors. This can also enable the simulation of degradations in the higher level detector performance metrics rather than performing

expensive empirical studies on devices further along in the manufacturing process, examples of which are shown in Figures 6.2-6.3.

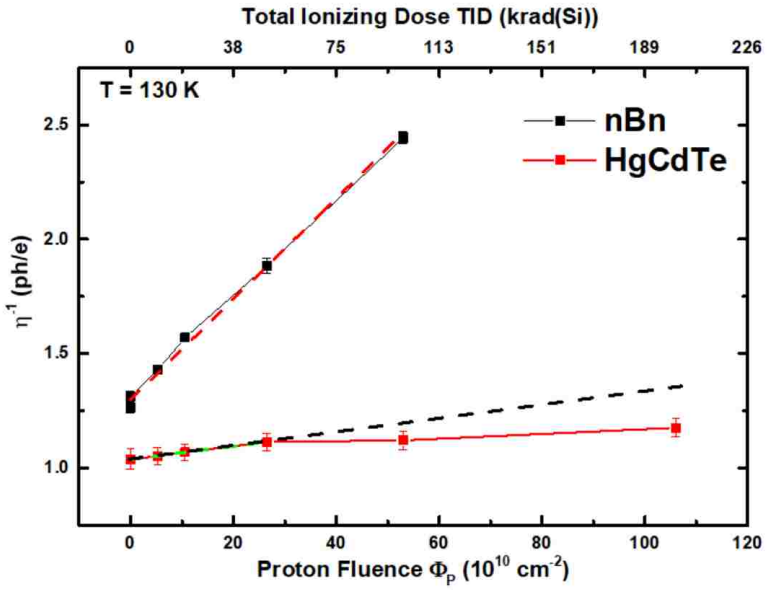

Figure 6.2: Examples of $\eta^{-1}(\Phi_p)$ for a typical MWIR HgCdTe photodiode and an III-V Sb-based *nBn* detector.

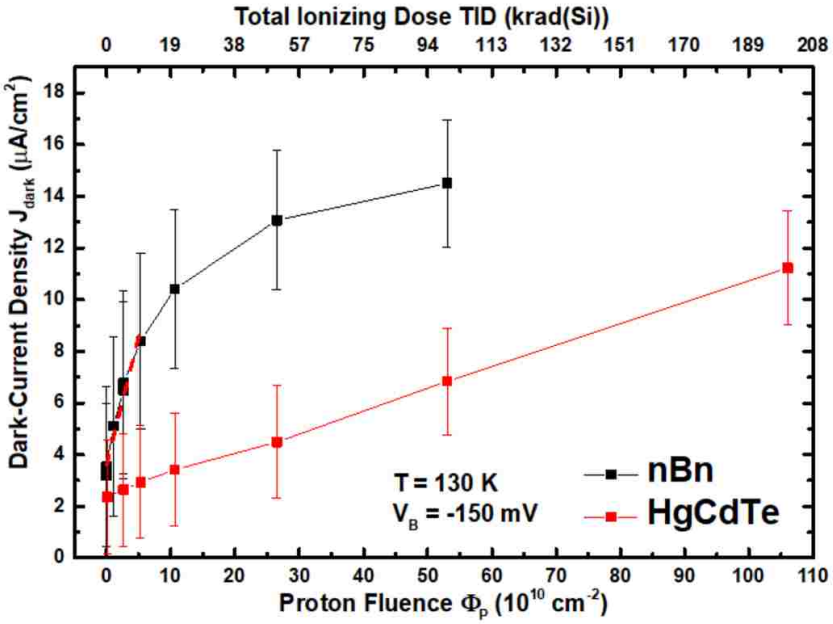

Figure 6.3: Examples of J_D increasing with Φ_p in a typical MWIR HgCdTe photodiode and an III-V Sb-based *nBn* detector.

These examples validated the device specific equations in Chapter 2 and were the source of interest in directly characterizing the minority carrier lifetime.

In Figure 6.4 all the lifetime damage factors $K_{\tau^{-1}}$ of the III-V Sb-based *nBn* and II-VI HgCdTe detector structures are plotted as a function of inverse initial SRH-lifetime $\tau^{-1}(0)$ on a log-log scale.

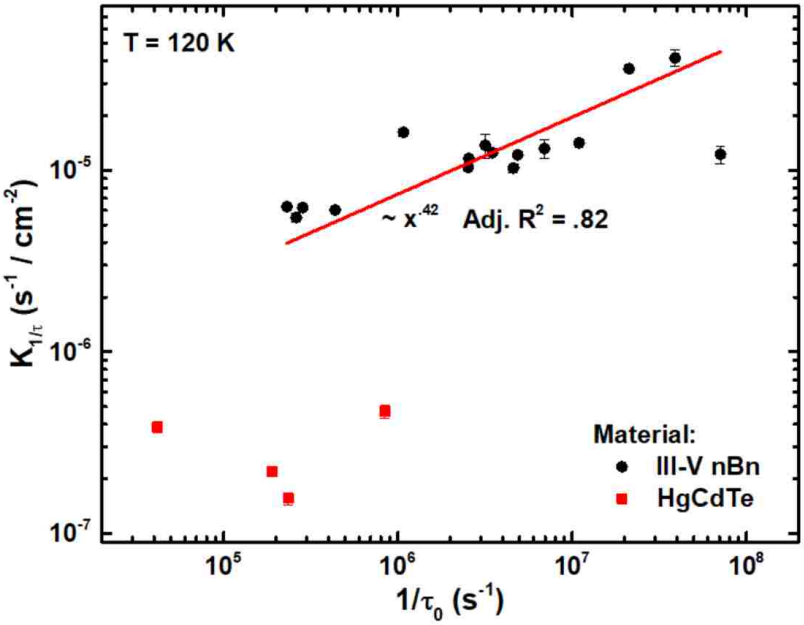

Figure 6.4: Lifetime damage factors $K_{\tau^{-1}}$ of III-V Sb-based *nBn* and II-VI HgCdTe detector structures plotted on a log-log scale as a function of the inverse of their initial lifetimes, $\tau^{-1}(0)$. Empirical fitting shows a power-law relationship between $K_{\tau^{-1}}$ and $\tau^{-1}(0)$.

This plot, again, clearly illustrates that generally the lifetime of II-VI HgCdTe materials are nearly an order of magnitude more tolerant to proton irradiation induced displacement damage compared to III-V Sb-based *nBn* materials. It also appears to indicate that a power law relationship appears to exist between $K_{\tau^{-1}}$ and $\tau^{-1}(0)$ for the *nBn* structures. While no similar relationship appears to exist for the HgCdTe samples, this may be the result of too few experiments to which can be referred. The appearance of a power-law

dependence is likely the result of $K_{\tau^{-1}}$ and $\tau^{-1}(0)$ simply sharing a similar dependence on the σv_{th} product, not necessarily an indication that $K_{\tau^{-1}}$ is really a function of τ^{-1}. If that were the case, then $K_{\tau^{-1}}$ would change with $N_T(\Phi_p)$, which an inspection of all the results from the *nBn* samples in Figure 4.17 clearly shows does not happen; rather, $K_{\tau^{-1}}$ appears to be constant for each sample over the range of interest for Φ_p here, which governs how τ can vary.

In addition to providing the inherent radiation tolerances between these two competing technologies, the extrapolation of the minority carrier lifetime damage factor over a continuous range of proton kinetic energies was enabled for InAs/InAsSb-based devices with the NIEL study. Confidence in these results was validated as data proved to be in family with what has been seen by other researchers in a variety of other III-V devices. This also indicated that the damage factors are much stronger functions of the elemental makeup (% ionic character) than on device structure (e.g. complex type-II superlattices).

The pre- and post-radiation temperature studies yielded that there are significant differences in annealing phenomena between the II-VI and III-V detector technologies. Not only did the HgCdTe samples almost completely heal after annealing, they did so very quickly and it was shown that their crystal lattice defects are mobile at much lower temperatures than those within the III-V samples.

6.3 The Fate of III-V Detectors in Space

Although high performance MWIR III-V T2SL *nBn* detectors have already been proven worthy for terrestrial applications, their future role on space vehicles is uncertain. They

can provide many advantages, as discussed in previous chapters; however, as shown in this work, they remain plagued with relatively short initial minority carrier lifetimes and poor radiation tolerance. Additionally, if strategic annealing is an option for an on-orbit radiation tolerance regimen, HgCdTe is the clear choice here as well.

All hope is not lost, however, as practically realized minority carrier lifetimes in these III-V-based detectors have yet to even approach their theoretical potential. This is the current focus of many R&D laboratories around the world, as both material quality and device architectures are being improved. Although this work has shown that lifetime damage factors for III-V devices are similar, regardless of design/architecture, Figure 5.4 indicates that the damage factors are smaller for samples having the highest initial lifetimes. In other words, the higher the purity of the initial device, the lower its lifetime damage factor will be. If the initial lifetimes can be improved significantly, the relatively poor radiation tolerance may become less of an issue.

6.4 Recommended Efforts

Several efforts are recommended as continuations of this work, and some are already under way. First, the lifetime characterization technique shall change from TRPL to W-band (94 GHz) microwave-photoconductive-decay (μPCD), also known as transient microwave reflectivity (TMR) which is described by Kadlec [**95**]. TRPL is superior for short lifetimes and simplicity for travel; however, TMR is more sensitive and superior for samples with longer lifetimes (~1 μs). Since PL will become irrelevant, the ambiguity of achieving the low-injection condition will be removed as the injection laser can be attenuated to the point that no detectable PL will be emitted. Also, TMR will enable the

radiation hardness studies of indirect bandgap samples, such as Si-based solar cells, opening up a new potential avenue of research.

It is recommended that the NIEL study on the III-V T2SL *nBn* samples be continued. Two more batches of sample set #6 are available from the sample growth which can be characterized at different proton energies to more completely fill out the NIEL curve in Figure 4.24 with empirical results.

Further analyses can be performed on the existing pre- and post-radiation lifetime vs. temperature studies. By performing curve fits on these data, such as those shown in Figure 4.18, additional information can be extracted as a function of proton fluence, such as changes in the average energy level of the defect/trap concentration and charge carrier densities as attempted by Höglund [**34**]. This should improve the understanding of the fundamental differences in lifetime radiation tolerances between II-VI and III-V material systems.

REFERENCES

[1] David A. Ramirez, Stephen A. Myers, Greg von Winckel, Sanchita Krishna, Marianne Berwick, R. Steven Padilla, Pradeep Sen, Sanjay Krishna Sebastián E. Godoy, "Dynamic infrared imaging for skin cancer screening," *Infrared Physics & Technology*, vol. 70, no. ISSN 1350-4495, pp. 147-152, 2015. [Online]. https://doi.org/10.1016/j.infrared.2014.09.017

[2] R. R. Gamache, A. Goldman, L. R. Brown, R. A. Toth, H. M. Pickett, R. L. Poynter, J.-M. Flaud, C. Camy-Peyret, A. Barbe, N. Husson, C. P. Rinsland, and M. A. H. Smith L. S. Rothman, "The HITRAN database: 1986 edition," *Appl. Opt.*, vol. 26, pp. 4058-4097, 1987. [Online]. http://hitran.org/

[3] Public Domain. (2018) Atmospheric Transmittance. [Online]. https://commons.wikimedia.org/w/index.php?curid=34818020

[4] G. D. Boreman E. L. Dereniak, *Infrared detectors and systems*, 1st ed.: Wiley-Interscience, 1996.

[5] L. Shipeng, Z. Qiao, amd W. Nigfel W. Weichen, "Jet engine temperatures," *Chinese Journal of Aeronautics*, vol. 26, no. 3, pp. 594-600, 2013.

[6] Donald A. Neamen, *Semiconductor Physics and Devices: Basic Principles*, 4th ed. New York: McGraw Hill, 2012.

[7] M. A. Kinch, *Fundamentals of Infrared Detector Materials, (Tutorial Texts in Optical Engineering)*., 2007, vol. TT76.

[8] J. L. Schmit, and T. N. Casselman G. L. Hansen, "Energy gap versus alloy composition and temperature in Hg1-xCdxTe," *J. Appl. Phys.* , vol. 53, no. 10, 1982.

[9] P. M. Young, and H. Ehrenreich C.H. Grein, "Minority carrier lifetimes in ideal InGaSb/InAs superlattices," *Appl. Phys. Lett.*, vol. 61, p. 2905, 1992.

[10] D. R. Rhiger, "Performance comparison of long-wavelength infrared type-II superlattice devices with HgCdTe," *J. Electron. Mat.* , vol. 40, pp. 1815-1822, 2011.

[11] L. Esaki and R. Tsu, "Superlattice and negative differential conductivity in semiconductors," *IBM J. Res. Develop.*, vol. 14, no. 61, 1970.

[12] D. L. Smith and C. Mailhiot, "Proposal for strained type II superlattice infrared detectors," *J. Appl. Phys.*, vol. 62, no. 2545, 1987.

[13] J. R. Meyer, C. A. Hoffman, F. J. Bartolim C. H. Grein, P. M. Young, H. Ehrenreich, R. H. Miles, and D. H. Chow E. R. Youngdale, "Auger lifetime enhancement in InAs-Ga1-xInxSb superlattices," *Appl. Phys. Lett.*, vol. 64, no. 3160, 1994.

[14] M. Walther, J. Schmitz, J. Fleibner, F. Fuchs, J. Zeigler, and W. Cabanski R. Rehm, "InAs/GaSb superlattice focal plane arrays for high-resolution thermal imaging," *Opt. Electron. Rev.* , vol. 14, no. 19, 2006.

[15] E. Plis, J. B. Rodriguez, G. D. Bishop, Y. D. Sharma, L. R. Dawson, S. Krishna, J. Bundas, R. Cook, D. Burrows, R. Dennis, K. Patnaude, A. Reisinger, and M. Sundaram H. S. Kim, "Mid-IR focal plane array based on type-II InAs/GaSb stain layer superlattice detector with nBn design.," *Appl. Phys. Lett.*, vol. 92, no. 183502, 2008.

[16] A. Soibel, S. A. Keo, J. M. Mumolo, D. Z. Ting, and S. D. Gunapal C. J. Hill, "Demonstration of large format mid-wavelength infrared focal plane arrays based on superlattice amd BIRD detector structures," *Infrared Phys. Technol.*, vol. 52, no. 348, 2009.

[17] S. A. Pour, M.-A. Hoang, A. Haddadi, M. Razehi, and M. Z. Tidrow E. K. Huang, "Low irradiance background limited type-II superlattice MWIR M-barrier imager," *Optics Lett.*, vol. 37, no. 2025, 2012.

[18] S. Ramezani-Darvish, G. Chen, A. M. Hoang, B.-M. Nguyen, and M. Razeghi A. Haddadim, "High operability 1024x1024 long wavelength type-II superlattice focal plane array," *IEEE J. Quant. Electron.*, vol. 48, no. 221, 2012.

[19] G. D. Metcalfe, H. Shen, and M. Wraback B. C. Connellym, "Direct minority carrier lifetime measurements and recombination mechanisms in long-wave infrared type-II superlattices using time-resolved photoluminesence," *Appl. Phys. Lett.*, vol. 97, no. 251117, 2010.

[20] J. G. Tischler, J. H. Warner, I. Vurgaftman, W. W. Bewley, J. R. Meyer, J. C. Kim, L. J. Whitman, C. L. Canedy, and E. M. Jackson E. H. Aifer, "W-structured type-II superlattice long-wave infrared photodiodes with high quantum efficiency," *Appl. Phys. Lett.*, vol. 89, no. 053519, 2006.

[21] S. Maimon and G. W. Wicks, "nBn detector, an infrared detector with reduced dark current and higher operating temperature," *Appl. Phys. Lett.*, vol. 89, no. 151109, 2006.

[22] D. Donetsky, D. Wang, H. Hier, F. J. Crowne, and G. Belenky S. P. Svennson, "Growth of type II strained layer superlattice, bulk InAs and GaSb materials for minority carrier lifetime characterization," *J. Crystal Growth*, vol. 334, no. 103, 2011.

[23] B. C. Connelly, G. D. Metcalfe, H. Shen, M. Wraback, D. Lubyshev, Y. Qiu, J. M. Fastenau, A. W. K. Liu, S. Elhamari, O. O. Cellek, and Y.-H. Zhang E. H. Steenbergen, "Significantly

improved minority carrier lifetime observed in a long-wavelength infrared III-V type-II superlattice comprised of InAs/InAsSb," *Appl. Phys. Lett.*, vol. 99, no. 151110, 2011.

[24] J. N. Schulman and T. C. McGill, "The CdTe/HgTe superlattice: proposal for a new infrared material," *Appl. Phys. Lett.* , vol. 34, pp. 663-5, 1979.

[25] R. M. Biefeld, T. E. Zipperian, I. J. Fritz and B. L. Doyle G. C. Osbournm L. R. Dawson, "III-V strained layer superlattices for long-wavelength detector applications: Recent progress," *J. Vac. Sci. Technol. A*, vol. 5, pp. 3150-3152, 1987.

[26] G. Sullivan, D. Lee, E. Aifer and M. Razeghi J. Bajaj, "Comparison of type-II superlattice and HgCdTe infrared detector technologies," *Proc. SPIE* , vol. 65420B, 2007.

[27] M. E. Beatty, "Changes in minority-carrier lifetime in Si and GaAs resulting from irradiation with 22 and 40-MeV protons," NASA, Langley Research Center, Technical Note 1969.

[28] A. J. Houdayer, P. F. Henrichsen, W. G. Letourneau, and J. Vincent A. L. Barry, "The energy dependence of lifetime damage constants in GaAs LEDs for 1-500 MeV protons," *IEEE Trans. Nucl. Sci.* , vol. 42, 1995.

[29] M. A. Xapsos, S. R. Messenger, E. A. Burke, R. J. Walters, G. P. Summers, and T. Jordan I. Jun, "Proton nonionizing energy loss (NIEL) for device applications," *IEEE Trans. Nucl. Sci.* , vol. 50, 2003.

[30] C. J. Dale, and P. W. Marshall G. R. Hopkinson, "Proton effects in charge-coupled devices," *IEEE Trans. Nucl. Sci*, vol. 43, 1996.

[31] R. J. Walters, S. R. Messenger, G. P. Summers, S. M. Khamna, D. Estan, L. S. Erhardt, and A. Houdayer J. H. Warner, "High energy proton irradiation effects in GaAs devices," in *7th European Conference on Radiation and Its Effects on Components and Systems, RADECS*, Noordwijk, The Netherlands, 2003, pp. 525-531.

[32] R. Ecoffet, J. Costeraste, A. Meygret, and X. Hugon, S. Barde, "Displacement damage effects in InGaAs detectors: experimental results and semi-empirical model prediction," *IEEE Trans. Nucl. Sci.*, vol. 47, no. 6, 2000.

[33] E. A. Burke, P. Shapiro, S. R. Messenger, and R. J. Walters G. P. Summers, "Damage correlations in semiconductors exposed to gamma, electron, and proton radiations," *IEEE Trans. Nucl. Sci.* , vol. 40, 1993.

[34] D. Z. Ting, A. Khoshakhlagh, A. Soibel, A. Fisher, C. J. Hill, S. Keo, S. Rafol, and S. D. Gunpala L. Hoglund, "Influence of proton radiation on the minority carrier lifetimes in midwave

infrared InAs/InAsSn superlattices," *Appl. Phys. Lett.*, vol. 108, 2016.

[35] R. Chandrasekara, C. Cheng, and A. Ling Y. C. Tan, "Silicon avalanche photodiode operation and lifetime analysis for small satellites," *Optics Express*, vol. 21, no. 14, 2013.

[36] Royal Belgian Institute for Space Aeronomy. (2018, July) Space Environment Information System (SPENVIS). [Online]. https://www.spenvis.oma.be/intro.php

[37] D. Masti, A. Ebrahimi, M. Orvatinia, and N. Maryann O. Zeynali, "The design and simulation of the shield reduce ionizing radiation effects on electronic circuits in satellites," *Electrical and Electronic Engineering*, vol. 1, no. 2, pp. 112-116, 2011.

[38] P. Marshall, B. Cummings, L. Shamey, and A. Holland C. Dale, "Displacement damage effects in mixed particle environments for shielded spacecraft CCDs," *IEEE Trans. Nucl. Sci.*, vol. 40, no. 6, 1993.

[39] J. R. Srour and J. M. McGarrity, "Radiation effects on microelectronics in space," *Proc. IEEE*, vol. 76, pp. 1443-1469, 1988.

[40] C. J. Marshall and P. W. Marshall, "Proton effects and test issues for satellite designers," *IEEE Nuclear and Space Radiation Effects Conference*, vol. Short Course Notes, pp. 50-110, 1999.

[41] E. A. Garduno, V. M. Cowan, G. Jenkins C. P. Morath, "More accurate quantum efficiency damage factor for proton-irradiated, III-V-based unipolar barrier infrared detectors," *IEEE Trans. Nucl. Sci.*, vol. 64, no. 1, January 2017.

[42] T. C. Harman, and J. P. Donnelly A. G. Foyt, "Type conversion and n-p junction formation in Hg1-xCdxTe produced by proton bombardment," *Appl. Phys. Lett.*, vol. 18, no. 8, 1970.

[43] P. G. Rancoita and M. Tacomi M. J. Boschini. (2017) SR-NIEL Calculator: Screened relativistic (SR) treatment for calculating the displacement damage and nuclear stopping powers for electrons, protons, light- and heavy- ions in materials. [Online]. http://www.sr-niel.org/

[44] V. M. Cowan, L. A. Treider, G. D. Jenkins, and J. E. Hubbs C. P. Morath, "Proton irradiation effects on the performance of III-V-based, unipolar barrier infrared detectors," *IEEE Trans. Nucl. Sci.* , vol. 62, no. 2, April 2015.

[45] C. P. Morath, and V. M. Cowan J. E. Hubbs, "Comparison of the proton radiation response of HgCdTe focal plane array technologies to a III-V nBn MWIR focal plane array," in *Proc. MSS*, 2014.

[46] S. L. Chuang, *Physics of Photonic Devices*, 2nd ed. Hoboken, New Jersey: Wiley, 2009.

[47] S. M. Sze and K. K. Ng, *Physics of Semiconductor Devices*, 3rd ed. Hoboken, New Jersey: Wiley-Interscience, 2007.

[48] R. K. Ahrenkiel and M. S. Lundstrom, *Minority Carriers in III-V semiconductors: Physics and Applications*.: Academic Press, Inc., 1993.

[49] W. Shockley and W. T. Read, "Statistics of the recombination of holes and electrons," *Phys. Rev.* , vol. 87, no. 835, 1952.

[50] R. N. Hall, "Recombination processes in semiconductors," in *Proc. of IEEE 106, 923*, 1960.

[51] J. D. Vincent, *Fundamentals of Infrared Detector Operation and Testing*. New York: Wiley, 1990.

[52] K. Adamiec, and J. Rutkowski A. Rogalski, *Narrow-gap Semiconductor Photodiodes*. Bellingham, WA: SPIE, 2000.

[53] and L. H. Hall J. Bardeenm F. J. Blatt, "Indirect transitions from the valence to the conduction bands," in *Photoconductivity Conference*, 1956, p. 146.

[54] J. Blakemore, *Semiconductor Statistics*. Mineola, New York: Dover Publications, Inc., 1962.

[55] M. Kopytko, and A. Rogalski P. Martyniuk, "Barrier infrared detectors," *Opto-Electron. Rev.*, vol. 22, no. 2, pp. 127-146, 2014.

[56] E. Plis, G. Bishop, Y. D. Sharma, H. Kim, L. R. Dawson, and S. Krishna J. B Rodriguez, "nBn structure based on InAs/GaSb type-II strained layer superlattices," *Appl. Phys. Lett.*, vol. 91, no. 043514-1-2, 2007.

[57] J. R. Pedrazzani, D. E. Sidor, S. Maimon, and G. W. Wicks G. R. Savich, "Dark current filtering in unipolar barrier infrared detectors," *Applied Physics Letters*, vol. 99, September 2011.

[58] A. Soibel, L. Hoglund, J. Nguyen, C. J. Hill, A. Khoshakhlagh, and S. D. Gunapala D. Z. Ting, "Type-II superlattice infrared detectors," in *Semiconductors and Semimetals*, D. R. Rhiger, and C. D. Jagadish S. D. Gunapala, Ed. Amsterdam: Elsevier, 2011, pp. 1-57.

[59] J. R. Pedrazzani, D. E. Sidor, and G. W. Wicks G. R. Savich, "Benefits and limitations of unipolar barriers in infrared photodetectors," *Infrared Physics and Technol.*, vol. 59, pp. 152-155, 2013.

[60] P. Klipstein, "XBn barrier photodetectors for high sensitivity operating temperature infrared sensors," in *Proc. SPIE 6940*, 2008.

[61] C. J. Hill, A. Soibel, J. Nguyen, S. A. Keo, M. C. Lee, J. M. Mumolo, J. K. Liu, and S. D. Gunapala D. Z. Ting, "Antimonide-based barrier infrared detectors," in *Proc. SPIE 6940*, 2010.

[62] O. Klin, S. Grossman, N. Snapi, I. Lukomsky, D. Aronov, M. Yassen, A. Glozman, T. Fishman, E. Berkowicz, O. Magen, I. Shtrichman, and E. Weiss P. Klipstein, "XBn barrier photodetectors based on InAsSb with high operating temperatures," *Opt. Eng.* , vol. 50, no. 061002, pp. 1-10, 2011.

[63] J. R. Pedrazzani, D. E. Sidor, S. Maimon, and G. W. Wicks G. R. Savich, "Use of unipolar barriers to block dark currents in infrared detectors," in *Proc. SPIE 8012*, 2012.

[64] P. Martyniuk and A. Rogalski, "HOT infrared photodetectors ," *Opto-Electron. Rev.* , vol. 21, pp. 240-258, 2013.

[65] D. E. Sidor, X. Du, M. Jain, C. P. Morath, V. M. Cowan, J. K. Kim, J. F. Klem, D. Leonhardt, S. D. Hawkins, T. R. Fortune, A. Tauke-Pedretti, and G. W. Wicks G. R. Savich, "Defect related dark currents in III-V MWIR nBn detectors," in *Proc. SPIE 907011*, 2014.

[66] J. Keller. (2010, December) Military and Aerospace Electronics. [Online]. https://www.militaryaerospace.com/articles/2010/12/military-infrared.html

[67] R. K. Ahrenkiel and R. S. Lundstrom, *Minority Carriers in III-V Semiconductors: Physics and Applications, vol. 39*. San Diego, USA: Academic Press, Inc., 1993.

[68] R. N. Hall, *Phys. Rev.*, vol. 87, p. 387, 1952.

[69] Teledyne Lecroy. (2018, June) Teledyne Lecroy Website. [Online]. http://cdn.teledynelecroy.com/files/appnotes/an_006a.pdf

[70] M. D. Ziegler, and J. P. Biersack J. F. Ziegler, "SRIM - The stopping and range of ions in matter," *Nuclear Instruments and Methods in Physics Research*, vol. 268, no. 11-12, pp. 1818-1823, June 2010.

[71] ISP Optics. (2018) Janis Research Company, LLC. [Online]. https://www.janis.com/Libraries/Window_Transmissions/BariumFluoride_BaF2_TransmissionCurveDataSheet.sflb.ashx

[72] C. M. Castaneda, "Crocker Nuclear Laboratory (CNL) Radiation Effects Measurement and Test Facility," *IEEE Radiation Effects Data Workshop*, pp. 77-81, 2001.

[73] R. K. Ahrenkiel, *Solid State Electronics*., 1992.

[74] G. D. Metcalfe, H. Shen, and M. Wrabeck B. C. Connelly, "Direct minority carrier lifetime measurements and recombination mechanisms in long-wave infrared type-II superlattices using time-resolved photoluminescence," *Appl. Phys. Lett.*, vol. 97, no. 251117, 2010.

[75] Z. Li, "Radiation damage effects in Si materials and detectors and rad-hard Si detectors for SLHC," *Journal of Instrumentation (JINST)*, vol. 4, no. P03011, March 2009.

[76] E. A. Burke, M. A. Xapsos, C. J. Dale, P. W. Marshall, and E. L. Petersen G. P. Summers, "Displacement Damage in GaAs Structures," *IEEE Trans. Nucl. Sci.*, vol. 35, no. 6, pp. 1221-1226, December 1988.

[77] P. W. Marshall, G. P. Summers, and E. A. Wolicki C. J. Dale, "Displacement damage equivalent to dose in silicon devices," *Appl. Phys. Lett.*, vol. 54, January 1989.

[78] Discussion with John Hubbs, August 2015.

[79] S. R. Messenger, G. P. Summers, E. A. Burke, S. M. Khanna, D. Estan, L. S. Erhardt, H. C. Liu, M. Gao, M. Buchanan, A. J. Springthorpe, A. Houdayer, and C. Carlone R. J. Walters, "Correlation of proton radiation damage in InGaAs-GaAs quantum-well light-emitting diodes," *IEEE Trans. Nucl. Sci.*, vol. 48, no. 6, pp. 1773-1777, December 2001.

[80] J.R. Srour and J.M. McGarrity, "Radiation effects on microelectronics," in *Proc. IEEE 76*, 1988, pp. 1443-1469.

[81] C. Claeys and E. Simoen, *Radiation Effects in Advanced Semiconductor Materials and Devices*, J. Parisi, and R. Hull R. M. Osgood Jr., Ed. Springer-Verlag Berlin Heidelberg New York, Germany: Springer, 2002.

[82] N. Keskitalo and A. Hallen, "Resistivity profile measurements of proton-irradiated n-type silicon," in *Solid State Electronics 37*, 1994, pp. 55-60.

[83] S. J. Taylor, M-J Yang, S. Matsuda, O. Kawasaki and T. Hisamatsu M. Yamaguchi, "High-energy and high-fluence proton irradiation effects in silicon solar cells," *J. Appl. Phys.* , vol. 80, pp. 4916-4920, 1996.

[84] P. Desgardin, M. Saillard, J. Vernois and J. F. Barbot E. Ntsoenzok, "Evolution of shallow donors with proton fluence in n-type silicon," *J. Appl. Phys.*, vol. 79, pp. 8274-8277, 1996.

[85] J. H. Crawford and J. W. Cleland, *Progress in Semiconductors*, 2nd ed., P. Aigrain and R. E. Burgess A. F. Gibson, Ed. London: Heywood and Co., 1957.

[86] J. W. Cleland and J. H. Crawford, *Phys. Rev.* , vol. 93, p. 894, 1954.

[87] A. C. Beer and R. K. Willardson F. J. Reid, *Bull. Am. Phys. Soc.*, vol. 2, p. 356, 1957.

[88] J. W. Cleland and J. H. Crawford, *Bull. Am. Phys. Soc.*, vol. 3, p. 142, 1958.

[89] L. W. Aukerman and K. Lark-Horovitz, in *Symposium on Nuclear Irradiation of Semiconductor Materials*, New York City, 1957.

[90] Antoni Rogalski, *New Ternary Alloy Systems for Infrared Detectors*.: SPIE Press, 1994.

[91] A. Rogalski, *New Ternary Alloy Systems for Infrared Detectors*. Bellingham, Washington: SPIE Optical Engineering Press, 1994.

[92] D. S. Billington and J. H. Crawford, *Radiation Damage in Solids*, 1st ed., E. P. Wigner and R. Hofstadter, Ed. Princeton, New Jersey: Princeton University Press, 1961.

[93] V. M. Goldschmitt and L. Thomassen, *Norsk. Ak. Skr.*, vol. 5, p. 58, 1924.

[94] C. Claeys and E. Simoen, *Radiation Effects in Advanced Semiconductor Materials and Devices*.: Springer, 2002.

[95] Emil A. Kadlec, "Progress Towards Competitive III-V Infrared Detectors: Fundamental Material Characterization and Techniques," University of New Mexico, Albuquerque, PhD Thesis 2017.